Characterization & Modification of Copper and Iron Oxide Nanoparticles for Application as Absorber Material in Silicon based Thin Film Solar Cells

Maurice René Nuys

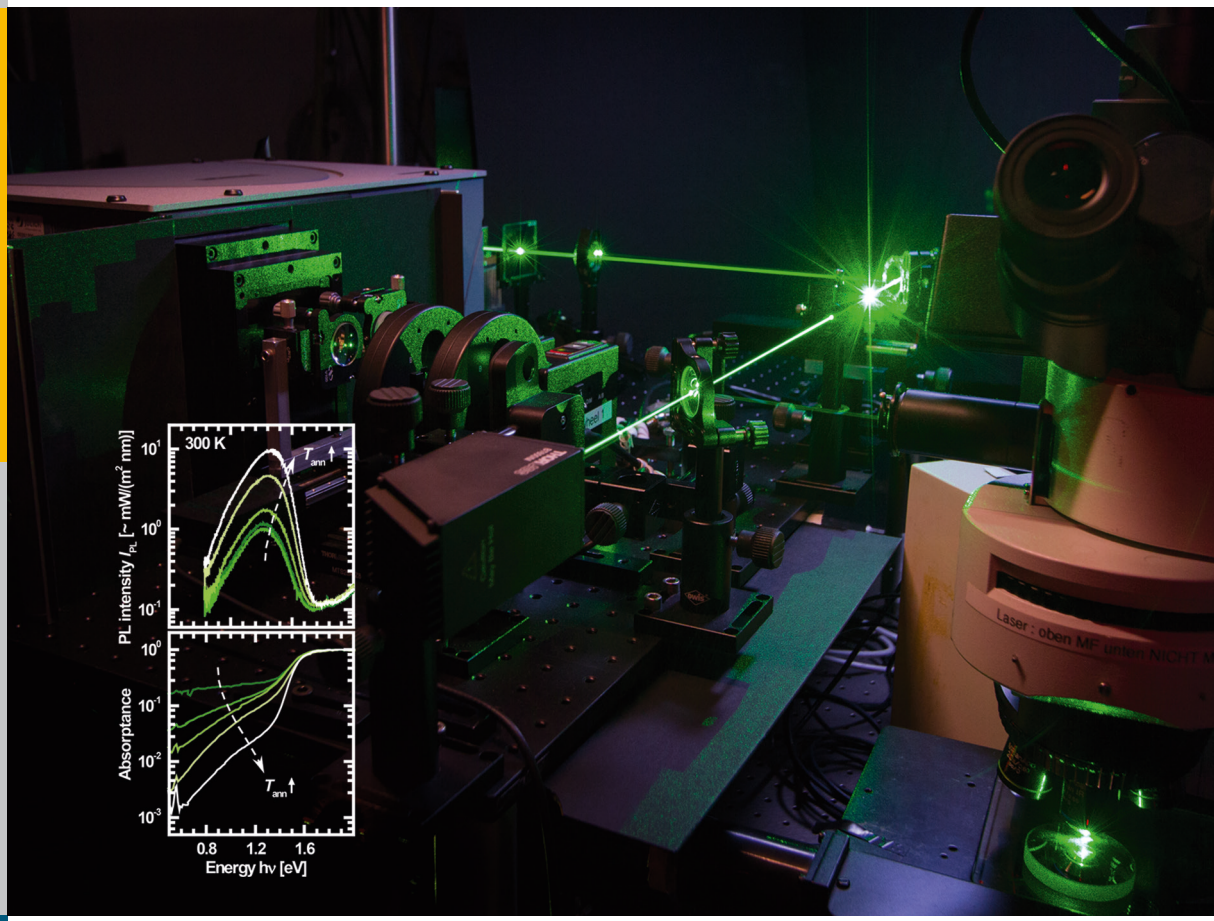

Member of the Helmholtz Association

Energie & Umwelt / Energy & Environment
Band / Volume 291
ISBN 978-3-95806-096-8

JÜLICH
FORSCHUNGSZENTRUM

Schriften des Forschungszentrums Jülich
Reihe Energie & Umwelt / Energy & Environment Band / Volume 291

Forschungszentrum Jülich GmbH
Institute of Energy and Climate Research
Photovoltaics (IEK-5)

Characterization & Modification of Copper and Iron Oxide Nanoparticles for Application as Absorber Material in Silicon based Thin Film Solar Cells

Maurice René Nuys

Schriften des Forschungszentrums Jülich
Reihe Energie & Umwelt / Energy & Environment Band / Volume 291

ISSN 1866-1793 ISBN 978-3-95806-096-8

Bibliographic information published by the Deutsche Nationalbibliothek.
The Deutsche Nationalbibliothek lists this publication in the Deutsche Nationalbibliografie; detailed bibliographic data are available in the Internet at http://dnb.d-nb.de.

Publisher and Distributor: Forschungszentrum Jülich GmbH
Zentralbibliothek
52425 Jülich
Tel: +49 2461 61-5368
Fax: +49 2461 61-6103
Email: zb-publikation@fz-juelich.de
www.fz-juelich.de/zb

Cover Design: Grafische Medien, Forschungszentrum Jülich GmbH

Printer: Grafische Medien, Forschungszentrum Jülich GmbH

Schriften des Forschungszentrums Jülich
Reihe Energie & Umwelt / Energy & Environment, Band / Volume 291

D 82 (Diss. RWTH Aachen University, 2015)

ISSN 1866-1793
ISBN 978-3-95806-096-8

The complete volume is freely available on the Internet on the Jülicher Open Access Server (JuSER) at www.fz-juelich.de/zb/openaccess.

Für meine Eltern
Beate und Gottfried Nuys

Contents

Abstract

The present thesis deals with the characterization and modification of semiconducting copper oxide (CuO, Cu_2O) and iron oxide (γ-Fe_2O_3, α-Fe_2O_3) nanoparticles, which provide a basis for an innovative solar cell concept involving nanoparticles composed of almost unlimitedly available elements as absorber material in thin film solar cells. This approach is promising to meet the requirements of increasing the production capacity and lowering the production costs if the nanoparticles exhibit superior properties compared to corresponding thin films. Therefore, the goal of this thesis is to demonstrate the high quality of semiconducting nanoparticles that can be achieved by proper treatment. The structural and opto-electronic properties of copper as well as iron oxide compounds are investigated and the influence of thermal annealing is analyzed.

Commercially available tenorite (CuO) nanoparticles with a diameter of about 30 nm are annealed stepwise up to 1000 °C in air and nitrogen atmosphere. The photoluminescence (PL) and photothermal deflection spectroscopy (PDS) results show tenorite band emission at about 1.3 eV, which strongly increases accompanied by a decreasing sub gap absorption with increasing annealing temperature up to 700 °C and 1000 °C in nitrogen atmosphere and air, respectively. These variations are ascribed to a reduction of the defect concentration. According to literature, a phase transition from tenorite to cuprite (Cu_2O) is expected and observed after annealing at 800 °C in nitrogen atmosphere. Strong cuprite band edge emission at about 2 eV accompanied by very weak defect and possibly tenorite band edge emission is found for the samples annealed at 800 °C and 1000 °C. Analyzing selected Raman and PDS spectra of the nanoparticles annealed at 800 °C, the volume fraction of a remaining tenorite phase is estimated to be smaller than 20%. There is no indication for the presence of tenorite after annealing at 1000 °C.
In comparison to results reported for tenorite bulk material and thin films, nanoparticles include fewer defects and therefore show superior opto-electronic properties. The cuprite nanoparticles exhibit excellent properties at least similar to high quality single crystals. In contrast to results usually reported in the literature for cuprite thin films, the PL spectra are not dominated by strongly pronounced defect emission, which confirms that high quality nanoparticles can be easier prepared than corresponding thin films.

Likewise, commercially available maghemite (γ-Fe_2O_3) nanoparticles with a diameter of about 8 nm to 15 nm are modified by oven annealing in nitrogen atmosphere up to 900 °C. The PDS and PL results of as-prepared nanoparticles indicate the band gap at about 2 eV and a weakly pronounced and broad emission in the spectral region of the band gap. Up to an annealing temperature of 450 °C, the nanoparticles remain in the maghemite phase and their opto-electronic properties are only weakly affected. The PDS spectra reveal typical absorption features that are ascribed to ligand field transitions at about 1.4 eV and 1.9 eV. After further annealing at 550 °C,

the nanoparticles are partially transformed into the hematite phase (α-Fe_2O_3). Due to the similarity of the electronic structure of maghemite and hematite, the emission and absorption characteristics change only slightly, but a lower sub gap absorption is observed indicating a reduction of the defect concentration. The nanoparticles are completely transformed into the hematite phase after annealing at 750 °C. The PDS spectra exhibit a significantly reduced sub gap absorption and a slightly higher emission in the spectral region of the band gap implying a substantial reduction of the defect concentration. Concomitantly, the absorption of the ligand field transition at 1.4 eV increases drastically. After annealing at 900 °C, the sub gap absorption increases significantly indicating the generation of defects at very high annealing temperatures.

The sub gap absorption of the maghemite as well as the hematite nanoparticles is similar to the absorption detected for high quality thin films and literature data of hematite single crystals as well as high quality bulk material, which provides strong evidence for the excellent properties of the nanoparticles. However, the absorption and emission spectra clearly demonstrate that for both iron oxide compounds electronic states are introduced deep in the band gap due to the ligand field splitting of iron 3*d* electrons. This intrinsic property of both iron oxides is expected to limit the Fermi-level splitting, and thus would probably restrict the achievable open circuit voltage of a photovoltaic device.

In the near IR, emission bands are observed at 0.9 eV and 1 eV, whose contributions vary substantially with the annealing temperature. The origin of these emission bands in the near IR is not explained finally. Probably, it corresponds either to characteristic ligand field or defect related transitions.

In addition, hematite nanoparticles with a diameter of about 50 nm are provided by a partner university. Raman, PL, and PDS measurements reveal similar structural and opto-electronic properties as the oven annealed hematite nanoparticles (8 nm to 15 nm) implying that the observed results are not related to size dependent effects.

For all investigated maghemite and hematite nanoparticles, sharp emission lines are observed superimposed on the broad emission between 2 eV and 2.2 eV, which are also reported in the literature. These sharp emission lines are unambiguously attributed to characteristic maghemite and hematite Raman modes. In the literature, these Raman modes are likely misinterpreted as maghemite or hematite band edge emission.

Zusammenfassung

Die vorliegende Dissertation beschäftigt sich mit der Charakterisierung und Modifizierung von halbleitenden Kupferoxid (CuO, Cu_2O) und Eisenoxid (γ-Fe_2O_3, α-Fe_2O_3) Nanopartikeln, die die Basis für ein innovatives Solarzellenkonzept darstellen, bei dem Nanopartikel aus nahezu unbegrenzt verfügbaren Elementen als Absorber in Dünnschichtsolarzellen eingebaut werden sollen. Falls Nanopartikel bessere Eigenschaften aufweisen als entsprechende Dünnschichten, stellt dieser Ansatz eine vielversprechende Perspektive dar, um Anforderungen hinsichtlich steigender Produktionskapazitäten und Reduzierung der Produktionskosten gerecht zu werden. Ziel dieser Arbeit ist es zu demonstrieren, dass durch geeignete Behandlung qualitativ hochwertige halbleitende Nanopartikel hergestellt werden können. Die strukturellen und opto-elektronischen Eigenschaften von Kupferoxid und Eisenoxid Nanopartikeln werden untersucht und der Einfluss von Temperbehandlungen wird analysiert.

Kommerziell erhältliche Tenorit (CuO) Nanopartikel mit einem Durchmesser von ungefähr 30 nm werden schrittweise in Luft und Stickstoffatmosphäre bis zu einer Temperatur von 1000 °C getempert. Photolumineszenz (PL) und photothermische Deflektionsspektroskopie (PDS) Messungen zeigen Tenorit Bandkantenlumineszenz bei ungefähr 1,3 eV, die mit steigender Tempertemperatur bis 700 °C in Stickstoffatmosphäre beziehungweise bis 1000 °C in Luft stark ansteigt. Begleitet wird der Anstieg der Lumineszenzintensität von einer deutlichen Reduzierung der Absorption unterhalb der Bandlücke. Diese Variationen werden auf eine Reduzierung der Defektkonzentration zurückgeführt. In Übereinstimmung zur Literatur wird ein Phasenübergang von Tenorit zu Kuprit (Cu_2O) nach den Temperschritten in Stickstoffatmosphäre bei 800 °C und 1000 °C beobachtet. Die PL Spektren zeigen sowohl stark ausgeprägte Bandkantenlumineszenz von Kuprit bei ungefähr 2 eV als auch schwache Emissionsbanden, die Defekten und Tenorit Bandkantenlumineszenz zugeordnet werden. Aus Raman und PDS Spektren der Nanopartikel, die bei 800 °C getempert wurden, wird ein verbleibender Volumenanteil des Tenorits auf weniger als 20% abgeschätzt. Nach dem Temperschritt bei 1000 °C wird ausschließlich Kuprit detektiert.
Im Gegensatz zu Berichten über Tenorit Volumenmaterial oder Dünnschichten weisen entsprechende Nanopartikel eine geringere Defektkonzentration auf und besitzen deshalb bessere opto-elektronische Eigenschaften. Kuprit Nanopartikel zeigen ebenfalls exzellente Eigenschaften, die vergleichbar sind zu Kuprit Einkristallen. Im Gegensatz zu Ergebnissen zu Dünnschichten in der Literatur werden die PL Spektren nicht von stark ausgeprägten Emissionen dominiert, die Defektübergängen zugeordnet werden können. Dies unterstreicht, dass qualitativ hochwertige Kuprit Nanopartikel einfacher präpariert werden können als entsprechende Dünnschichten.

Zudem werden kommerziell erhältliche Maghemit (γ-Fe_2O_3) Nanopartikel mit einem Durchmesser von ungefähr 8 nm bis 15 nm durch Temperbehandlung in Stickstoffatmosphäre bis zu einer Temperatur von 900 °C modifiziert. PDS und PL Spek-

tren der unbehandelten Nanopartikel weisen auf eine Bandlücke bei ca. 2 eV hin. Im spektralen Bereich der Bandlücke wird eine schwach ausgeprägte und breite Emission beobachtet. Bis zu einer Tempertemperatur von 450 °C verbleiben die Nanopartikel in der Maghemit-Phase und ihre opto-elektronischen Eigenschaften werden kaum beeinflusst. Die PDS Spektren zeigen typische Absorptionsmerkmale bei ungefähr 1,4 eV und 1,9 eV, die Ligandenfeldübergängen zugeordnet werden. Die Nanopartikel werden bei der Temperung bei 550 °C teilweise in Hämatit (α-Fe_2O_3) umgewandelt. Aufgrund der Ähnlichkeit der elektronischen Struktur der beiden Eisenoxide sind kaum Veränderungen in der Emission und der Absorption zu beobachten. Jedoch impliziert die geringere Absorption unterhalb der Bandlücke eine Reduzierung der Defektkonzentration. Nach dem Temperschritt bei 750 °C liegen die Nanopartikel ausschließlich in der Hämatit-Phase vor. Das entsprechende PDS Spektrum zeigt eine deutlich reduzierte Absorption unterhalb der Bandlücke und eine leicht stärkere Emission im Bereich der Bandlücke. Diese Veränderungen werden auf eine substantielle Reduzierung der Defektkonzentration zurückgeführt. Außerdem ist das Absorptionsmerkmal des Ligandenfeldübergangs bei ca. 1,4 eV deutlich stärker ausgeprägt. Nach der Temperbehandlung bei 900 °C steigt die Absorption unterhalb der Bandlücke wieder an, was darauf hindeutet, dass bei sehr hohen Temperaturen Defekte erzeugt werden.
Die Absorption der Maghemit und Hämatit Nanopartikel unterhalb der Bandlücke ist vergleichbar zu der Absorption die für epitaktisch gewachsener Dünnschichten beziehungsweise Hämatit Einkristalle und Volumenmaterial ermittelt werden. Dies demonstriert die exzellenten Eigenschaften der Nanopartikel. Jedoch zeigen die Absorptions- und Emissionsspektren die Existenz von elektronischen Zuständen tief in der Bandlücke aufgrund der Aufspaltung der 3*d* Elektronen im Ligandenfeld des Kristallgitters. Diese intrinsische Eigenschaft beider Eisenoxide limitiert vermutlich die Aufspaltung der Fermi-Niveaus und beschränkt folglich die erreichbare Leerlaufspannung einer Solarzelle.
Im nahen IR Bereich werden zwei Emissionsbanden bei ca. 0,9 eV und 1 eV beobachtet, deren Intensitäten stark mit der Tempertemperatur variieren. Die Ursache dieser Emissionen ist nicht abschließend geklärt. Ligandenfeldübergänge oder Defekte werden als mögliche Ursache diskutiert.
Zusätzlich werden Hämatit Nanopartikel mit einem Durchmesser von 50 nm von einer Partneruniversität zur Verfügung gestellt. Raman, PL und PDS Messungen zeigen ähnliche strukturelle und opto-elektronische Eigenschaften wie die getemperten Hämatit Nanopartikel (8 nm bis 15 nm). Dies impliziert, dass die beobachteten Eigenschaften nicht auf größenabhängige Effekte zurückzuführen sind.
In allen PL Spektren der Eisenoxid Nanopartikel überlagern scharfe Emissionslinien, die auch in der Literatur beobachtet werden, die breite Emission im Bereich von 2 eV bis 2,2 eV. Diese scharfen Linien werden eindeutig typischen Maghemit und Hämatit Ramanmoden zugeordnet. In der Literatur wurden diese Moden wahrscheinlich als Maghemit und Hämatit Bandkantenlumineszenz fehlinterpretiert.

Chapter 1

Introduction

Photovoltaics is one of the most attractive options for a sustainable supply of electric power in the future. According to the EPIA[1], photovoltaics will provide 10% of the electricity demand in the EU in 2030, which the EIA[2] forcasts to a total of 3×10^{13} kWh. In order to meet this enormous demand, the production capacities have to be increased drastically. For this purpose, thin film solar cells with high efficiencies on the basis of earth abundant materials are preferred. Besides the medium- to long-term abundance, environmentally sustainable material extraction and processing is desirable. Furthermore, the energy input for the production is an essential issue for the economy of solar cells.
Currently, the prevailing solar cell technologies are based on crystalline Si, CdTe, amorphous/microcrystalline Si (a-Si:H, μc-Si:H) as well as Cu(In,Ga)Se_2. In contrast to the abundance of Si, limitations of the availability are proposed for Ga, Se, In, and Te in the medium-term [1, 2]. For crystalline silicon, a thick absorber layer is required due to its low absorption coefficient. In order to lower the production costs, the thickness of the Si wafer has to be reduced. Though meeting most of the requirements, thin film silicon solar cells based on amorphous or microcrystalline hydrogenated silicon suffer from a low conversion efficiency. Therefore, innovative concepts and new materials have to be developed and analyzed in order to cope with the enumerated requirements.

In the past, various compound semiconductors have been investigated with respect to their suitability for photovoltaic application. For instance, silicides (β-$FeSi_2$, Ca_2Si) as well as sulfides (pyrite-FeS_2, ZrS_2, chalcocite-Cu_2S) and oxides (CuO, Cu_2O, α-, γ-Fe_2O_3) are composed of elements, which are abundantly present in the crust of the earth. The named compound semiconductors cover a wide range of band gaps from about 0.8 eV (β-$FeSi_2$) to 2.2 eV (α-Fe_2O_3) accompanied by high absorption coefficients exceeding $10^5\,cm^{-1}$ just above the optical band gap and are therefore

[1] **E**uropean **P**hotovoltaic **I**ndustry **A**ssociation
[2] **E**nergy **I**nformation **A**dministration

favorable for the application as absorber materials in thin film solar cells [3, 4, 5]. Recently, chalcocite-Cu_2S and pyrite-FeS_2 have been identified to be promising candidates with respect to availability, extraction costs, band gap, and absorption coefficient [6].
Attempts to prepare efficient solar cells on the basis of β-$FeSi_2$, pyrite-FeS_2, chalcocite-Cu_2S, and Cu_2O thin films failed because of various reasons. For $FeSi_2$ and FeS_2, poor opto-electronic properties due to a high defect concentration and high recombination rates were crucial parameters limiting the open circuit voltage resulting in poor cell performance with efficiencies below 3% [7, 8]. Besides, the stoichiometry of some compound semiconductors, i.e. FeS_2 and β-$FeSi_2$, allows only a narrow range of tolerance, which carries the danger of unwanted impurity phases, which again deteriorates the solar cell performance. The research of Cu_2S predominantly failed due to the high mobility of the copper atoms and thus leading to a degradation of the prepared solar cells. Cu_2O tended to be deoxidized to elemental copper [9]. Thin films and bulk material of other materials such as CuO, Fe_2O_3, and ZrS_2 have not been explored with respect to a photovoltaic application in detail.
All the presented attempts base on the preparation of crystalline thin films. However, recent progress in the nanotechnology offers a variety of new low-cost production processes such as spin-coating or ink-jet printing, whereby nanoparticle dispersions are cast onto the substrate. Using nanoparticles instead of thin films is a promising approach to overcome problems of the past. We expect that phase pure and almost defect free nanoparticles can be prepared more easily than thin films. Moreover, nanoparticles may favor a self-purification process, since impurities and material defects tend to diffuse to the surface upon thermal annealing leading to an increased material perfection. In the near past, the feasibility of nanoparticles for photovoltaic application is indicated [10, 11, 12].

In the Institute for Energy and Climate (IEK-5 Photovoltaik) Forschungszentrum Jülich GmbH, an innovative cell concept based on nanocrystalline absorber materials is proposed, which benefits from the advantages of nanotechnologie combined with the expertise in silicon based thin film photovoltaics of the IEK-5.[3] Semiconducting nanoparticles of almost unlimitedly available elements with high absorption coefficients are investigated for their feasibility as new absorber material in thin film solar cells. Developing and stacking absorber materials with different band gaps, the conversion efficiency of solar cells can be increased significantly. The specific configuration of such a solar cell depends on the properties of the nanoparticles and is hence not decided finally. Schematically, the new concept can be understood as a silicon based thin film solar cell, which absorber layers are substituted by nanopar-

[3] This idea was introduced by Prof. Dr. R. Carius Institute of Energy and Climate (IEK-5 Photovoltaik) Forschungszentrum Jülich GmbH and is the basis for a current research programme. The presented thesis was prepared in this context and a BMBF project NADNuM; project nr. 03SF0402A NADNuM.

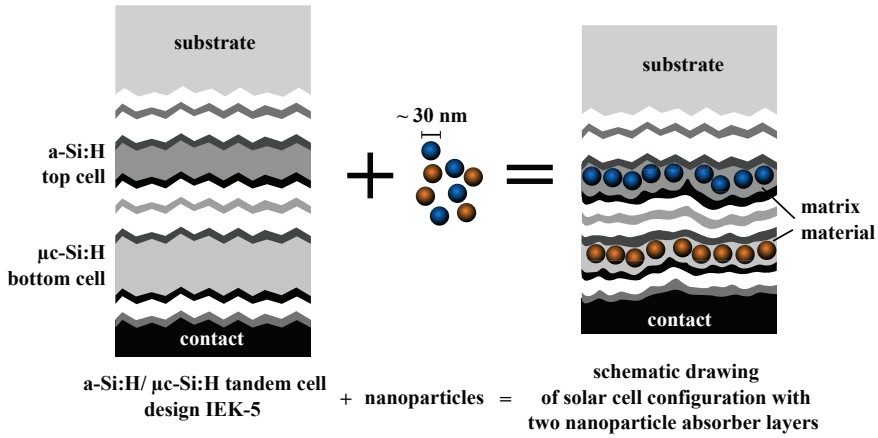

Figure 1.1 – *Schematic illustration of the suggested innovative solar cell concept. On the basis of a standard a-Si:H/µc-Si:H tandem solar cell (left image) that is typically prepared at the IEK-5. Nanoparticles with different band gaps are used to substitute the absorber layers. Note, that illustrated model (right image) illustrated the concept, but the exact cell configuration is not specified, so far.*

ticle mono layers (cf. figure 1.1). At the IEK-5, profound experience with various matrix materials, in which the nanoparticles can be incorporated, such as a-Si:H, a-$Si_{1-x}Ge_x$:H, a-SiO_x, a-$Si_{1-x}C_x$:H, and ZnO are available using low temperature deposition techniques like PECVD[4] and HWCVD[5]. The assortment of different alloys allows to adjust the interface properties in terms of suitable workfunctions and passivation of surface defects. Applying light management concepts, which have been intensively studied and developed in the context of thin film solar cells, the effective optical path of the light in the absorber can be enhanced by more than a factor of ten. Consequently, assuming an absorption coefficient of about $10^5\,cm^{-1}$ above the band gap, 95% of the light is absorbed by a monolayer of nanoparticles with a diameter of only 30 nm, which allows low material consumption and cost efficient solar cell production. Furthermore, the decoupling of the nanoparticle synthesis and solar cell implementation bares new degrees of freedom, especially in terms of temperature and chemical treatment for optimization, which would not be compatible with low temperature vacuum deposition techniques and cheap substrates like glas or foils.

[4]**P**lasma **E**nhanced **C**hemical **V**apor **D**eposition
[5]**H**ot **W**ire **C**hemical **V**apor **D**eposition

The present thesis is the first step into the suggested innovative solar cell concept. The high expectations base on the assumption, that nanoparticles exhibit superior properties compared to corresponding thin films. Therefore, the goal of this thesis is to demonstrate the high quality of nanoparticles that can be achieved by proper treatment. For this, the structural and opto-electronic properties of binary oxides are investigated and the influence of thermal annealing is analyzed.
In **chapter 2** the characterization methods along with their basic fundamentals are briefly introduced. Special respect is attributed to the micro-photoluminescence and micro-Raman setup.
Chapter 3 gives an overview about the structural and opto-electronic properties of copper oxide (CuO, Cu_2O) as well as iron oxide (α- and γ-Fe_2O_3) bulk material and thin films.
Chapter 4 and 5 deal with the characterization and modification of copper oxide and iron oxide nanoparticles, respectively. The nanoparticles are oven annealed stepwise in different atmospheres and the properties are evaluated with respect to literature data of corresponding bulk material and thin films. The evolution of the emission and absorption characteristics are studied in detail. Special respect is given to the defect structure of the respective materials. Additionally, selected results of two diploma theses that are completed in the course of this work are presented.
Finally, **chapter 6** summarizes and evaluates the properties of the binary oxide nanoparticles in terms of their feasibility for photovoltaic application.

Chapter

2

Fundamentals and characterization methods

In context of this thesis the structural, electronic and optical properties of semiconducting nanoparticles are investigated. In order to characterize the nanoparticles and the influence of the modification by thermal annealing, several characterization techniques are employed. The structure and morphology of the nanoparticles is investigated by Raman spectroscopy, X-ray diffraction (XRD), transmission electron microscopy (TEM), and scanning electron microscopy (SEM). The electronic properties and the optical absorption are examined by photoluminescence (PL) and photothermal deflection spectroscopy (PDS). In the following chapter, these techniques along with their basic fundamentals are briefly introduced with special respect to the benefit to this work. The micro-Raman and micro-PL setup is described and the procedure of raw data calibration is explained.

2.1 Raman spectroscopy

In the current thesis, Raman spectroscopy is used to investigate the vibrational modes of nanoparticles. Raman spectroscopy is a spectroscopic technique that is based on inelastic scattering of monochromatic light meaning that the frequency of the incident light changes upon interaction with a solid. The largest part of the incident monochromatic light with the energy $E = \hbar\omega$ is elastically scattered (Rayleigh scattering). However, a small fraction of the light interacts with the solid inelastically by the excitation or annulation of phonons. If a phonon is excited, the frequency of the scattered light ω_S is reduced by the phonon frequency Ω, $\omega_S = \omega - \Omega$. This phenomena is called Stokes scattering. In case of Anti-Stokes scattering, a phonon is annihilated and the frequency of the emitted photon is increased

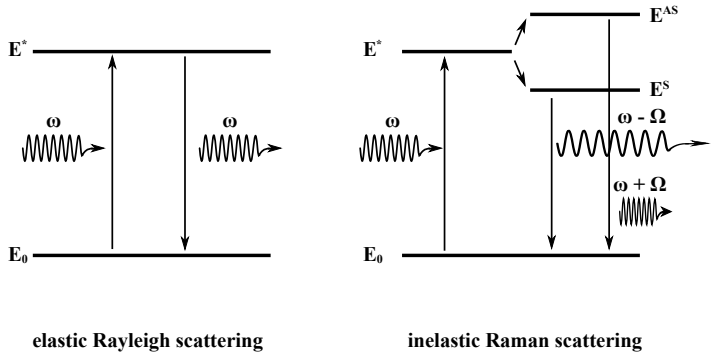

Figure 2.1 *– Schematic drawing of elastic Rayleigh (left) and inelastical Raman scattering (right). The exciting photon with the frequency ω is absorbed and promotes the system from the ground state E_0 into an excited state E^*. In case of Rayleigh scattering, the system relaxes back into the ground state by emitting a photon with the same frequency ω. Raman scattering is observed when the excited state splits into one slightly higher and one lower energy state by the annulation or generation of a phonon with the frequency Ω, respectively. Hence, the frequency of the emitted photon is increased or reduced by the phonon energy.*

by the phonon frequency $\omega_{AS} = \omega + \Omega$. Figure 2.1 depicts the three mentioned cases schematically.
Symmetry and polarizability of a crystal determine whether a phonon is Raman active or not. The phonon frequencies are characteristic for the crystal. Therefore, the Raman signal may allow to identify the material system and differentiates between stoichiometries or polytypes. However, this presupposes that the different material systems exhibit Raman active modes, and that different stoichiometries and polytypes show distinctively different Raman signatures. Under appropriate conditions, Raman signals offer information about defects and stress in the material. Defects and stress may lead to a distortion of the lattice and therefore to a variation of the binding properties, which can lead to a shift of the Raman frequencies and a variation of the line shape of the Raman signal.

2.2 Photoluminescence

Photoluminescence spectroscopy (PL spectroscopy) is a very sensitive tool to probe intrinsic as well as defects induced luminescent transitions in semiconductor materials. Hence, the PL signal provides information about the electronic structure, the band gap, defect states, and the quality of the investigated material. In general, luminescence is the emission of light from a solid arising from deviations from the thermal equilibrium. For instance, this equilibrium can be disturbed through excitation by the absorption of light. Photons with energies larger than the optical band gap E_g can excite electrons from the valence into the conduction band, i.e. electron-hole pairs are generated. Photoluminescence (PL) is the radiation that is emitted by the recombination of photo-excited electron-hole pairs.
In order to classify the different recombination mechanisms, the electronic structure of the semiconductor has to be considered. Thus, in the following section, the electronic structure of semiconductors is briefly introduced. Afterwards, optical generation and different recombination processes are described.

2.2.1 Electronic structure of semiconductors

The *band gap* is one of the fundamental characteristics of a semiconducting material. It describes the energy region between the highest occupied state in the top of the valence and the lowest unoccupied state in the bottom of the conduction band. Very close to the valence and conduction band edges, the density of the so called *extended band states* can be approximated by square root like functions.
On the other hand, there are states, which are energetically located between the band states within the band gap. States close to the band edges are referred to as *band-tail states*, whereas so called *deep states* are found deep in the band gap. There are several reasons for the formation of band-tail states. For instance, in disordered semiconductors, like hydrogenated amorphous silicon (a-Si:H), the variations of the interatomatic distances and binding angles result in a broadening of the distribution of the electronic states extending into the band gap, which is described by an exponential relation and referred to as Urbach-tail [13]. Besides, also crystalline phases form band-tails, which is widely discussed in the literature and various models are proposed to explain the origin of this behaviour. For example, fluctuations of the band gap value due to ionicity, stress, or local lattice vibrations are taken into account. Because of statistical nature, a Gaussian energy distribution is used to describe these fluctuations [14, 15]. Furthermore, in binary systems of two elements A and B, miscible phases A_xB can exist with different opto-electronic properties. If there is a continuous distribution of the miscible phase, a superposition of differenct electronic configurations leads to a distribution of states extending into the band gap. Also impurity atoms that are added as dopants induce acceptor or donor levels slightly above or below the valence and conduction band, respectively. Moreover,

introducing point defects such as vacancies, interstitials, and antisites into a crystal, a structural relaxation takes place, which is reflected in a change of the interatomic distances and binding angles in the vicinity of the defect. Through this, also the electronic structure is altered by inducing defect levels close to the band edges or deep in the band gap. *Vacancy* defects are empty lattice sites V_A, which would be usually occupied in a perfect crystal, whereas *interstitials* A_i describe the case when a site is occupied that is usually not part of the lattice. *Antisites* are found in alloys or compounds of at least two atom species A and B. Then, the antisite A_B implies that the atom species A occupies a lattice site that is normally filled by the species B. Also, *dangling bonds* that represent unsaturated atomic bonds might give rise to electronic states in the band gap. In disordered semiconductors, such as amorphous silicon, a high concentration of dangling bonds is found in the volume [16]. For crystalline material, dangling bonds predominantly arise from unsaturated states at the surface. Lastly, the disruption of the periodicity of the lattice at the surface can induce electronic states within the band gap of a semiconductor material.

2.2.2 Generation & recombination processes

Through the absorption of photons electron-hole pairs are created by exciting an electron from the valence band into the conduction band, and thereby creating a hole in the valence band. As illustrated in figure 2.2, this excitation can either be a direct transition or an indirect one. In the former case, the maximum of the valence band and the minimum of the conduction band are located at the same position in the reciprocal space. In contrast to that, for an indirect semiconductor, the valence band maximum and the conduction band minimum are located at different positions in the reciprocal space. Due to the conservation of momentum, this difference has to be compensated. For small variations, the change of the momentum can be supplied by the momentum of the photon, whereas phonons have to be emitted or absorbed to balance larger differences. Once an electron-hole pair is generated, there are *radiative* and *non-radiative* recombination mechanisms. In the following, the most important radiative and non-radiative recombination processes are briefly introduced.

The radiative recombination is spectrally distributed and gives information about the electronic states of the recombining charge carriers. According to Fermi's Golden rule, the transition rate writes as

$$R(E) \propto \int |M_{if}|^2 (1 - f(E')) g_f(E') \cdot f(E + E') g_i(E + E') dE' \tag{2.1}$$

Here, M_{if} is the transition matrix element coupling the wavefunctions of the initial (i) and final (f) state. $g_{i/f}$ represents the distribution of the density of states of the initial and final state. The function f gives the occupation probability function of electronic states of the initial states. Consequently, $1 - f$ describes the probability

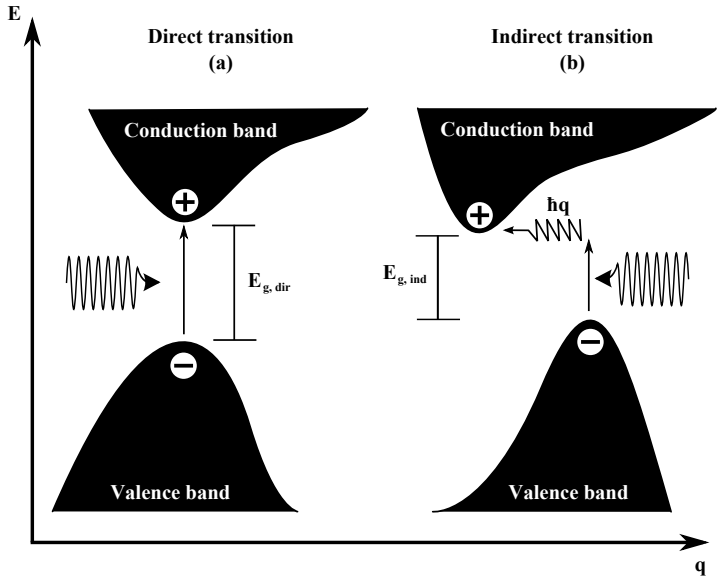

Figure 2.2 *– Schematic drawing of the band structure of a direct (left) and an indirect (right) semiconductor. The generation of an electron-hole pair by the absorption of a photon is indicated for the direct and the phonon assisted indirect transition.*

that the final state is empty. Therefore, the luminescence and absorption spectra give advice about the joint density of states weighted by its occupation probability as well as the transition matrix elements. Depending on which electronic states are involved in the transition, several recombination processes are distinguished. Figure 2.3 illustrates the charge carrier generation and radiative recombination processes schematically.

After excitation (1), the electrons and holes thermalize within a timescale of picoseconds, i.e. they move to the band edges (2) or into shallow states (3) close to the band edges by dissipating their energy by the emission of phonons.
Band-to-band luminescence (4) arises from the recombination of electron-hole pairs from the extended states of the valence and conduction bands. From the band edges the electron and hole recombine and a photon with the energy close to the band gap energy is emitted. Coulomb interaction of the electron-hole pair and electron-phonon coupling may account for slight deviations of the photon energy from the band gap energy.
Moreover, states within the band gap such as band-tail states as well as deep states may give rise to radiative transitions with energies lower than the band gap energy. Transitions that involve band states and/or band-tail states are called *band-to-tail*

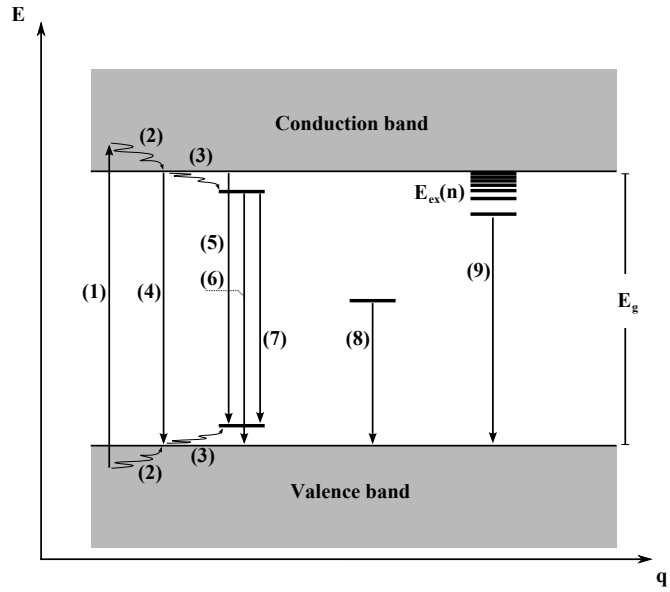

Figure 2.3 *– Typical generation and radiative recombination processes in semiconductor: (1) generation of an electron-hole pair, (2) thermalization to the band edges and (3) into shallow states close to the band edges. (4) band-band, (5) band-to-tail, (6) tail-to-band, and (7) tail-to-tail transitions are presented as well as transitions involving deep states in the band gap (8) and excitonic states (9).*

(5), *tail-to-band* (6), or *tail-to-tail* (7) transitions. The energy of the emitted photon is significantly lower than the band gap energy when deep states are included in the transition (8). Lastly, luminescence can arise from *excitonic* states (9). An exciton is a bound electron-hole pair that can be formed by the absorption of a photon. Due to the coulomb interaction between the electron and the hole the total energy of the exciton is marginally smaller than the band gap energy. Depending on the properties of the exciton, one distinguishes between Frenkel- and Mott-Wannier-excitons. They describe the two limit cases of small and large distances of the separated charges. For organic semiconductors Frenkel-excitons are most prevalently observed. Their exciton binding energies can reach values up to 1 eV. Mott-Wannier-excitons describe the limit case of large distances. Free excitons are easily captured by defects and form a bound exciton-defect complex. Excitons show a series of discrete energy levels $E_{ex}(n)$, which can be desribed by a simple hydrogenic model and can be written as

$$E_{ex}(n) = \frac{m_r e^4}{2(4\pi\epsilon_0\epsilon_r\hbar)^2 n^2} \tag{2.2}$$

in which $\frac{1}{m_r} = \frac{1}{m_e^*} + \frac{1}{m_h^*}$ represents the reduced mass, ϵ_r is the specific dielectric constant of the material and n the quantum number. Hence, the emission energy of free excitons is the band gap energy E_g reduced by the exciton binding energy E_{ex}. Due to thermal dissociation at higher temperatures, excitons are mostly observed at low temperatures $k_B T < E_{ex}$. Free excitons get easily bound to impurities or defects forming complexes with a binding energy E_{BE}. The transition energy E_{BX} of such a bound exciton is given by

$$E_{BX} = E_g - E_{BE} \tag{2.3}$$

Usually, non-radiative recombination is an undesired issue, since it involves the dissipation of the excitation energy as phonons. Since no photons are emitted, non-radiative recombination processes cannot be directly observed in PL spectra. However, radiative and non-radiative transitions are competing recombination mechanisms. Hence, non-radiative recombination becomes indirectly visible with a reduced emission intensity of radiative transitions. For non-ratiative recombination processes the energy of the electron-hole pair dissipates to the lattice by multi-phonon emission. The probability for non-radiative recombination by the emission of photons decreases exponentionally with the energy that has to be handed over. Consequently, especially for high band gap semiconductors, this process is improbable. The probability increases significantly, when the transition is mediated by deep states in the middle of the band gap. The recombination via deep states through multi-phonon emission is referred to as *Shockley-Read-Hall* recombination. The probability for this transition increases with an increasing concentration of deep states in the band gap. Considering that these states usually arise from defects or impurity atoms, the non-radiative recombination provides information about the material quality.
Auger recombination describes another non-radiative recombination process involving an additional electron or hole. When the electron-hole pair recombines its energy is given to another electron or hole which is thereby ejected deep into the conduction or valence band, respectively. The ejected carrier then thermalizes to the band edge by multi-phonon emission. Since it requires the interaction of three carriers, the Auger effect is most important for indirect semiconductors with long carrier lifetime as well as heavily doped semiconductors or at high carrier injection levels.

2.3 Photothermal deflection spectroscopy

Photothermal deflection spectroscopy (PDS) is a sensitive tool to measure the absorption coefficient reliably in a wide dynamic range of more than four orders of magnitude [17]. It measures the absorption on the basis of the thermal state of the sample due to the absorption of radiation and is not calculated from transmission and reflection data. Thus, the PDS spectroscopy technique does not suffer from problems of accuracy due to the small differences of large numbers as it is the case

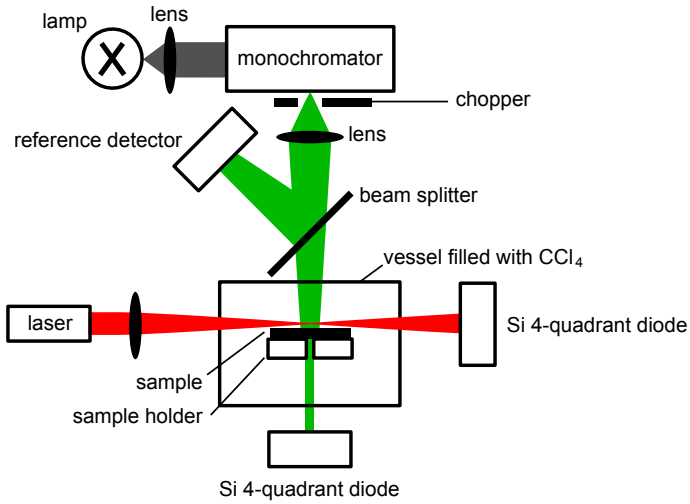

Figure 2.4 *– Schematic drawing of the PDS setup.*

for conventional transmission and reflection measurements in the region of low absorption. Moreover, using the thermal state of the sample, the PDS spectra is only weakly influenced by scattering and film inhomogeneity e.g. by partial coverage of the substrate.
In figure 2.4 the principle of the PDS measurement setup is illustrated schematically. The light of a vapor discharge lamp is dispersed in a monochromator so that monochromatic light can be focused on the sample. The sample is adjusted in a quartz vessel, which is filled with tetrachlorcarbon CCl_4. This liquid is used, as its refractive index strongly depends on the temperature and is similar to the refractive index of the quartz vessel. Moreover, CCl_4 is chemical inert. The light beam illuminates the sample and is absorbed. As described in section 2.2, an excited electron can relax non-radiatively by exciting phonons. The generation of a phonon is always connected to a generation of heat, which is released to the surrounding area. Therefore, adjacent to the sample, a temperature gradient $\vec{\nabla} T$ establishes in the CCl_4 liquid. The warmer the liquid, the smaller is its refractive index n_{fl}. In conclusion, a gradient in the refractive index $\vec{\nabla} n_{\mathrm{fl}}$ accrues, which is the basis for the photothermal deflection spectroscopy. A laser beam, adjusted parallel to the surface of the sample, is deflected due to this gradient by the angle β. The deflected beam is detected by a silicon 4-quadrant-diode. The deflection angle is directly proportional to the power of the absorbed light. For films a special method is used, to determine

the absorption coefficient without interference fringes. To apply this method it is necessary to measure the transmission additionally. If the refractive index n of the examined material and the film thickness d are known, the absorption and transmission values can be used to calculate the absorption coefficient. However for most samples which are presented in this thesis, it is not easy to estimate an effective sample thickness. Therefore, the absolute value of the absorption coefficient cannot be specified. Yet, the qualitative characteristics of the absorption coefficient are well illustrated. In the region of high absorption, the PDS signals saturate indicating an absorbance close to one. The PDS spectra that are presented in this thesis are thus normalized to one and interpreted as the absorbance.

2.4 X-ray diffraction (XRD)

When an electromagnetic wave interacts with matter, diffraction patterns are visible if the wavelength of the incident irradiation is of the order of lattice plane distances. Lattice plane distances are commonly in the range of several tenth of a nanometer which is the wavelength of X-rays. Therefore, the diffraction pattern of X-rays that are diffracted at a solid provides information about the solid's crystal structure [18]. Consequently, it is possible to identify different phases within the investigated solid due to characteristic lattice plane distances. Warren et al. investigated phenomenologically the line broadening of XRD reflexes and identified stress and size effects to be mainly responsible for it [19, 20]. Consequently, the line broadening exhibits information about the size of the nanoparticles which are analyzed in this thesis as well as about lattice imperfections such as stacking fault and point defects. The XRD reflexes are fitted by two Voigt-function profiles (so called double-Voigt approach) which allows to separate the influence of stress and defect induced line broadening. The nanoparticle size and the distortion of the lattice plane distance can be estimated.

2.5 Transmission electron microscopy (TEM)

Transmission electron microscopy (TEM) is a technique that uses an electron beam with an energy of about 200 keV to analyze the sample. Thus, the de Broglie wavelength of the electrons is smaller than 0.01 nm which allows to investigate the sample with a resolution in the nm-range. With the help of magnetic lenses, the electron beam can be focussed on single nanoparticles or clusters of few nanoparticles. Hence, using TEM, the properties of single nanoparticles or selected nanoparticle clusters can be examined. Several imaging modi are possible. In the following the bright field and dark field imaging mode as well as the selected area electron diffraction (SAED) technique are briefly indroduced.

The bright field imaging mode provides a two-dimensional projection of the

sample. The contrast of the image directly arises from the absorption of electrons in the sample. If investigating nanoparticles for instance, the nanoparticles will appear dark and the regions without nanoparticles will be bright. Therefore, this technique reveals information about size and shape of the nanoparticles.
In the dark field mode, the direct electron beam is blocked and only the diffracted electrons are collected. Therefore, the areas exhibiting the crystallographic orientation that fullfills the Bragg condition appear bright in the dark field image. Tilting the sample, different areas match the Bragg condition and appear bright.
Similar to the mechanism described earlier for X-ray irradiation, electrons are also diffracted at the lattice planes and give information about the phase of the investigated material. In contrast to XRD, the **selected area electron diffraction (SAED)** technique allows to investigate the diffraction pattern of single nanoparticles or clusters of few nanoparticles.
Besides, there exist different spectroscopic techniques like electron energy loss spectroscopy (EELS) providing information about the local elemental composition.

2.6 Scanning electron microscopy (SEM)

The scanning electron microscope (SEM) uses a focused electron beam to probe the surface of a specimen. With the help of magnetic lenses, the electron is scanned over the surface, so that a two-dimensional image of the sample is generated with an achievable resolution better than one nanometer. Several imaging modi can be employed. In the course of this thesis, only the electrons (secondary electrons), which escape from the specimen due to the interaction with the incident electrons (primary electrons), are anaylzed. These secondary electrons come from the first few nanometers of the sample and image the morphology of the sample. Hence, this mode is suitable to analyze the distribution of the nanoparticles on the substrate. Investigating the back-scattered primary electrons, the characteristic X-rays, or the light emission (cathodoluminescence, CL) provide information about the chemical composition, the crystal structure, and the electronic properties of the specimen.

2.7 Raman and PL setup

In this work the Raman and PL experiments are conducted in the same configuration. Using the exact same spot of the sample for excitation of both measurements, structural and electronic properties can be correlated locally. Moreover, by using a microscope (BX250, Olympus) the excited area is small, so that local differences can be investigated. Figure 2.5 illustrates the experimental setup. A semiconductor laser of the series Cobolt Samba with a wavelength of 532 nm and a maximum power of 150 mW is used as the light source. With the help of the microscope optics the irradiated area of the sample has a diameter of about 1 µm. An IR objective

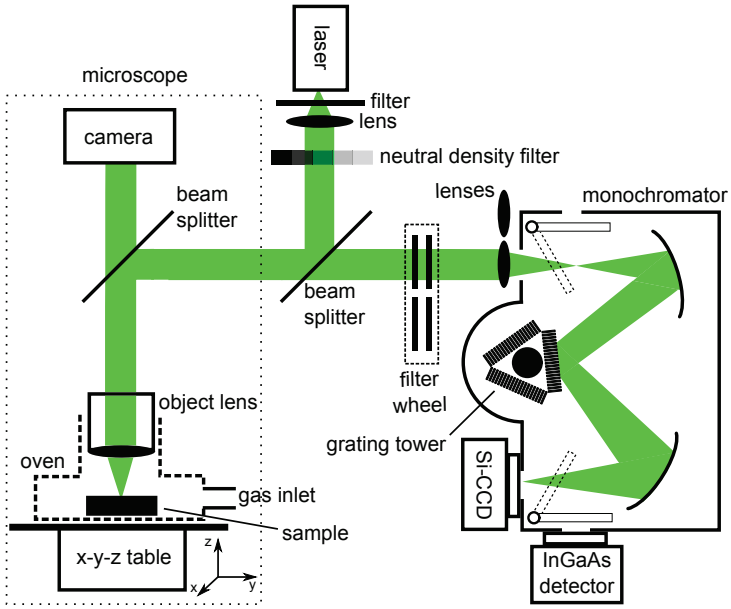

Figure 2.5 *– Schematic drawing of the Micro-Raman and Micro-PL setup.*

lense with a magnification of 50 × and a numerical aperture of 0.55 is used (LM PLan IR, Olympus). The sample is installed on a microscopic stage (Märzhäuser), which can be moved into the x, y and z direction. The accuracy of repositioning is significantly smaller than 200 nm and about 1 µm in the x-y plane and along the z achses, respectively. Optionally, an oven can be attached on the stage enabling to heat the sample during the measurement and perform the measurements under nitrogen atmosphere. A *Horiba iHR 320* grating monochromator equipped with a Silicon-CCD and an InGaAs detector is used to detect the Raman and PL signal. The Si-CCD (Photometrics) is a 512 × 1024 pixel matrix with a pixel size of 25 µm × 25 µm. The camera is cooled by liquid nitrogen to about -135 °C. The InGaAs line (Bayspec) with 512 pixel (pixel size: 25 µm × 500 µm) is upgraded with a water cooling system resulting in an operating temperature of -75 °C. In the course of this thesis, this InGaAs line was replaced by an Andor *iDus InGaAs 1.7* µm detector line with 512 pixels (pixel size: 25 µm × 500 µm). A mirror is used to switch between the detectors. Three gratings with a groove density of 2400 mm^{-1}, 235 mm^{-1}, and 85 mm^{-1} and blazed at 400 nm, 870 nm, and 1200 nm, respectively, are mounted onto the grating tower. While the 2400 mm^{-1} line grating is used for the Raman measurements due to its higher resolving power, the 235 mm^{-1} and 85 mm^{-1} line gratings allow to detect a larger spectral region which can be aquired and are therefore used for the PL measurements. Before beeing coupled into the monochromator, the signal

passes two filter wheels and is focussed on the entrance slit with a lense. Depending on the spectral region of interest different filters and lenses can be used. The filter wheels contain several red glas, notch, and edge filters. A VIS- or NIR-Achromat is used for focussing. With the help of the neutral density filter, that is devided in ten zones, the laser power can be variied by about one order of magnitude. Further filters can be applied so that the laser power can be varied. The maximum laser power is about $30\,\mathrm{Wcm^{-2}}$.
In context of a diploma thesis, J. Bergmann extended and partly automated the setup which was initially arranged by J. Flohre during his diploma thesis [21, 22]. The software, that is described in detail in J. Bergmann's diploma thesis, allows to switch the grating, the detector, lenses and filters. Raman and PL measurements can therefore be conducted automatically. Moreover, the microscope stage is controlled by the software. Hence, several points on the sample can be measured consecutively. Merely the objective lens in the microscope has to be changed manually.

2.7.1 Experimental details and data evaluation

As described earlier, the filter, lenses, and monochromator setup depend on the kind of measurement. The adjustment details and raw data evaluation is described in the following.

2.7.1.1 Raman measurements

The Raman signal is detected with the Si-CCD and the 2400 line grating which offers the best resolution. Two KF532 edge filters are used to block the exciting laser. In order to focus the Raman signal onto the slit of the monochromator the VIS-Achromat is used and a slit width of $200\,\mu\mathrm{m}$ is adjusted. Each spectrum is corrected for the background signal and divided by the measurement time. Cosmic spikes are removed manually.

2.7.1.2 PL measurements

The PL of the sample is detected from about 0.8 eV to 2.2 eV. It is not possible to detect the whole spectrum in one shot. Thus, the central grating position and the detector have to be varied. The Si-CCD is used to detect the signal from 1.1 eV to 2.2 eV. For this, the $235\,\mathrm{mm^{-1}}$ line grating and two central grating positions of about 1.25 eV and 1.66 eV are used. The IR-objective and the NIR-Achromat are employed. Two KF532 edge filters are applied in case of the central grating position of 1.66 eV whereas one of the filters is replaced by the RG665 edge filter for the second grating position. The PL signal between 0.8 eV and 1.6 eV is recorded by the InGaAs detector. For this purpose, either the $235\,\mathrm{mm^{-1}}$ line grating with the central positions set at 0.80 eV, 0.86 eV, 0.93 eV, 1.02 eV, 1.13 eV, 1.27 eV, and 1.47 eV, or the $85\,\mathrm{mm^{-1}}$ line grating set at 0.89 eV and 1.18 eV are used. For all

InGaAs measurements the IR-objective and the NIR-Achromat are applied. Up to a central grating position of 0.89 eV two RG830 edge filters are equipped, whereas a KF532 combined with a RG715 edge filter is used above 0.89 eV.

2.7.1.3 Raw data evaluation

The central grating positions are choosen in the way that the spectra overlap at the edges. Through this, the spectra can be fit together easily. However, the raw data has to be corrected for the spectral response of the system beforehand. The emitted signal of the sample runs through several optical elements leading to a change of the spectral intensity. Furthermore, there is a spectral weighting due to the quantum efficiency of the detectors. The overall measured signal can therefore be described as the true signal which is modified. If the spectral sensitivity of all elements was known, a calibration function could be deduced by multiplication of all transmission signals. The true signal would be calculated by dividing the measured signal by this calibration function. Since not all transmission signals are available, an experimental method is used to determine a calibration curve (c.f. diploma thesis J. Flohre [21]). The calibration procedure is illustrated in figure 2.6. A calibrated halogen lamp with a well known spectrum (b) is installed at the position where the sample is usually installed. For each filter, lense, grating and detector combination a spectrum is detected (a). By dividing the measured halogen spectrum (a) by the true halogen spectrum (b) a correction curve (c) is derived. The corrected PL spectrum (e) is obtained by dividing the measured PL spectrum (d) by this correction curve (c). This procedure is performed for each grating position. The different sections are connected at the edges and the connected spectrum is normalized to the measuring time of the silicon measurement with the central grating position of 1.66 eV.

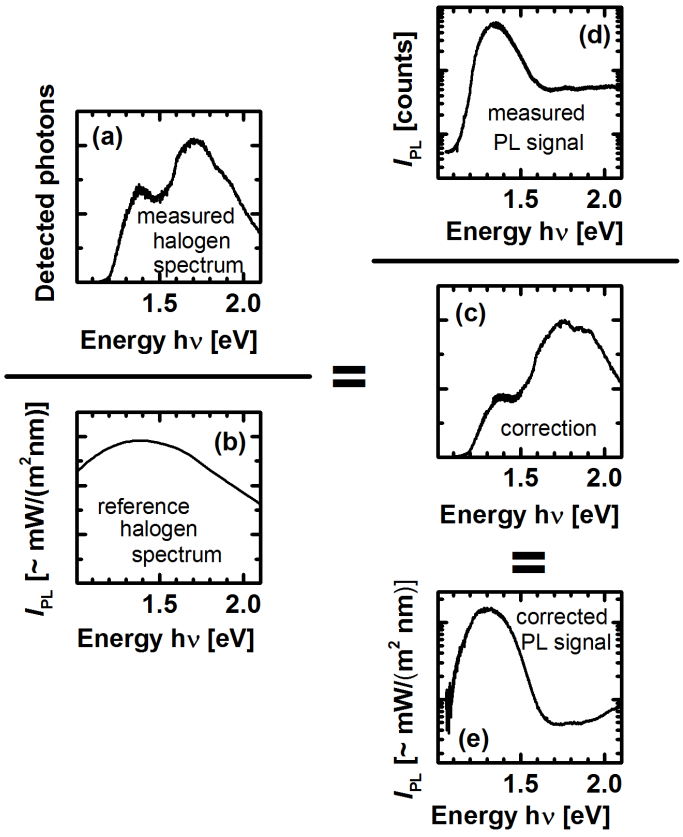

Figure 2.6 – *Schematic drawing of the intensity calibration of the measured PL signal. (a) measured halogen spectrum, (b) known halogen reference, (c) correction curve, (d) measured PL spectrum, and (e) calibrated PL spectrum (c.f. J. Flohre's diploma thesis [21]).*

Chapter

3

Material properties

In course of this thesis copper and iron oxide nanoparticles are modified and characterized. These binary oxides exist in different polytypes and stoichiometries with different structural and opto-electronic properties. The different phases have more or less been investigated in the past. In the following chapter the different polytypes and stoichiometries are listed and characteristic properties of mainly bulk material are presented. Special attention is paid to the absorption and emission characteristics as well as the Raman spectra since these properties will be analyzed in detail in this thesis.

3.1 The physics of copper oxide

In nature, copper oxide occurs in two stoichiometries, namely copper(II)-oxide (CuO, tenorite) and copper(I)-oxide (Cu_2O, cuprite). The black solid tenorite crystallizes in a monoclinic and the red-brown cuprite in a cubic Bravais lattice. Rakhshani summarized information about the stability regions of the Cu-Cu_2O-CuO system (cf. figure 3.1) [27]. Tenorite can be transformed into cuprite at high temperature. The phase transition temperature depends on the partial pressure of oxygen and the reduction of the copper atoms is achieved by the release of oxygen

$$4CuO \rightarrow 2Cu_2O + O_2 \tag{3.1}$$

For the sake of completeness, the metastable phase Cu_4O_3 deserves mentioning, which is also referred to as paramelaconite. So far, there are only few reports about its optical and electronic properties [28].

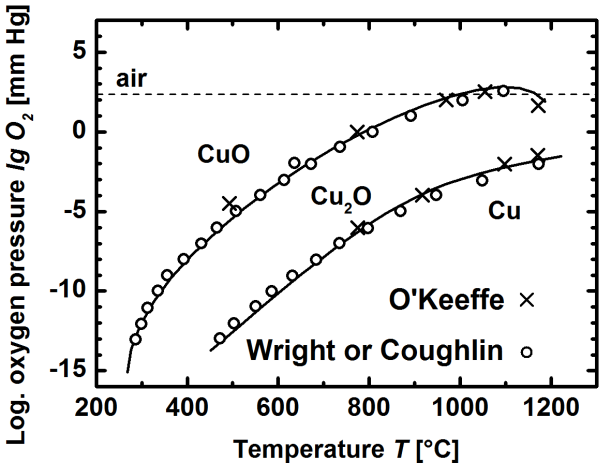

Figure 3.1 *– P-T phase stability diagram of the Cu-Cu_2O-CuO system according to Rakhshani [23] comprising data from Wright (circle), Coughling (circle) and O'Keeffe et al. (cross) [24, 25, 26].*

3.1.1 History of cuprite

Cuprite was one of the first materials showing semiconducting properties [29, 30]. The interest in cuprite began in the 1920s with the invention of the rectifier [31]. After 1940 the interest in cuprite decreased due to the increasing focus on silicon, germanium, selenium and other materials. The work on cuprite was revived in the 1970s. Cuprite was intensively investigated and in particular with regard to its suitability for photovoltaic application. Due to its suitable band gap and a high absorption coefficient above the optial band gap accompanied by its abundance and cheapness, cuprite was considered as an alternative for silicon as the absorber material in solar cells. For instance, cuprite was prepared by various techniques such as thermal oxidation of metallic copper, electrodeposition, and sputtering [32, 33, 34]. Heterojunction and Schottky barrier solar cells were prepared (e.g. [35, 36]). However, the efficiency did not exceed 3%. Due to the lack of a technique to prepare high quality n-type cuprite, homojunction solar cells could not be fabricated. The work done in this era is summarized by Rai et al. [37]. Poor material properties due to high defect concentration and the formation of metallic copper at the surface were crucial parameters leading to a fading interest in cuprite for photovoltaic application. The copper oxide was reduced to elementary copper resulting in a Cu_2O/Cu Schottky contact which limited the open circuit voltage [38, 39, 9]. Recently, cuprite regained attention as absorber material in thin film solar cells [28].

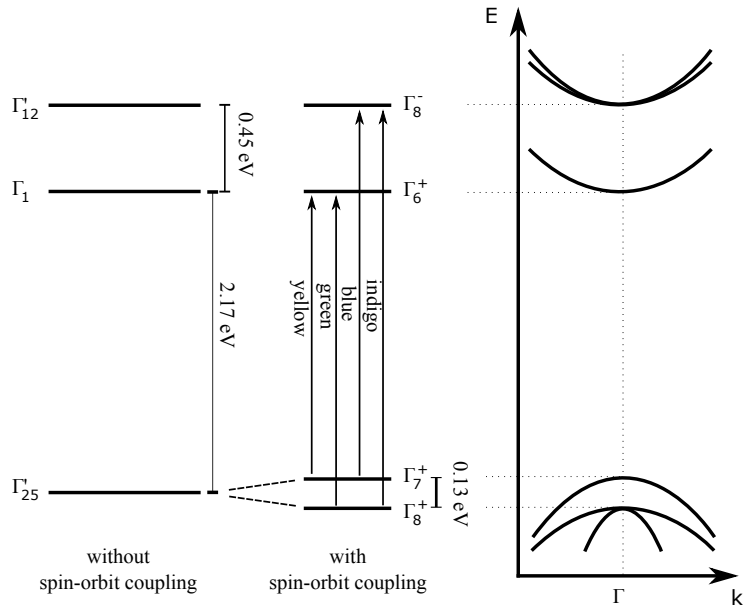

Figure 3.2 *– Band diagram of cuprite near the* Γ*-point (compare Meyer et al. [28]). The left and middle scheme illustrate the band scheme without and with considering spin-orbit coupling, respectively. On the right site the dispersion of the bands is depicted.*

3.1.1.1 Cuprite band structure

Cuprite is a semiconductor with a forbidden direct transition at 2.1 eV. The band structure of cuprite and especially its excitonic transitions were intensively investigated in the past [40, 41, 42, 43, 44, 45, 46, 47, 48]. A direct transition is found at the Γ-point of the Brioullin zone. The electronic states of the valence band and the conduction band are predominantly $3d^{10}$ and $4s$ character of the Cu atoms, respectively [43]. Scheme 3.2 shows the band structure at the Γ-point. Taking into account the splitting of the Γ_{25}' state into Γ_7^+ and Γ_8^+ due to spin-orbit interaction, the two lowest transitions are parity forbidden ($\Gamma_7^+ \rightarrow \Gamma_6^+$ and $\Gamma_8^+ \rightarrow \Gamma_6^+$). The four forbidden and allowed transitions are are named according to their wavelength (yellow, green, blue, and indigo). These transitions are accompanied by excitonic transitions with high binding energies in the range of 46 meV to 150 meV. The dispersion relation at the Γ-point was also deduced from cyclotron resonance measurements [49, 50].

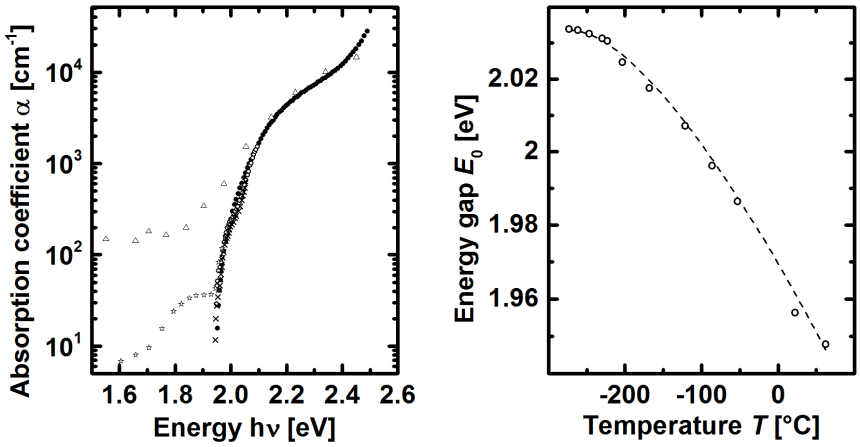

Figure 3.3 *– (a) the absorption coefficient of Cu_2O bulk material and thin films after different publications [27, 51, 41, 52]. (b) temperature dependence of the fundamental energy gap determined by PL measurements after Snoke et al. [53].*

3.1.1.2 Absorption coefficient of cuprite

Figure 3.3 (a) illustrates the absorption coefficient of cuprite bulk material and thin films measured at room temperature in the region of its optical band gap [27, 51, 41, 54]. Between 1.9 eV and 2.1 eV the absorption coefficient increases by about two orders of magnitude indicating the optical band gap. Snoke et al. deduced the temperature dependence of the optical band gap by photoluminescence measurements. The shift of the band gap is shown in figure 3.3 (b). Rakhshani et al. and Weichman et al. report an absorption tail for energies below 1.9 eV which is attributed to defect or free carrier absorption [27, 54].

M. Zouaghi and B. Prevot et al. analyzed the absorption and photoconductivity characteristics of cuprite in the near infrared [56, 57, 55]. Figure 3.4 (a) illustrates the absorption coefficient of a representative sample in the region between 0.7 eV to 2.1 eV at 77K. The spectrum exhibits several absorption maxima which were assigned to transitions involving states in the forbidden energy region. Five energy levels are suggested to explain the features of the absorption and photoconductivity measurements (cf. figure 3.4) [56]. The level β was observed for all samples and shifts to lower energies with increasing temperature. It was assigned to exciton-defect complexes of the yellow exciton. The acceptor level A is situated about 0.55 eV above the valence band and ascribed to copper vacancies. The donor level D is placed about 0.38 eV below the conduction band and attributed to oxygen vacancies. Two further levels B and C are found 0.76 eV and 0.97 eV above the

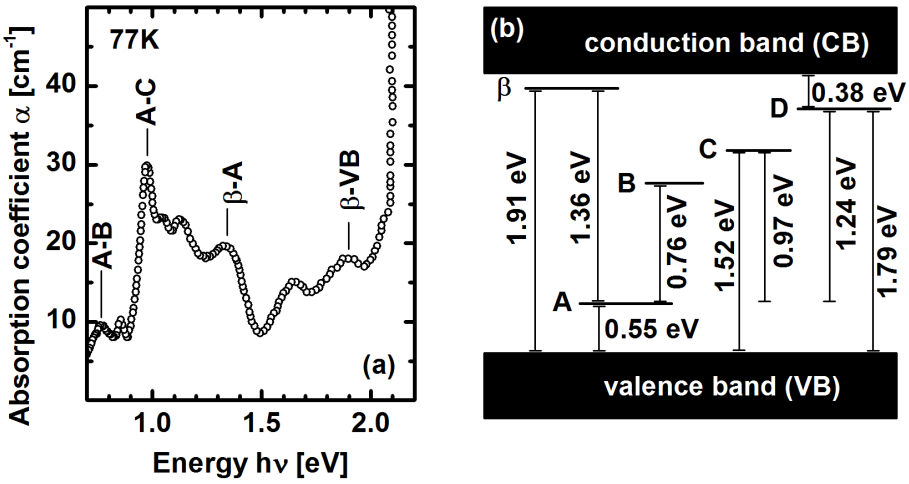

Figure 3.4 *– (a) the absorption coefficient of cuprite in the near infrared at 77K after Prevot et al. [55]. (b) sketches a model of defect and exciton related energy levels within the forbidden band gap suggested by Zouaghi et al. [56]. Some of the absorption maxima in figure (a) are assigned according to the scheme proposed in figure (b).*

level A, respectively. The transitions between the levels are associated with copper-oxygen vacancy (A-B) and copper-copper vacancy (A-C) transitions.

3.1.1.3 Non-stoichiometry of cuprite

Cuprite shows deviation from the perfect stoichiometry and is often referred to as $Cu_{2-\delta}O$. This non-stoichiometry is explained by copper (V_{Cu}) and oxygen vacancies (V_O). The density of vacancies and other defects such as interstitials strongly depends on the preparation technique, the deposition temperature, and the oxygen pressure. For instance, experimental data show that the density of vacancies depends on the logarithm of the oxygen activity $\lg a_{O_2}$ as illustrated in figure 3.5 [58]. Cuprite exhibits interesting electrical, and opto-electronic properties which are governed by the defect concentration. For example, its p-type character is attributed to copper vacancies acting as an acceptor level [30, 29]. In 1956 J. Bloem ascribed photoluminescence signals in the IR region to oxygen and copper vacancy related transitions [60]. The findings are summarized in detail in the subsequent section. Zouaghi et al. suggest an extended version of Bloem's model which describes the absorption and photoconductivity measurements in the near infrared (cf. figure 3.4)[56]. Experimental and theoretical work was devoted to the band scheme within the forbidden energy region and several groups extended this model

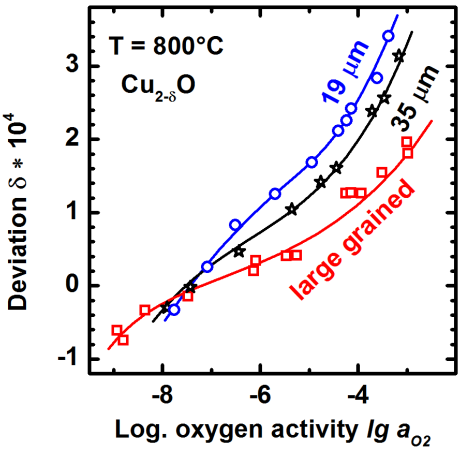

Figure 3.5 – *Variation of δ in polycrystalline $Cu_{2-\delta}O$ depending on the logarithm of the oxygen activity $\lg a_{O_2}$ are prepared at 800° C (blue circle and black star) after Aggarwal et al. [58]. The data for the large grain sample (red square) is taken from the literature after Xue et al. [59].*

[61, 62, 63, 64, 65, 66, 67, 68]. However, differences of the exact energetic position and of the number of levels are reported. Up to now, there is no model, which is capable to explain all the different findings. Different preparation techniques and thus a different amount and distribution of defects are probably responsible for this.

3.1.1.4 Photoluminescence of cuprite

Snoke et al. investigated PL spectra in the region around 2 eV of natural, high purity cuprite samples [53]. A dominant emission band consisting of two luminescence lines are found which are attributed to phonon assisted exciton recombination. The figures 3.6 (a) and (b) illustrate PL spectra of natural, high purity samples of cuprite detected at 77 K (square, b), 220 K (triangle, a), 295 K (star, a), and 335 K (circle, a) after Snoke et al. [53]. Note, Snoke et al. give no information about the unit of the PL intensity. The relative peak intensities and the peak position vary with the sample temperature. With increasing sample temperature, the emission signal shifts to lower energies and the intensity of the low energy emission decreases (cf. figure 3.6 (a)). The exciton states of cuprite consist of a spin singlet paraexciton and a spin triplet orthoexciton. According to its crystal symmetry, the recombination is dipole and quadrupole forbidden for the paraexciton and dipole forbidden for the orthoexciton. Therefore, the dominant transition mechanism is a phonon assisted recombination of the orthoexciton. The transition involving the 13.6 meV (110 cm^{-1}) optical phonon (Γ_{12}) is more than one order of magnitute larger than the direct

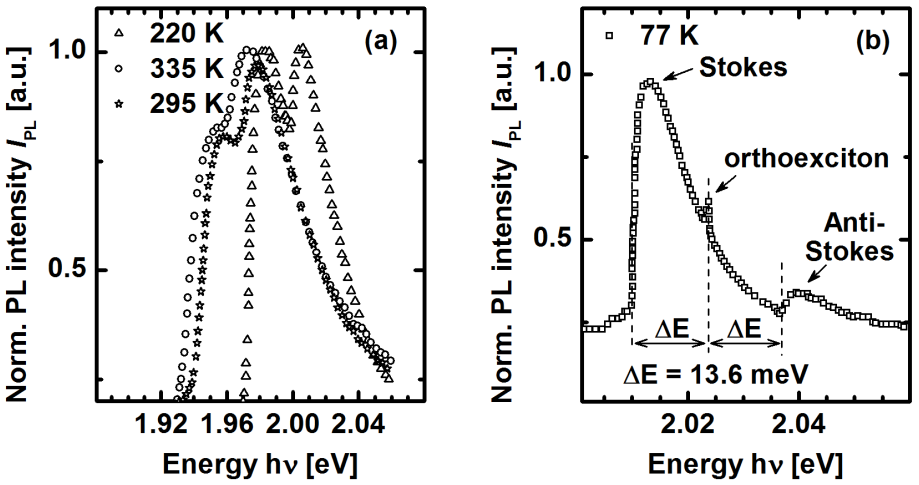

Figure 3.6 – *PL spectra of natural, high purity samples of cuprite detected at sample temperatures of 220 K (triangle, (a)), 295 K (star, (a)), 335 K (circle, (a)), and 77 K (square, (b)) after Snoke et al. [53].*

recombination of the paraexciton or any other assisted transition involving other phonons [69]. At 77 K the direct recombination line of the orthoexciton is observed at about 2.024 eV (cf. figure 3.6 (b)). The onset of the two phonon assisted emission lines is about 13.6 meV above and below the direct orthoexciton emission which is in line with the energy of the Γ_{12} phonon.

As mentioned earlier, copper and oxygen vacancies give rise to levels within the forbidden energy gap. Several groups investigated the emission spectra of cuprite in the energy region below 1.8 eV [60, 71, 72, 70]. Figure 3.7 illustrates several normalized PL spectra after Bloem et al. and Ito et al. detected at 20 K and 77 K, respectively [60, 70]. The results of natural single crystals (square) and samples that are prepared by oxidizing pure copper or the floating-zone method under various atmospheres are depicted. Note, Bloem et al. as well as Ito et al. give no information about the unit of the PL intensity. Depending on the preparation technique the spectra differ. For instance, Ito does not observe emission bands below 1.4 eV. Moreover, for natural cuprite, the relative and absolute peak intensities as well as the exact peak positions vary. The two high energy peaks are attributed to transitions involving oxygen vacancies whereas the emission peak at about 1.35 eV and a signal at 1.2 eV is ascribed to copper vacancies.

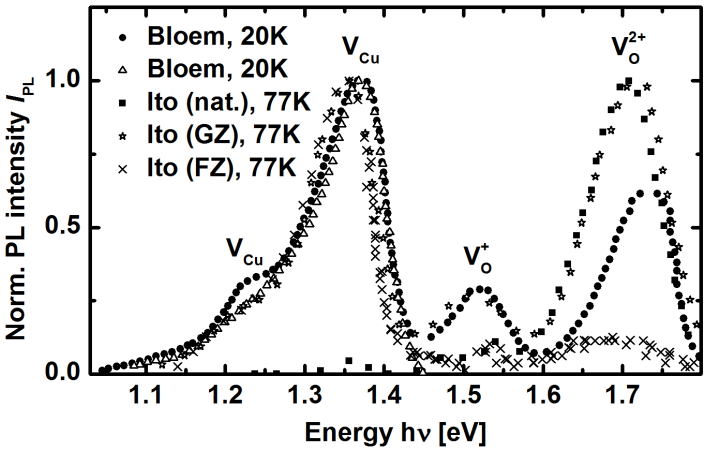

Figure 3.7 *– PL spectra of cuprite (after Bloem et al. and Ito et al.) detected at 20 K and 77 K, respectively [60, 70]. Bloem prepared the samples by oxidizing pure copper foil in argon atmosphere with a oxygen content of 1% at 960 °C. The samples were reheated at 960 °C under 4 µbar (circle) and 133 µbar (triangle) partial pressure of oxygen and then quenched in water. Ito et al. investigated natural grown cuprite single crystals (square) and samples that were prepared by floating-zone growth in air (FZ, cross) and under an argon pressure of 2 atm with 3% oxygen content (GZ, star).*

3.1.1.5 Raman modes of cuprite

The crystal structure of cuprite is a simple cubic lattice with two Cu_2O molecules in the primitive unit cell. This structure possesses the symmetry operations of the $O_h{}^4$ space group. The six atoms per unit cell result in eighteen normal modes. Huang et al. derived the normal modes of vibration of cuprite on the basis of symmetry considerations [73]. One Raman active and two IR active modes are identified. All other modes are silent in Raman as well as in IR spectra. Rigid-ion-lattice-dynamics calculations were performed to obtain the six optical modes [74]. For the Raman active mode a frequency of $550\,cm^{-1}$ and for the two IR active TO (LO) modes the frequencies $608\,cm^{-1}$ ($638\,cm^{-1}$) and $143\,cm^{-1}$ ($159\,cm^{-1}$) are obtained. The other three optical modes are expected to have fequencies of $99\,cm^{-1}$, $111\,cm^{-1}$ and $308\,cm^{-1}$. Several groups determined the frequencies of the IR active modes experimentally [75, 76, 77, 78]. Most results agree well with the predicted values reported by Carabatos et al [74]. The Raman spectrum of cuprite exhibits a multiplicity of features [79, 77, 78, 80]. In the literature the Raman characteristic of cuprous oxide has been investigated intensively. Similar results have been obtained by different groups. Merely the interpretation of the spectra differs. Table 3.1 sum-

marizes representative experimental results obtained by Reydellet et al. [77]. The identification of the Raman active normal mode is ambiguous. For instance, the frequencies 220 cm^{-1}, 515 cm^{-1}, and 598 cm^{-1} were attributed to the Raman active normal mode [79, 80, 77]. The strongest feature in the Raman spectra at 220 cm^{-1} can probably be excluded. It is suggested to arise from second-order scattering from the 110 cm^{-1} normal mode [80]. Moreover, it differs significantly from 550 cm^{-1} which was calculated to be the Raman active mode [74]. The other two values compare reasonably with the calculation. A definite assignment to one or the other is not possible so far.
It is hardly possible to assign the other features in the Raman spectra to a specific excitation or interaction. In contrast to a perfect crystal, defects result in a breakdown of selection rules, so that normally forbidden transitions are activated. Therefore, the IR active modes are observed in the Raman spectra. Moreover, multiphonon processes are likely to contribute to the spectra.

Table 3.1 – *Experimental (and calculated) Raman frequencies of cuprite, tenorite, and paramelaconite. The Raman frequencies are presented in relative wavenumbers (cm^{-1}) and the strongest intensities in the experimental data are indicated by bolt type.*

	Cuprite	**Tenorite**	**Paramelaconite**	
	48	**298**	175	
	53	345	**280**	
	58	632	320	318 (320)
	100			(448)
	108			(484)
	148			510 (506)
	180			**541** (521)
	190			651 (627)
	200			
	219			
	308			
	418			
	487			
	510			
	598			
	625			
	650			
	695			
References	[77]	[81, 82, 83]	[28]	[84]

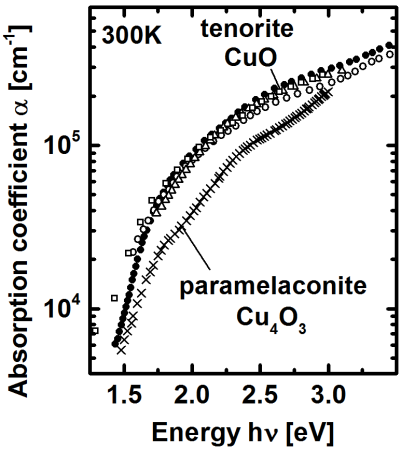

Figure 3.8 *– Absorption coefficient of tenorite (circle, open circle, open triangle, and open square) and paramelaconite (cross) after [87, 88, 28, 89].*

3.1.2 Tenorite and paramelaconite

For tenorite and paramelconite the crystallographic structure was determined. The crystal structure of tenorite is a monoclinic lattice with four CuO molecules in the unit cell and two molecules in the primitive cell [85]. The unit cell possesses the symmetry operations of the $C_{2h}{}^6$ space group. Paramelaconite exhibits a body-centered tetragonal structure and the $D_{4h}{}^{19}$ space group [86]. In chemical formula, paramelaconite can be written as follows, indicating that the copper atoms appear in an oxidation state of +2 as well as +1.

$$Cu_2^+Cu_2^{2+}O_3^{2-} \tag{3.2}$$

3.1.2.1 Absorption coefficient of tenorite and paramelaconite

Besides fundamental work on the crystal structure, there are few reports about the optical and electronic properties of tenorite and paramelaconite. Tenorite is believed to be a semiconductor with a band gap of ca. 1.35 eV to 1.5 eV [89, 90, 91]. Similar to the well known Cu_2O phase, Cu vacancies probably lead to a natural p-type character [28, 92, 93]. Recently, theoretical calculations predict an indirect transition at about 1 eV at which 3d electrons of the copper atoms form the top valence and the lowest conduction band [94]. There are some reports about the absorption characteristics of tenorite and lately the absorption coefficient of a paramelaconite thin film determined by ellipsometry was published (cf. figure 3.8) [87, 88, 28, 89]. For tenorite, similar results are found. Between 1.5 eV and 1.7 eV the absorption

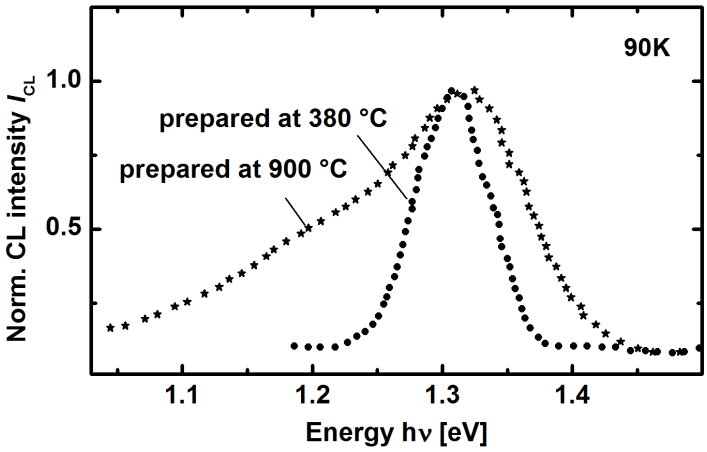

Figure 3.9 – *Cathodoluminescence spectra measured at 90 K of tenorite nanostructures grown by thermal oxidation of copper at 380 °C (circle) and 900 °C (star) after Vila et al. in the spectral range of defects [95].*

increases by more than one order of magnitute matching the optical band gap reported in literature. According to its absorption coefficient, paramelaconite seems to be a semiconductor with a slightly higher optical band gap.

3.1.2.2 Luminescence of tenorite

In the literature there are no reports about photoluminescence spectra of tenorite bulk material or films. Recently, several luminescence bands between 1 eV and 4 eV were observed for tenorite nanostructures, e.g. [96, 95] and tenorite films prepared by spark discharge [97]. However, X-ray photoelectron spectra and XRD measurements reveal that the samples are not phase pure tenorite but also contain cuprite which could be responsible for the detected emission bands. Vila et al. performed cathodoluminescence measurements (CL) on tenorite nanowires at 90 K (cf. figure 3.9, circle and star). He detects emission bands below 1.4 eV and ascribes them to near band gap transitions of tenorite which are probably related to defects. However, XRD measurements clearly document the presence of cuprite. Therefore, the origin of the emission bands is debatable.

3.1.2.3 Raman modes of tenorite and paramelaconite

There are four atoms in the primitive cell of tenorite. Hence, there are twelve normal modes. Three Raman and three IR active modes are expected. Several groups investigated the Raman characteristics experimentally yielding consistently

values of 298 cm^{-1}, 345 cm^{-1}, and 632 cm^{-1} [81, 82, 83]. In contrast to that, the vibrational modes of paramelaconite are mostly unknown. Due to 14 atoms in its primitive unit cell 42 vibrational modes are expected [86]. Meyer et al. report five Raman modes, which were found in experiment, peaked at 175 cm^{-1}, 280 cm^{-1}, 320 cm^{-1}, 530 cm^{-1}, and 610 cm^{-1} [28]. However, some of these modes could also be attributed to cuprite or tenorite. Recently, the vibrational properties of tenorite and paramelaconite were derived by first-principle calculations and compared to experimental results [84]. The theory predicts six active Raman modes at 320 cm^{-1}, 448 cm^{-1}, 484 cm^{-1}, 506 cm^{-1}, 521 cm^{-1}, and 627 cm^{-1}, whereas the experiment reveals only four peaks at 318 cm^{-1}, 510 cm^{-1}, 541 cm^{-1}, and 651 cm^{-1}. Further work is necessary to clearly identify and assign the Raman modes of paramelaconite. Table 3.1 summarizes the Raman modes of the different copper oxide phases.

3.2 The physics of iron oxides

There exist a variety of sixteen different iron oxide and hydroxide compounds [5]. Prevalently, iron(III)-oxide (Fe_2O_3) can be found in nature. This compound exists in two polymorphs namely hematite (α-Fe_2O_3) and maghemite (γ-Fe_2O_3). Hematite is the only iron oxide phase which is stable at standard conditions[1]. Besides, the phases wustite (FeO) and magnetite (Fe_3O_4) occur. Wustite is rarely found in nature in its real stoichiometry. Naturally, the off-stochiometric compositions $Fe_{1-x}O$ (1-x $\in [0.83; 0.95]$) occur, which are also referred to as wustite in the literature. Iron oxides tend to form iron hydroxides, e.g. Goethite (α-FeOOH), akaganéite (β-FeOOH), lepidocrocite (γ-FeOOH), and feroxyhyte (δ'-FeOOH).
In the course of this thesis, hematite and maghemite nanoparticles are investigated. Hence, mainly the structural, optical, and electronic properties, as well as the Raman active vibrational modes of these two polymorphs are presented.

3.2.1 Structure and magnetism of Hematite, maghemite, and magnetite

Hematite (α-Fe_2O_3) possesses a rhombohedral symmetry pertaining to a corundum structure [98]. The iron ions of hematite exist exclusively in the Fe^{3+} oxidation state. The structure of hematite can be described as a stacking of octahedrally coordinated sheets of Fe^{3+} ions, which are separated by close packed double layers of O^{2-} oxygen ions. Between the Morin transition temperature (260 K) and its Néel temperature (950 K), hematite shows a weakly antiferromagnetic magnetism [99].
Magnetite (Fe_3O_4) shows an inverse cubic spinel structure wherein the oxygen atoms form a fcc lattice and the iron atoms occupy tetrahedral (Fe^{2+}) and octahedral (Fe^{3+}) sites [5]. Its structure can be written as

$$Fe^{2+}Fe_2^{3+}O_4$$

Magnetite is one of the first discovered elements showing magnetism. It is found to show ferrimagnetic behaviour at room temperature, which is attributed to the coupling of its iron $3d$ electrons [5].
Maghemite (γ-Fe_2O_3) is equal to hematite in terms of his composition, but its physical structure resembles magnetite. Its structure can be described as a fully oxidized and Fe^{2+} deficient magnetite and exhibits consequently a spinel structure with ferrimagnetic behaviour [5, 100]. Its composition can be written as follows

$$\left(Fe_8^{3+}\right)_A \left[Fe_{40/3}^{3+}\square_{8/3}\right]_B O_{32}$$

[1] 273.15 K and 1013.25 hPa

Here, the indices A and B indicate tetrahedral and octahedral positions, respectively. □ represents vacancies [5].

3.2.2 Electronic structure of the hematite and maghemite

The electronic properties of hematite and maghemite, which were derived from self consistent field Xα scattered wave molecular orbital calculations, are governed by their partially occupied iron 3d orbitals [101]. In this method, the electronic structure is approximated by atomic clusters, which represent characteristic units of the crystal. The electronic structure of maghemite is deduced on the basis of an octahedral $(FeO_6)^{9-}$ and a tetragonal $(FeO_4)^{5-}$ cluster, whereas a slightly, trigonally distorted $(FeO_6)^{9-}$ cluster is assumed for hematite. Only, slight differences between the two $(FeO_6)^{9-}$ clusters are revealed, which result from orbital splitting due to the distortion of the trigonally $(FeO_6)^{9-}$ cluster. Hence, merely the octrahedral and tetragonal clusters are described subsequently. Figure 3.10 shows the spin-unrestricted molecular orbital diagrams of the octahedral $(FeO_6)^{9-}$ (a) and tetragonal $(FeO_4)^{5-}$ (b) clusters after Sherman [101]. The energy levels are those of the oxygen 2p and iron 3d bands and are labeled according to their irreducible representation of the O_h ($(FeO_6)^{9-}$) and T_D ($(FeO_4)^{5-}$) space groups. Each diagram is separated into a spin-up (↑) and spin-down (↓) region. Furthermore, the energy levels are grouped to its major orbitals, namely iron 3d and oxygen 2p orbitals. Due to the covalent bonding, the iron 3d levels show components of oxygen 2p orbitals. Likewise, the oxygen 2p levels contain iron 3d, 4s, and 4p components. The 3d electrons are localized on the iron atoms and lose degeneracy due to the electrostatic interaction with the octahedral crystal field.
Several transitions in the near IR to the near UV can be classified into four categories. Firstly, transitions that arise from the 3d electrons are referred to as *ligand field* (or crystal field) transitions. Secondly, so called *ligand to metal charge transfer* transitions describe transitions between the oxygen 2p and the iron 3d orbitals. Thirdly, at significantly higher energies, *metal to conduction band* transitions from iron 3d to iron 4s or 4p orbitals are possible. Lastly, the magnetic coupling between Fe^{3+} cations allows the simultaneous excitation of two cations by one photon. This *pair excitation* appears at an energy of about the sum of two simple iron 3d ligand field transitions.
The presented results describe the electronic structures of the electronic states in terms of one-electron orbitals. However, solids molecules, multielectronic wavefunctions have to be considered. In general, each electronic structure over one-electron orbitals corresponds to several multielectronic states, which are called multiplets. According to the multiplet theory, the irreducible representation of a multiplet is given by the direct product of the one-electon orbitals [102]. The ground-state

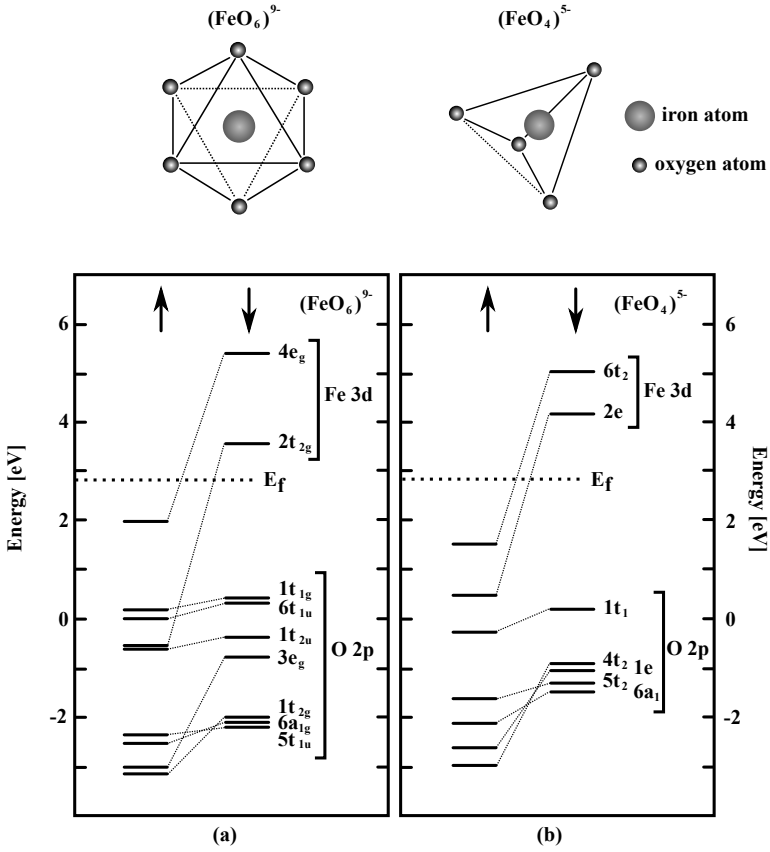

Figure 3.10 – *Molecular orbital diagrams of $(FeO_6)^{9-}$ (a) and $(FeO_4)^{5-}$ (b) cluster without considering spin-restrictions after Sherman [101]. The arrows indicate the spin-up (↑) and spin-down (↓) orbitals. The energy levels are labeled according to their irreducible representation of the O_h ($(FeO_6)^{9-}$) and T_D ($(FeO_4)^{5-}$) space groups and are classified to their major orbital component (O 2p or Fe 3d). On top of each diagram a schematic drawing of the corresponding atom cluster is given.*

Table 3.2 – *Calculated one-electron and corresponding spectroscopic optical transitions of the Fe^{3+} oxides after Sherman [101]. The abbreviations LF and LMCT indicate ligand field and ligand to metal charge transfer transitions, respectively.*

$(\mathbf{FeO}_6)^{9-}$			
One-electron transition	Energy [eV]	Corresponding spectroscopic transitions	Comment
$6t_{1u}^{\downarrow} \rightarrow 4e_g^{\downarrow}$	6.44	${}^6A_{1g} \rightarrow {}^6T_{1u}, {}^6T_{2u}$	LMCT
$1t_{2u}^{\downarrow} \rightarrow 2t_{2g}^{\downarrow}$	5.41	${}^6A_{1g} \rightarrow {}^6A_{1u}, {}^6E_u, {}^6T_{1u}, {}^6_{2u}$	LMCT
$6t_{1u}^{\downarrow} \rightarrow 2t_{2g}^{\downarrow}$	4.72	${}^6A_{1g} \rightarrow {}^6A_{2u}, {}^6E_u, {}^6T_{1u}, {}^6_{2u}$	LMCT
$2t_{2g}^{\uparrow} \rightarrow 2t_{2g}^{\uparrow}$	3.63	${}^6A_{1g} \rightarrow {}^4E_g, {}^4A_{1g}({}^4G), {}^4T_{2g}({}^4D)$	LF
$4e_g^{\uparrow} \rightarrow 4e_g^{\downarrow}$	3.15	${}^6A_{1g} \rightarrow {}^4E_g, {}^4E_g({}^4G),$ ${}^4T_{1g}({}^4P), {}^4A_{2g}({}^4F)$	LF
$4e_g^{\uparrow} \rightarrow 2t_{2g}^{\downarrow}$	1.38	${}^6A_{1g} \rightarrow {}^4T_{1g}({}^4G), {}^4T_{2g}({}^4G)$	LF
$(\mathbf{FeO}_4)^{5-}$			
One-electron transition	Energy [eV]	Corresponding spectroscopic transitions	Comment
$1t_1^{\downarrow} \rightarrow 2e^{\downarrow}$	5.01	${}^6A_1 \rightarrow {}^6T_1, {}^6T_2$	LMCT
$2e^{\uparrow} \rightarrow 2e^{\downarrow}$	3.22	${}^6A_1 \rightarrow {}^4E, {}^4A_1({}^4G), {}^4T_2({}^4D)$	LF
$6t_2^{\uparrow} \rightarrow 6t_2^{\downarrow}$	2.85	${}^6A_1 \rightarrow {}^4E({}^4D), {}^4T_1({}^4P), {}^4A_2({}^4F)$	LF
$6t_2^{\uparrow} \rightarrow 2e^{\downarrow}$	2.01	${}^6A_1 \rightarrow {}^4T_1({}^4G), {}^4T_2({}^4G)$	LF

electronic configuration of the octahedrally coordinated iron Fe^{3+} ions is given by $(2t_{2g})^3(4e_g)^2$, which groups to 21 multiplets with the irreducible representation

$$3({}^2A_2) + 3({}^2E) + 4({}^2T_1) + 4({}^2T_2) + 2({}^4E) + {}^4T_1 + {}^4T_2 + {}^4A_1 + {}^4A_2 + {}^6A_1$$

Table 3.2 sumarizes the calculated one-electron and the corresponding spectroscopic transitions of the Fe^{3+} oxides after Sherman [103]. Moreover, Sherman et al. investigated the electronic spectra of Fe^{3+} oxides in the near IR to the near UV, experimentally [103]. Table 3.3 gives an overview about the detected transition energies and assignments for the hematite as well as maghemite phase. Below 4.5 eV the observed transitions are attributed to ligand field and double excitation processes. The first ligand to metal charge transfer transition is observed at 4.59 eV (hematite) and 4.96 eV (maghemite).

Table 3.3 *– Observed and calculated transition energies and assignments of hematite and maghemite after Sherman et al. [103].*

Detected (calculated) transition energies [eV]		
Transition	**Hematite**	**Maghemite**
$^6A_1 \rightarrow ^4T_1(^4G)$	1.40 (1.40)	1.32 (1.32)
$^6A_1 \rightarrow ^4T_2(^4G)$	1.91 (1.91)	1.86 (1.85)
$^6A_1 + ^6A_1 \rightarrow ^4T_1(^4G) + ^4T_1(^4G)$	2.34 (–)	2.43 (–)
$^6A_1 \rightarrow ^4E, ^4A_1(^4G)$	2.79 (2.79)	2.85 (2.86)
$^6A_1 \rightarrow ^4T_2(^4D)$	3.06 (2.99)	– (3.08)
$^6A_1 \rightarrow ^4E(^4D)$	3.26 (3.26)	3.35 (3.35)
$^6A_1 \rightarrow ^4T(^4P)$	3.88 (4.23)	3.93 (4.36)
$6t_{1u} \rightarrow 2t_{2g}$ (LMCT)	4.59 (–)	4.96 (–)

3.2.3 Absorption coefficient of hematite and maghemite

Hematite is a semiconductor with an optical band gap of about 2.1 eV, which is estimated from the onset of the photocurrent, and absorption measurements [104, 107, 108, 109, 110]. Figure 3.11 (a) illustrates the absorption coefficient of a hematite thin film between 1.5 eV and 4.5 eV (red circles) [104]. The steep increase by about two orders of magnitute of the absorption coefficient between 2.0 eV and 2.2 eV indicate the optical band gap. Figure 3.11 (b) shows the absorption characteristics of a hematie single crystal in the near IR (red circles). Several absorption bands (labeled as A, B, C, D, E, and F) appear as humps or maxima on the curvature of the absorption coefficient. The absorption of hematite begins in the near IR region (cf. figure 3.11 (b)) and is formed by transitions between the $3d$ electrons of the Fe^{3+} ions. Since the transitions are parity and spin forbidden, phonons or magnons are involved. As discussed in section 3.2.2, the $3d$ orbitals of the iron ions split into two orbitals due to the crystal field arising from the separation between the O^{2-} and Fe^{3+} ions. On the basis of the calculations performed by Tossel et al., transitions with energies lower than 2.5 eV (A,B,C, and D) were ascribed to these crystal field transitions. On the other hand, the transitions above 2.5 eV (D, E, and F) are believed to arise from spin-flip or ligand to metal charge transfer transitions from O^{2-} to Fe^{3+} ions [111]. According to Sherman, these bands assignments are partly incorrect due to too low calculated energies for the ligand to metal charge transfer transitions [101]. In his work, the lowest ligand to metal charge transfer transition of maghemite is predicted at about 4.59 eV. Though the assignments of the structures is ambigeous, a fairly good agreement between theory and experiment is observed. The transition A* is possibly related to a pure exciton transiton [112].
Maghemite is also a semiconductor with an optical band gap of about 2 eV [5].

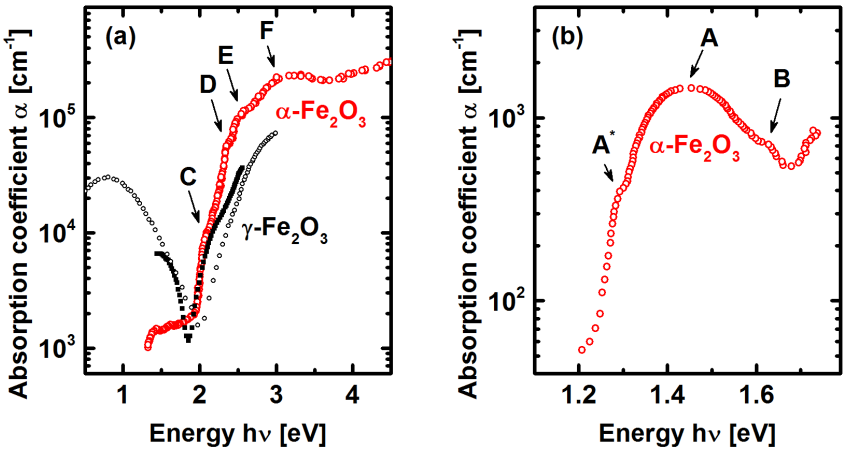

Figure 3.11 – *Absorption coefficient of hematite thin films in the spectral region of the near IR to the UV (a) and of single crystals in the near IR (b) after Marusak et al. (red circles) [104]. Figure (a) also shows the absorption coefficient of maghemite thin films after Babkin et al. (black circle) and Wang et al. (black square) [105, 106].*

Compared to the hematite phase, there are less reports about its optical properties. Figure 3.11 (a) also presents the absorption coefficient of maghemite thin films after Babkin et al. (black circle) and Wang et al. (black square) [105, 106]. The two spectra differ slightly, but exhibit similar features. As mentioned in section 3.2.1, the structure of maghemite can be described as a Fe^{2+} deficient magnetite phase. Depending on the preparation conditions, the vacancies order in superstructures (tetragonal or tetrahedral) or occur in a disordered distribution [113, 114, 115]. In conclusion, the optical properties also depend on the preparation technique. The optical band gap of maghemite is indicated by the increase of the absorption between 2 eV and 2.5 eV. An absorption feature at about 2.1 eV is observed, which can be explained by the ligand field transitions of the iron 3*d* electrons.

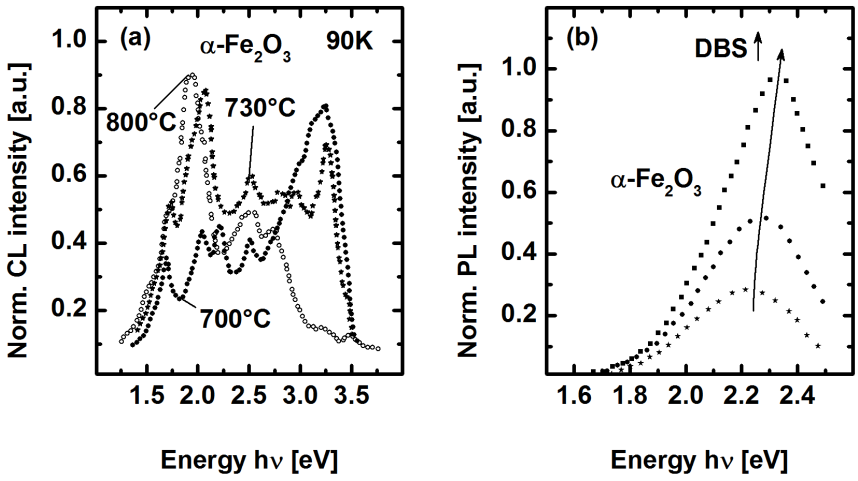

Figure 3.12 *– (a) cathodoluminescence spectra (CL) at 90K of hematite nanowires after Chioncel et al. [116]. The nanowires are prepared by oxidation of iron at 700° C (circle), 730° C (star), and 800° C (open circle). (b) PL spectra of hematite nanoparticles, which are coated with sodium dodecyl/benzene sulphonic (DBS) after Fei et al. [117]. The arrow indicate an increasing DBS concentration at the surface of the nanoparticles.*

3.2.4 Luminescence of hematite and maghemite

In the literature, there are no reports about the luminescence of hematite and maghemite bulk material. The strong localization of the $3d$ electrons accompanied by the forbiddance of the $d - d$ transitions, magnetic relaxations, and energy transfer between cations and the lattice are usually considered as the reasons why no luminescence could be detected [116, 119, 120, 121]. However, several groups reported the observation of luminescence of iron oxide nanostructures in the region between 1.5 eV and 3.5 eV [116, 119, 120, 117, 122, 123]. The occurrence of luminescence is probably related to the reduced size, which comes along with a higher surface to volume ratio. In the literature it is believed, that the ferromagnetic long range order is disturbed, the density of the electronic population is altered (more iron $3d$ $4sp$ hybridization), the forbiddance of the $d - d$ transition is weakened, a different defect structure establishes, the electron phonon coupling is enhanced, and the charge carriers are more delocalized, so that the non-radiative recombination is reduced [116, 119]. Figure 3.12 (a) shows cathodoluminescence spectra (CL) of hematite nanowires that are prepared by oxidation of iron at different temperatures after Chioncel et al. [116]. Complex emission spectra are observed, with emission peaks at about 1.8 eV, 2.1 eV, 2.3 eV, 2.6 eV, 3.0 eV, and 3.3 eV, which are

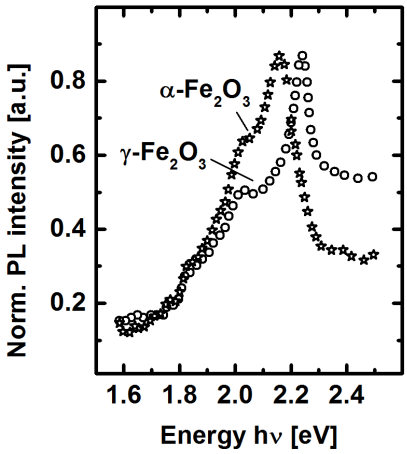

Figure 3.13 *– PL spectra of hematite (star) and maghemite (circle) nanowire band edge emission after Han et al. [118].*

attributed to the different ligand field, double excition, and ligand to metal charge transfer transitions. The intensities of the respective emission peaks depend strongly on the oxidation temperature.
Moreover, the surface of the nanoparticles plays a crucial role concerning the emission properties of hematite nanoparticles. Fei et al. detect PL signals of hematite nanoparticles, which are coated by sodium dodecyl/benzene sulphonic (DBS) (cf. figure 3.12 (b)) [117]. No emission is detected for bare hematite nanoparticles, but, when the surface of the nanoparticles is coated with DBS, an emission band is detected at about 2.2 eV, and attributed to hematite band edge emission. The emission intensity increases with increasing DBS content on the surface. The surface is believed to exhibit OH and $(OH)_2$ endgroups, which are substituted by SO_3-PH. Since the DBS repels electrons, a gradient of the electric field is established, which leads to a delocalization of the iron $4s$ and $4p$ orbitals. Moreover, the emission peak shifts to higher energies with increasing DBS concentration, but no explanation is given in the literature.
Figure 3.13 depicts PL spectra of hematite (star) and maghemite (circle) nanowires after Han et al. [118]. The most pronounced emission bands at about 2.15 eV (hematite) and 2.24 eV (maghemite) are attributed to the respective band edge transitions.

Wang et al. detected a weak near IR emission signal of commercially available hematite microparticles with different morphologies (platelets, polyhedral, and pseudocubes) that are prepared via hydrothermal synthesis [120]. Figure 3.14 (a) illustrates some of the detected emission spectra of the as-prepared nanoparticles with polyhedrical (star) and platelets like (circle) morphology. All emission signals seem

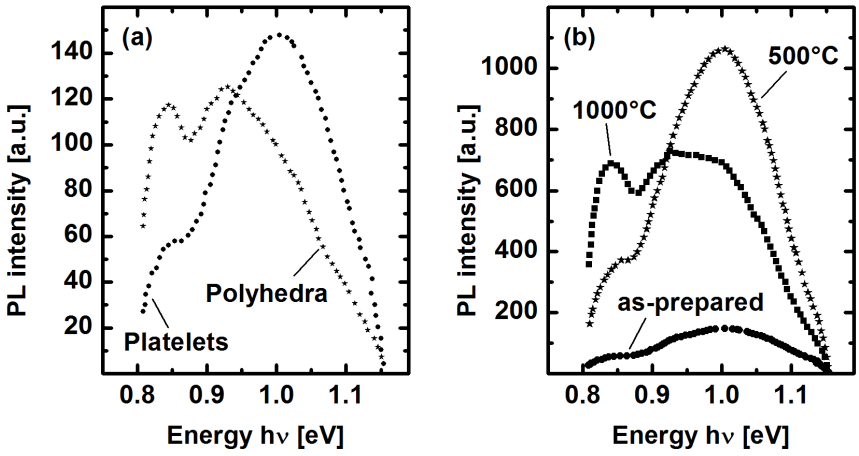

Figure 3.14 *– (a) PL spectra of polyhedrally (star) and platelets like (circle) shaped hematite microparticles after Wang et al. [120]. (b) PL spectra of the platelets shaped hematite particles in the as-prepared state (circle) and after annealing at 500° C (star) and 1000° C (square).*

to be composed of several emission bands at about 0.83 eV, 0.91 eV, and 1 eV. The respective intensities of these bands depend on the morphology of the particles. The emission intensity is found to increase after annealing at temperatures between 500 °C and 1000 °C (cf. figure 3.14 (a)), whereas the emission changes after the annealing at 1000 °C. The origin of the bands and the dependence of the emission on the morphology is unclear. Wang et al. suggest defects or the ${}^6A_1 \rightarrow {}^4\ T_1({}^4G)$ ligand field transitions to be responsible for the emission. Hematite is known to be slightly non-stoichiometric [124]. Possibly defects such as oxygen vacancies or impurities that function as activators contribute to the near IR emission [120].

3.2.5 Raman modes of hematite, maghemite, magnetite, and wustite

Hematite belongs to the D_{34}^6 space group. Factor group analysis predicts seven Raman active modes for hematite. Experimentally, all seven frequencies 226 cm^{-1}, 245 cm^{-1}, 293 cm^{-1}, 298 cm^{-1}, 413 cm^{-1}, 500 cm^{-1}, and 612 cm^{-1} are found [125, 126, 127, 128]. Besides, a broader structure at ca. 1320 cm^{-1} is observed in the Raman spectrum of hematite. Its origin is controversly discussed in the literature. Some groups identify this feature with a collective spin movement due to the antiferromagnetic behaviour of hematite. Therefore, the signal is attributed to a two-magnon scattering process [129, 130, 131]. An alternative approach suggest the simultaneous excitation of two phonons to account for this Raman band [132, 133].
The Raman spectrum of **maghemite** is also agreed upon the literature. In contrast to hematite, the maghemite bands are not well defined. Three broad structures centered at around 350 cm^{-1}, 500 cm^{-1}, and 700 cm^{-1} are assigned to maghemite [127, 128, 125]. The feature at 700 cm^{-1} shows a double peak structure with peaks located at about 670 and 720 cm^{-1}. Moreover, several groups report a broad Raman mode between 1400 cm^{-1} and 1600 cm^{-1}; e.g. [128]. Its origin is not explained in the literature and remains unclear so far.
Magnetite (Fe_3O_4) shows a O_h^7 structure for temperatures higher than 119 K. Five Raman active modes are expected. The characteristic magnetite Raman frequencies are not clearly identified and there are some disagreements in the literature. Some groups report frequencies close to characteristic hematite Raman modes. According to DeBoer et al., magnetite undergoes a phase transition when heated [134].

$$Fe_3O_4 \overset{200\,^\circ C}{\rightarrow} \gamma\text{-}Fe_2O_3 \overset{400\,^\circ C}{\rightarrow} \alpha\text{-}Fe_2O_3 \tag{3.3}$$

This process is called martitization, which is responsible for the different Raman modes that are reported in the literature for the magnetite phase. For instance Faria et al. [128] and Shebanova et al. [135] show the influence of laser induced thermal effects during Raman measurements. They observe Raman peaks which are characteristic for hematite due to laser irradiation. One mode located at ca. 661 cm^{-1} is agreed upon in the literature [128, 135, 130, 127, 125, 136]. Merely the exact position is not clear. It is reported between 661 cm^{-1} and 676 cm^{-1}. If the band is reported above 670 cm^{-1}, other bands at wavenumbers lower than 500 cm^{-1} are also observed which can be attributed to hematite. Hence, the shift to higher wavenumbers possibly indicates the onset of transformation. Most groups report a second frequency at 532 cm^{-1} to 550 cm^{-1}. From the results of the groups, who reduced a significant influence of laser heating, the three Raman frequencies 532 cm^{-1}, 550 cm^{-1}, and 661 cm^{-1} can clearly be assigned to the magnetite phase. Moreover, Hart et al. find a very weak feature at 472 cm^{-1} and attributed it to a single magnon process [130]. This finding and interpretation is in good agreement with neutron

diffraction data which predict such a magnon excitation at $468 \pm 8\,\mathrm{cm}^{-1}$ [137].
Wustite has a cubic crystal structure at temperatures above 198 °C and a rhombohedral one below [5]. Its characteristic Raman frequencies are not finally identified. Under laser illumination wustite decomposes easily into magnetite and elementary iron [5]. Faria et al. detect a peak located at $652\,\mathrm{cm}^{-1}$ [128]. In comparison to the most intensive Raman frequency in the magnetite spectrum, this peak is shifted to lower wavenumbers and significantly broadened. Furthermore, the two other characteristic magnetite Raman frequencies at $310\,\mathrm{cm}^{-1}$ and $536\,\mathrm{cm}^{-1}$ are not observed. Hanesh et al. assign two peaks at $595\,\mathrm{cm}^{-1}$ and $670\,\mathrm{cm}^{-1}$ to the wustite phase [125]. Table 3.4 summarizes the characteristic Raman frequencies of hematite, maghemite, magnetite, and wustite. Moreover, figure 3.15 shows representative Raman spectra of the hematite (a), maghemite (a), magnetite (b), and wustite (b) phase taken from de Faria et al. [128].

Table 3.4 *– Experimental Raman frequencies of hematite, maghemite, magnetite, and wustite [125, 127, 128, 130, 135, 136]. The Raman frequencies are presented in wavenumbers (cm^{-1}) and the strongest intensities in the experimental data are indicated by bolt type.*

Hematite	Maghemite	Magnetite	Wustite
226	350	310	595
245	500	472	**652-670**
293	670-720	536	
298		**660-670**	
413		1400-1600	
500			
612			
1320			

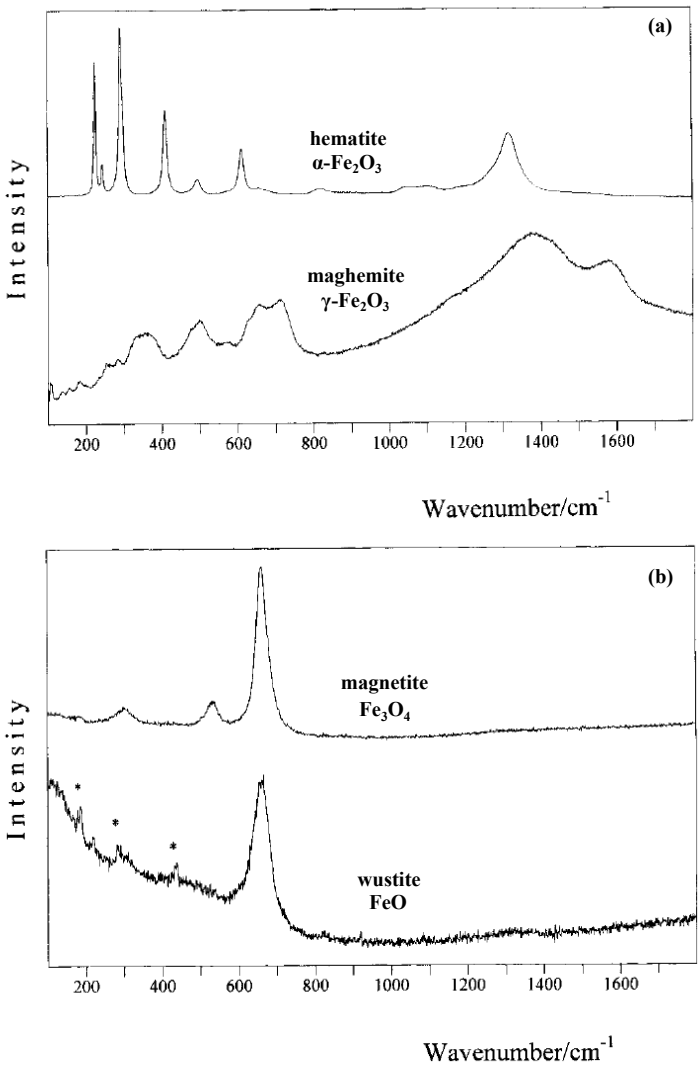

Figure 3.15 *– (a) Raman spectra of hematite and maghemite as well as (b) Raman spectra of magnetite and wustite (asterisk indicates artifacts) taken from de Faria et al. [128].*

Chapter 4

Characterization & modification of copper oxide nanoparticles

This chapter is dedicated to the characterization and modification of commercially available tenorite nanoparticles, which are purchased as powder from IoLiTec GmbH[1]. In the context of the present thesis, two diploma theses were completed. Their main results are briefly summarized in the beginning of this chapter. Afterwards, PL, Raman, PDS, TEM, and XRD results for oven annealed tenorite nanoparticles are presented. The nanoparticles are annealed up to 1000° C in nitrogen atmosphere as well as in air. The modifications of the (micro-)structural and opto-electronic properties are investigated by Raman and PL spectroscopy. On the same sample several sample spots are analyzed in order to reveal local inhomogeneities. Moreover, the influence of the laser irradiation during the measurement is investigated. Furthermore, the optical absorption is characterized by PDS. After selected annealing steps, TEM and XRD measurements are performed.

4.1 Summary of the related diploma theses

Jan Flohre showed in his diploma thesis that tenorite nanoparticles can be significantly improved by laser annealing in ambient air [21]. Raman and PL measurements were carried out at room temperature to analyze the structural and electronic changes. Firstly, the properties of the as-prepared material were investigated with a low laser excitation power of about $2.9\,\mathrm{Wcm^{-2}}$. Then, the same spot was irradiated with a laser power of about $12\,\mathrm{Wcm^{-2}}$ for ten minutes. Afterwards, the Raman and PL measurements were repeated with a laser excitation power of $2.9\,\mathrm{Wcm^{-2}}$. In the

[1] http://www.iolitec.de/

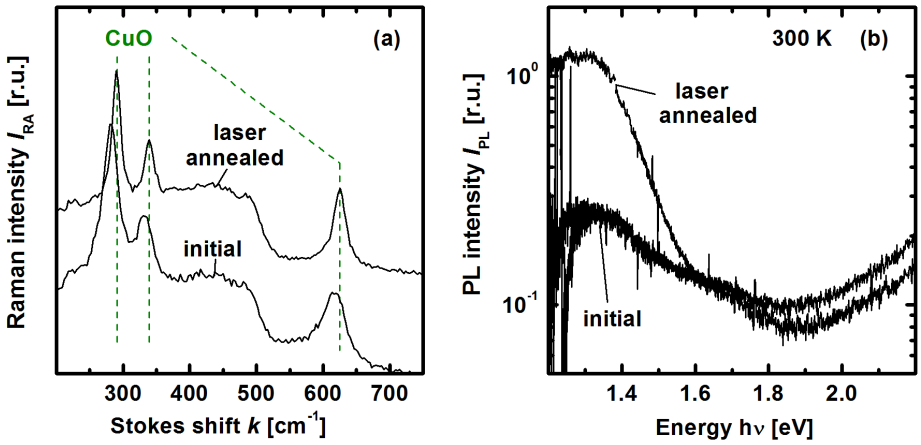

Figure 4.1 – *Raman (a) and PL (b) spectra at room temperature (300 K) after Flohre [21]. The spectra were taken on the same spot before and after a laser treatment with a laser excitation power of 12 Wcm^{-2} for ten minutes in air. Note, that the PL intensity is presented on a logarithmic scale. References for the tenorite Raman modes of bulk material are indicated by dashed lines [81].*

as-prepared state, the Raman spectrum exhibited typical tenorite Raman modes (cf. figure 4.1). Compared to bulk material, the line shape was broader and the positions were red-shifted [81, 82, 83]. Width and position of the Raman signals suggested stress and a high defect concentration within the nanoparticles. After the laser annealing step, a narrowing of the tenorite Raman modes was observed accompanied by a shift to higher wavenumbers which were comparable to values reported in the literature for bulk material. These variations indicated, that defects were annealed and stress was relaxed leading to an improvement of the structural properties. Furthermore, the PL signals changed significantly. The PL signal of the as-prepared sample exhibited a weak signal at about 1.3 eV which is in good agreement with the position of the optical band gap of tenorite copper oxide [89, 90, 91]. After the laser annealing, the PL intensity at about 1.3 eV increased by a factor of five. This increase was explained by a reduction of the defect concentration, which led to less non-radiative recombination and was consistent with the Raman results.

In a second diploma thesis, Jens Bergmann investigated the influence of laser and oven annealing in nitrogen atmosphere on the properties of tenorite nanoparticles [22]. In the course of his thesis, the experimental Raman and PL setup was partially automated and extended by an InGaAs detector, which allowed to measure the PL spectra also in the infrared region. In order to investigate the influence of laser annealing in nitrogen atmosphere, the sample was placed in a container that was filled with nitrogen, and irradiated with a laser power of about 14 Wcm^{-2}.

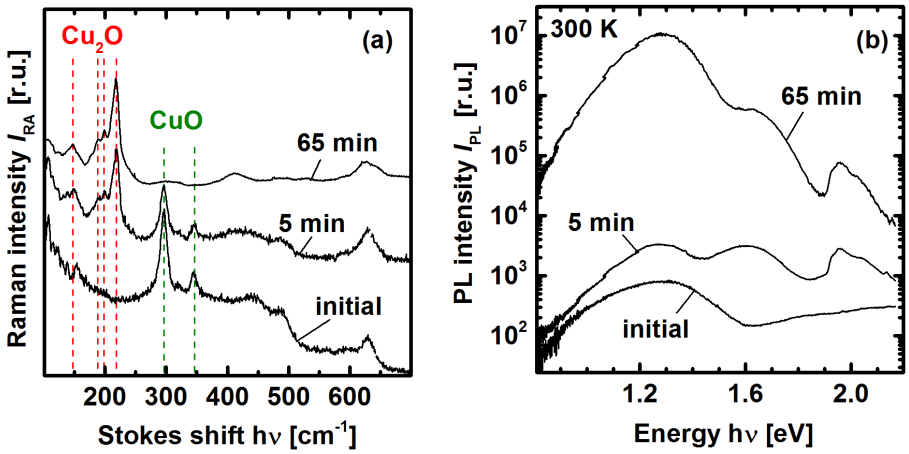

Figure 4.2 – *Raman (a) and PL (b) spectra of tenorite nanoparticles at room temperature (300 K) in the as-prepared state and after exposition to a laser power of about 14 Wcm^{-2} for 5 and 65 minutes in nitrogen atmosphere. The spectra were taken from the same spot with a laser power of 2.5 Wcm^{-2} (after Bergmann [22]). Note, that the PL intensity is presented on a logarithmic scale. The main tenorite and cuprite Raman modes are indicated by green and blue dashed lines, respectively [81, 77].*

After 5 and 65 minutes of irradiation, the laser power was reduced to 2.5 Wcm^{-2} to perform PL and Raman measurements at room temperature (RT) (cf. figure 4.2). In contrast to the laser treatment in Jan Fohre's diploma thesis, a phase transition from tenorite to cuprite is observed. The different behaviour can be explained by the lower oxygen partial pressure due to the nitrogen atmosphere leading to a lower phase transition temperature as expected from the stability diagram (cf. figure 3.1). The as-prepared sample showed tenorite Raman modes and tenorite band edge emission with its maximum at about 1.3 eV. After five minutes of irradiation, additional Raman peaks were detected, which are characteristic for cuprite. This indicated that the tenorite nanoparticles were partially tranformed into cuprite. The transformation was also visible in the PL signal. The corresponding PL spectrum exhibited three luminescence bands at about 1.2 eV, 1.6 eV, and 2 eV. The band at 2 eV showed a characteristic fine structure which was attributed to exciton related transitions of cuprite. The bands at 1.6 eV and 1.2 eV were explained by defect emission in cuprite, and a superposition of defect transitions and tenorite band edge emission, repectively [60, 72, 71, 70]. After increasing the annealing time, the cuprite Raman signal increased and the tenorite Raman modes vanished, suggesting a complete phase transition. However, it could not be excluded that there was still some amount of tenorite present that was not resolved by the Raman measurement

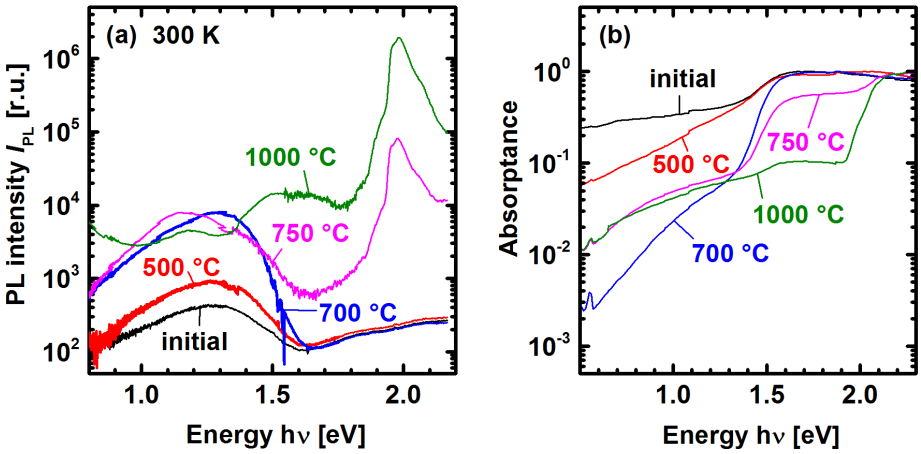

Figure 4.3 – *PL (a) and PDS (b) spectra at room temperature (RT) of copper oxide nanoparticles that were annealed stepwise in nitrogen atmosphere (cf. Bergmann [22]).*

due to a significantly lower Raman cross section for tenorite which was indicated by our experiments. The intensities of the emission signals at 1.3 eV, 1.5 eV, and 2 eV increased by more than three, two, and one order of magnitude, respectively. The dominant emission bands below 1.8 eV indicated defect rich material after the phase transition.

Furthermore, nanoparticles were annealed stepwise up to 1000 °C in an oven under nitrogen atmosphere. Its opto-electronic properties were investigated by PDS and PL spectroscopy at room temperature (RT). Up to an annealing temperature of 700 °C, the structural and electronic properties of the tenorite nanoparticles were improved. A narrowing and shifting of the Raman modes to higher wavenumbers was observed (not shown here), accompanied by a significant increase of the tenorite band edge emission by more than one order of magnitude (cf. figure 4.3 (a)). Consistent with the previous interpretation, this was explained by the release of stress and the annealing of defects. The absorptance of the as-prepared sample increased between 1.4 eV and 1.6 eV which was in good agreement with the optical band gap of tenorite bulk material (cf. figure 4.3 (b)) [89, 90, 91]. Below 1.4 eV, a high sub gap absorption was observed, which was reduced significantly with increasing annealing temperature confirming the interpretation of defect annealing. Various spots were investigated by Raman and PL spectroscopy, revealing a high homogeneity. Slight variations could mainly be attributed to small differences of the setup calibration, and laser power variations. After annealing at 750 °C, only cuprite Raman modes were observed (not shown here). Nevertheless, there is still some remaining tenorite phase material left as was concluded from the PL and PDS spectra (cf. figures 4.3 (a)

and (b)). The increase of the absorptance in the regions around 1.5 eV and 2 eV was ascribed to the optical band gaps of tenorite and cuprite, respectively. Moreover, the PL signal exhibited two pronounced emission bands at 1.3 eV and 2 eV which correlated with the PDS spectrum and were therefore attributed to tenorite and cuprite band edge emissions. After annealing at 1000 °C, the maximum intensity of the emission at 2 eV increased by more than one order of magnitude. Below 1.8 eV a weak emission signal was observed which again could be explained by remaining tenorite phase. Potentially tenorite band edge emission and emissions related to defects were responsible for this signal. The PDS spectrum showed a strong and a weak absorption edge at 2 eV and 1.5 eV, respectively, which indicated that most of the nanoparticles were tranformed into cuprite. The intensity of the band edge emission and particularly the relative intensities of the defect related transitions at lower energies varied drastically when analyzing different spots. This indicated that the phase transformation was not homogeneous. There was no indication if single nanoparticles were only partially tranformed and exhibited both copper oxide phases, or if each nanoparticle is purely present in either the tenorite or the cuprite phase. However, in comparison to the laser transformed nanoparticles, the emission below 1.8 eV was always about two orders of magnitute lower than the pronounced emission at 2 eV. This finding implied, that the nanoparticles which were transformed by oven annealing exhibited a significantly lower defect concentration.

4.2 Pre-examination of tenorite nanoparticles by TEM

Commercially available tenorite (CuO) nanoparticles with a nominal diameter of 40 nm to 80 nm are purchased as powder from IoLiTec GmbH[2]. These nanoparticles are dispersed in deionized water by treatment in an ultrasonic bath. For preliminary TEM measurements a TEM grid[3] is coated with nanoparticles by dipping it into the dispersion and subsequent drying in air. Figure 4.4 (a) and (b) show bright field images of the untreated tenorite nanoparticles. The nanoparticles are not uniform but exhibit large variations in size and shape. According to the TEM images, nanoparticles with a diameter of about 30 nm and few nanoparticles with diameters primarily above 100 nm are found. Figure 4.4 (c) illustrates a representative diffraction pattern corresponding to the bright field image in figure 4.4 (b). The diffractrogram in figure 4.4 (d) was calculated from the angular integration of the pattern in figure 4.4 (c) and shows a multitude of reflexes resulting from the different crystallographic orientations of the nanoparticles, similar to a powder pattern. Reflexes referring to characteristic tenorite lattice distances are observed [85]. There is no indica-

[2]http://www.iolitec.de/
[3]Copper grid with carbon film (Lacey-Carbon)

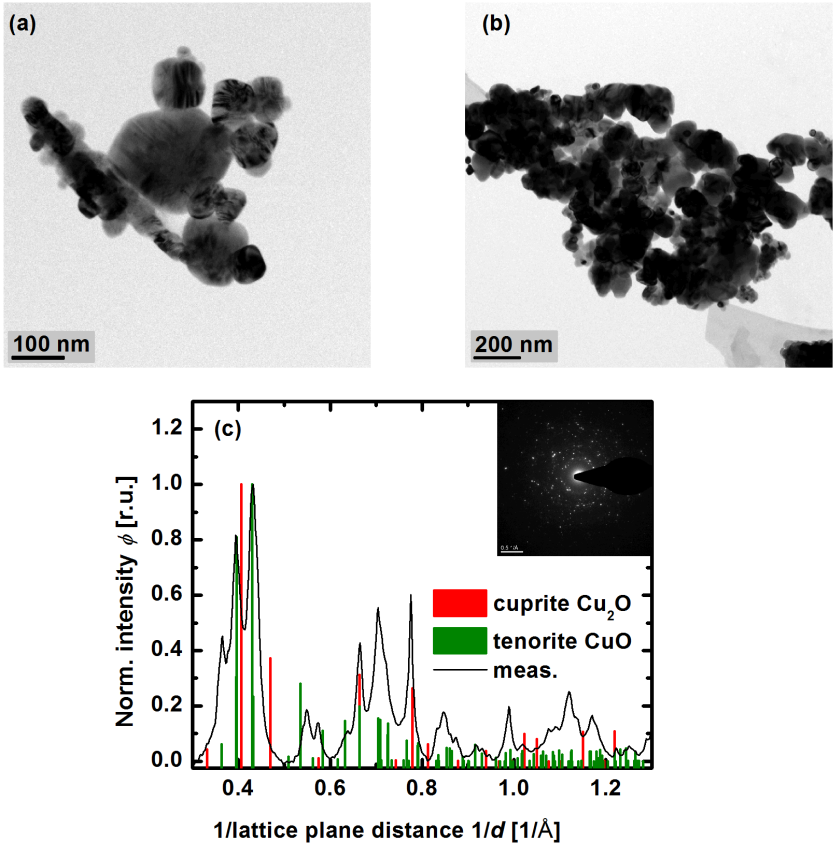

Figure 4.4 – *(a) and (b) TEM bright field images of untreated tenorite nanoparticles at different sample positions. (c) angular integrated diffractogram of the pattern diffraction pattern shown as inset corresponding to the bright field image (b). Reference data for tenorite and cuprite is indicated by green and red bars, respectively [85, 138].*

tion for the presence of cuprite. Within the limits of the TEM measurements, the nanoparticles seem to consist of a highly crystalline tenorite phase.

4.3 Oven annealing of tenorite nanoparticles

Based on the findings in Jan Flohre's and Jens Bergmann's diploma theses, the tenorite nanoparticles are intensively investigated. In the present thesis, tenorite nanoparticles are annealed stepwise in air and nitrogen atmosphere. The impact of this treatment on the opto-electronic and structural properties is analyzed. After each annealing step, Raman, PL, and PDS measurements are performed to analyze the structural and electronic properties of the modified nanoparticles. For each annealing temperature several positions are measured in order to monitor possible local inhomogeneities. After selected annealing steps, XRD and/or TEM patterns are recorded.
Similar to the sample preparation for the preliminary TEM measurements, the tenorite nanoparticles are dispersed in deionized water by treatment in an ultrasonic bath. For Raman, PDS, PL, and XRD measurements, a small volume of the dispersion is applied to quartz substrates (8 nm × 15 nm) and allowed to dry in air. The nanoparticles form larger agglomerates on the substrate leading to an inhomogeneous coverage. After selected modification steps, the nanoparticles are transferred from the quartz substrate onto a TEM grid by stamping the grid onto the quartz substrate that is covered with nanoparticles.

4.3.1 Structural modification

Subsequently, the influence of the oven annealing treatment on the structural properties is discussed. Firstly, representative Raman spectra for each annealing temperature and both annealing atmospheres are presented. The results of the Raman measurements are complemented by XRD diffractograms after selected annealing steps. Finally, TEM measurements of the nanoparticles which are annealed at 1000 °C in air and nitrogen atmosphere are presented.

4.3.1.1 Raman spectroscopy

Figure 4.5 depicts representative Raman spectra for nanoparticles that are annealed stepwise in air, and nitrogen atmosphere. The as-prepared nanoparticles show the three typical tenorite Raman modes at about 298 cm^{-1}, 345 cm^{-1}, and 632 cm^{-1} [81, 82, 83]. The weak feature at 320 cm^{-1} as well as the signal around 500 cm^{-1} can be assigned to the quartz substrate. Besides, no characteristic cuprite signals are detected. In case of annealing in air the general characteristics of the Raman spectrum remain unaffected. On the contrary, after annealing at 800 °C and 1000 °C

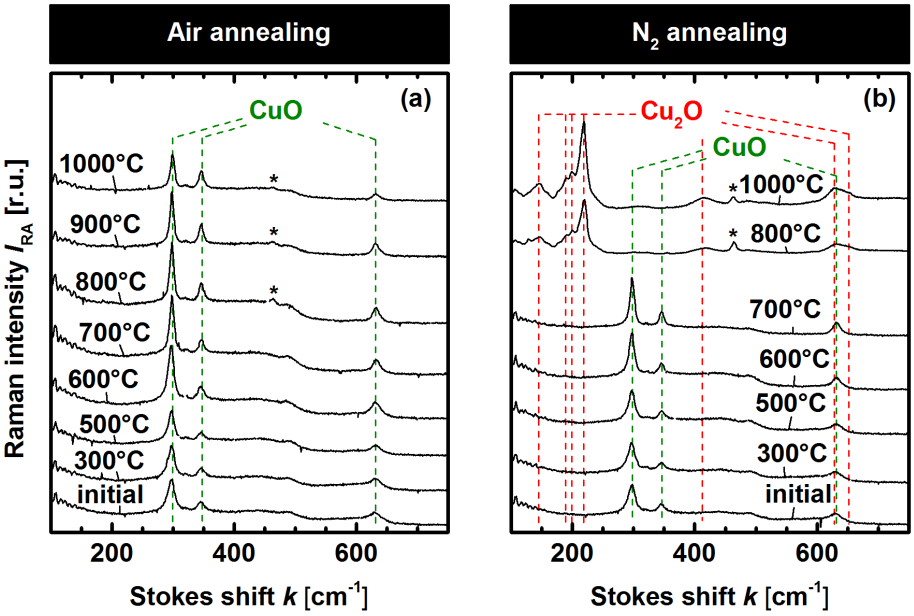

Figure 4.5 – *Representative Raman spectra of copper oxide nanoparticles that are annealed stepwise in air (a) and nitrogen atmosphere (b). Reference data for tenorite and cuprite Raman modes (bulk material) is indicated by green and red dashed lines, respectively [81, 77]. The asterisk (*) indicates the mode of the crystallized quartz substrate.*

in nitrogen atmosphere the nanoparticles are transformed into cuprite, which is confirmed by the detection of cuprite Raman modes, i.e. at about 144 cm^{-1}, 200 cm^{-1}, and 220 cm^{-1}; cf. e.g. [77]. No tenorite Raman modes are visible any more. While the mode at 464 cm^{-1} (*) is explained by the crystallization of the quartz substrate after the high temperature annealing steps, the origin of the broad Raman signal at 300 cm^{-1} is unknown.

With inreasing annealing temperature, the shape and the position of the Raman modes vary. Exemplarily, the main tenorite Raman modes at about 300 cm^{-1} is analyzed in more detail. For this purpose, the samples of both modification series that do not show cuprite Raman modes, are evaluated. This means, that the Raman spectra of the annealing series in nitrogen atmosphere up to an annealing temperature of 700 °C and all Raman spectra of the annealing series in air are regarded. In figure 4.6 the Full Width at Half Maximum (FWHM) (a) and the peak position (b) are plotted against the annealing temperature T_{ann}. Note, that no significant difference between the two series under different annealing atmospheres is observed. Up to an annealing temperature of about 400 °C the FWHM remains nearly constant at

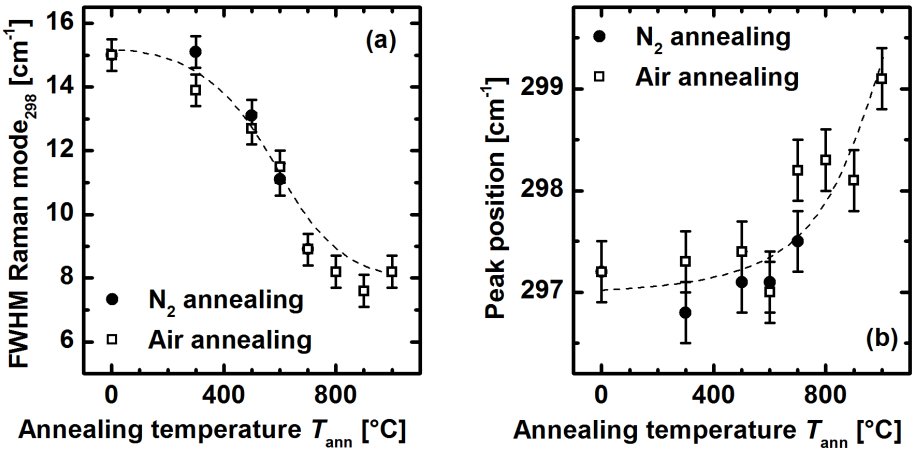

Figure 4.6 *– Full Width at Half Maximum (FWHM) (a) and peak position (b) of the main tenorite Raman mode at about 300 cm^{-1} depending on the annealing temperature. The Raman spectra of the annealing series in nitrogen atmosphere (circle) up to an annealing temperature of 700 °C and all Raman spectra of the annealing series in air (open square) are regarded. The dashed lines are given as a guide to the eye.*

14 cm^{-1} to 15 cm^{-1}. Further annealing up to 800 °C leads to a continuous reduction of the FWHM to 8 cm^{-1} and remains constant up to an annealing temperature of 1000 °C. The narrowing of the peak is accompanied by a shift of the Raman mode from about 297 cm^{-1} to 299 cm^{-1} with increasing annealing temperature.

4.3.1.2 XRD

Figure 4.7 shows diffractograms of the nanoparticles in the as-prepared state and after annealing at 700 °C, 800 °C, and 1000 °C in nitrogen atmosphere and after annealing at 700 °C and 1000 °C in ambient air. In the as-prepared sample the observed reflexes can be assigned to characteristic tenorite lattice planes [85]. After annealing at 800 °C in nitrogen atmosphere, there is no significant indication for a remaining tenorite phase. Characteristic cuprite reflexes are oberseved while further peaks could be assigned to the crystallized quartz substrate, which are labeled by asterisks (*) [138]. Further annealing at 1000 °C does not show further changes. Contrasting, only the typical tenorite and no cuprite reflexes are observed after annealing at 1000 °C in air. Again, the asterisks indicate reflexes that arise from the crystallized quartz substrate.

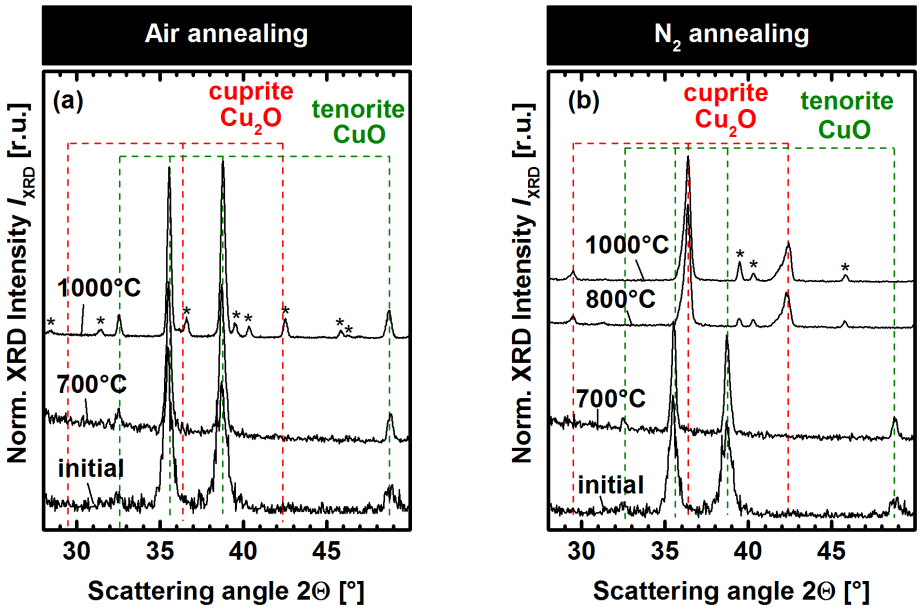

Figure 4.7 – *XRD patterns of the untreated nanoparticles and after annealing different temperatures in air (a) and nitrogen atmosphere (b). Reference data for cuprite and tenorite are indicated by red and green dashed lines, respectively [138, 85]. Substrate reflexes are marked by asterisks *.*

4.3.2 PL and PDS before phase transition

The influence of the annealing steps on the opto-electronic properties of the nanoparticles is analyzed by PL and PDS measurements. The PL spectra are taken at room temperature from the same spots wherefrom the Raman spectra are detected. The figures 4.8 (a) and (c) illustrate the PL signals for the different annealing temperatures on a logarithmic scale. For the samples that are annealed in nitrogen atmosphere, merely the annealing steps before the phase transition are depicted. For each annealing step, a representative PDS signal is also given in the figures 4.8 (b) and (d). For as-prepared tenorite nanoparticles, the PL spectra at room temperature exhibit a peak at about 1.28 eV and a FWHM of about 0.35 eV with an unsymmetric shape, i.e. a slightly steeper decay towards higher energies. The corresponding PDS spectra slightly increase between 0.5 eV and 1.4 eV and then increase further by a factor of three in the region between 1.4 eV and 1.6 eV, before they saturate at higher energies. The value just below the saturation corresponds well to the optical band gap reported in literature for bulk material tenorite [89, 90, 91].

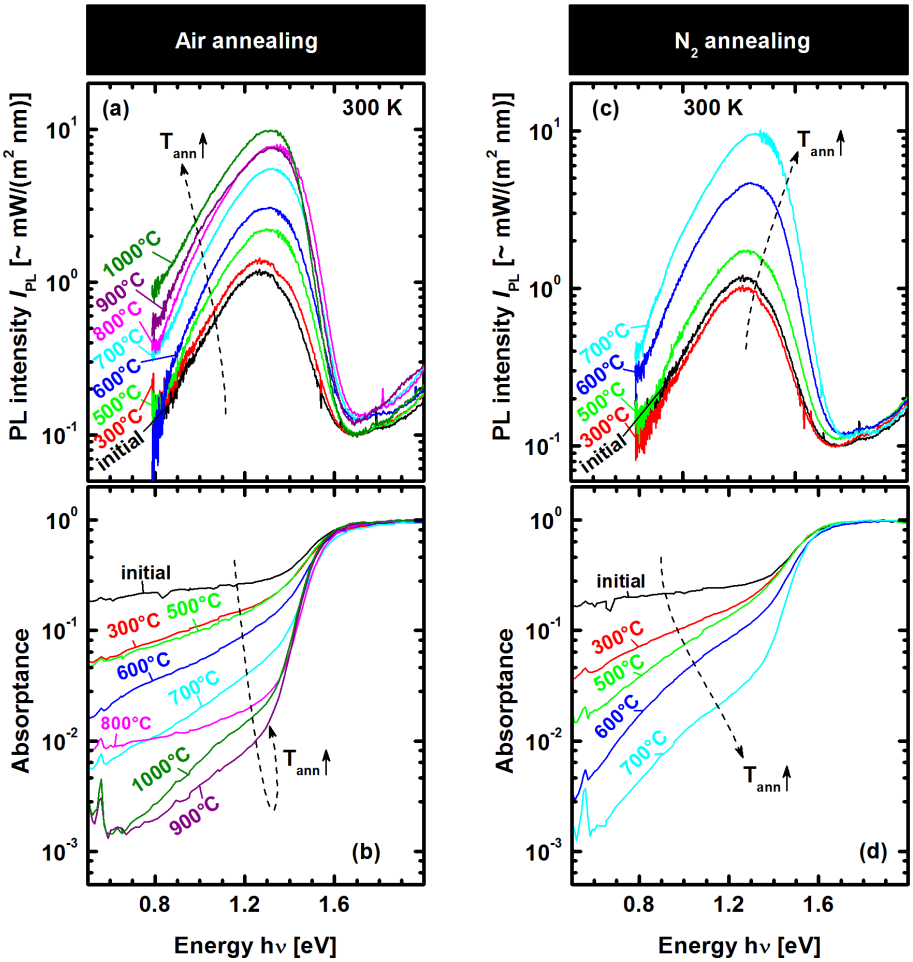

Figure 4.8 – *PL and PDS spectra of the nanoparticles of the annealing series in air (a, b) and nitrogen atmosphere (c, d) up to annealing temperatures of 1000 °C and 700 °C, respectively. The measurements are performed at room temperature and the absorptance as well as PL spectra are presented on a logarithmic scale.*

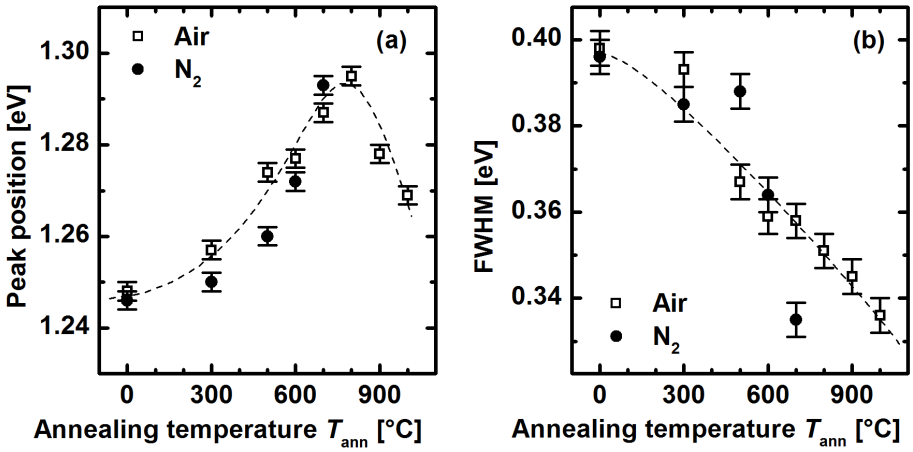

Figure 4.9 *– Peak position (a) and Full Width at Half Maximum (FWHM) (b) of the PL emission in dependence of the annealing temperature. The samples of the annealing series in nitrogen atmosphere (circle) up to an annealing temperature of 700 °C and all samples of the annealing series in air (open square) are regarded. The dashed lines are given as a giude to the eye.*

The onset of the PL at about 1.6 eV is in good agreement to the band edge determined by PDS. The PDS signal shows significant sub gap absorption, extending to low energies. By annealing stepwise in nitrogen as well as in air atmosphere, the sub gap absorption is reduced continuously and the PL intensity increases by about one order of magnitude. The slope of the PDS signal below 1.3 eV increases continuously with increasing annealing temperature for both annealing series. Merely the slope of the sample that is annealed at 800 °C in air is comparable to the slope of the untreated sample.
Up to an annealing temperature of 300 °C, the PL intensities are similar for the respective series. The PL signals of the samples that are annealed in nitrogen atmosphere at 500 °C, 600 °C, and 700 °C show significantly stronger PL compared to the corresponding PL signals of the annealing series in air. There are also differences in the curve shape of the PDS signals. Independent from the annealing atmosphere, the sub gap absorption decreases continuously. Up to an annealing temperature of 900 °C, the sub gap absorption of the samples that are annealed in air atmosphere exhibits a power law behaviour. Merely the annealing process at 1000 °C results in a bent shape between 0.6 eV and 1.3 eV. In contrast to that, all PDS signals of samples annealed in nitrogen atmosphere show a bent curvature in this region.

In figures 4.9 (a) and (b), the positions of the maximum and the Full Width at Half Maximum (FWHM) of the PL emission are plotted against the annealing temperature. With increasing annealing temperature up to 800 °C, the PL peak shifts from

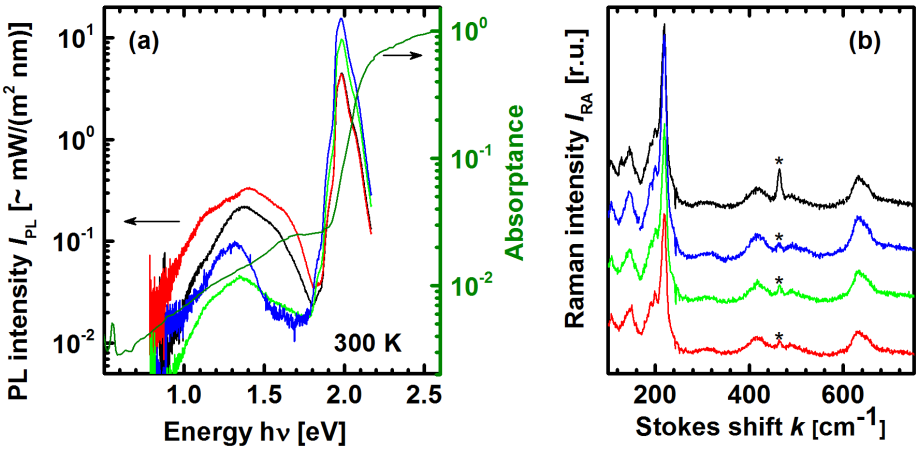

Figure 4.10 *– PL (a) and Raman (b) measurements at room temperature of four different sample spots after annealing at 800 °C in nitrogen atmosphere. The measurements are performed with an excitation laser power of 2.5 Wcm^{-2} to avoid a modification of the nanoparticles during the measurement. In (a) the absorptance is given (dark green line). The asterisks indicate Raman modes of the crystallized quartz substrate.*

about 1.25 eV to nearly 1.3 eV. After annealing at 900 °C and 1000 °C, the PL peak shifts back to lower energies at about 1.27 eV. The FWHM continuously decreases from about 0.4 eV to less than 0.34 eV with increasing annealing temperature.

4.3.3 PL and PDS after phase transition towards cuprite

There is no indication for a phase transition towards cuprite for the samples that are annealed in air up to an annealing temperature of 1000 °C. After annealing at 800 °C in nitrogen atmosphere, the presence of cuprite is confirmed by Raman and XRD measurements. There is no indication for a remaining tenorite phase. Before phase transition, no significant local differences are observed in Raman and PL spectra. Figure 4.10 illustrates four Raman spectra taken from different sample spots. In order to avoid a modification by the laser irradiation, which was observed for an excitation power of 25 Wcm^{-2}, the measurements were performed with a low excitation power of about 2.5 Wcm^{-2}. All four spectra exhibit very similar Raman signatures and there is no indication for a remaining tenorite phase. However, the PL signals reveal strong local differences (c.f. figure 4.10 (a)). All spectra are dominated by a pronounced emission at about 2 eV, which exhibits a fine structure. Its emission intensity varies by almost one order of magnitude. Between 1 eV and 1.6 eV, a weakly pronounced emission is observed. At least, four bands located

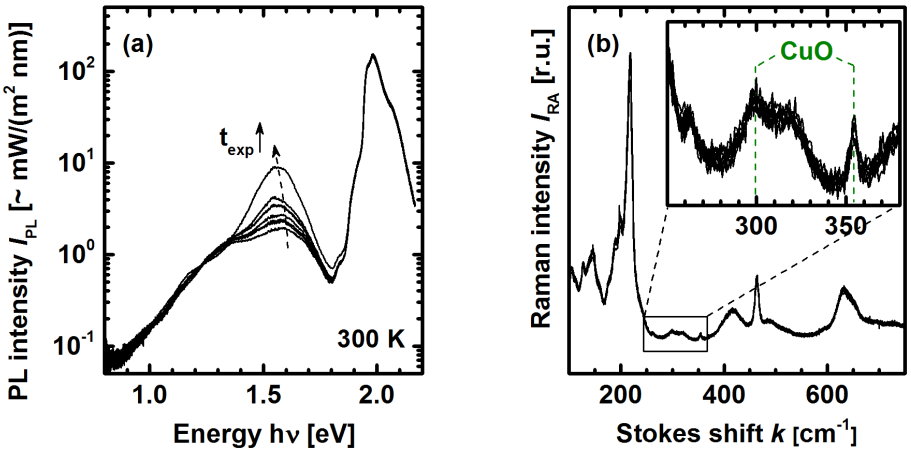

Figure 4.11 – *Series of six PL (a) and Raman (b) measurements at 300 K of the nanoparticles that are annealed at 800 °C in nitrogen atmosphere. One spot after different time of exposure to the laser beam with a excitation laser power of 2.5 Wcm^{-2} is investigated. It is to note, that all the six Raman spectra are depicted, but hardly any difference is observed. The inlet in (b) gives a magnification of the region around 300 cm^{-1}. The main Raman mode of the tenorite phase at about 298 cm^{-1} is indicated by the green line in the inset.*

at about 1.1 eV, 1.3 eV, 1.4 eV, and 1.6 eV are detected. Although the four PL spectra are taken from the same sample, strong differences are observed below 1.6 eV. The intensities of these four bands vary with the sample spot. Figure 4.10 (a) also illustrates the absorptance of the sample after annealing at 800 °C in nitrogen atmosphere (dark green line). The absorbtance increases by about one order of magnitude between 0.5 eV and 2.1 eV with a weakly pronounced absorption band at about 1.6 eV. Between 2.1 eV and 2.2 eV, the range of the optical band gap of cuprite [41, 42], the absorptance increases strongly by almost two orders of magnitude and saturates above 2.5 eV.

Several experiments show, that the properties of the nanoparticles after the phase transition change during the measurements, when the sample is irradiated with a laser excitation power of 2.5 Wcm^{-2}. In order to investigate this influence, Raman and PL are measured on the same spot for various treatment time. Figure 4.11 (a) shows the evolution of the PL spectra. For the first five spectra, the measurement is repeated every 30 minutes. The last one after 12 hours of irradiation. There are no further changes observed after further irradiation. It is clearly visible, that the intensity of the peak at about 1.55 eV increases with increasing irradiation time. Figure 4.11 (b) shows the corresponding Raman spectra. The Raman spectra do not change with prolonged laser irradiation. Between 250 cm^{-1} and 350 cm^{-1} the

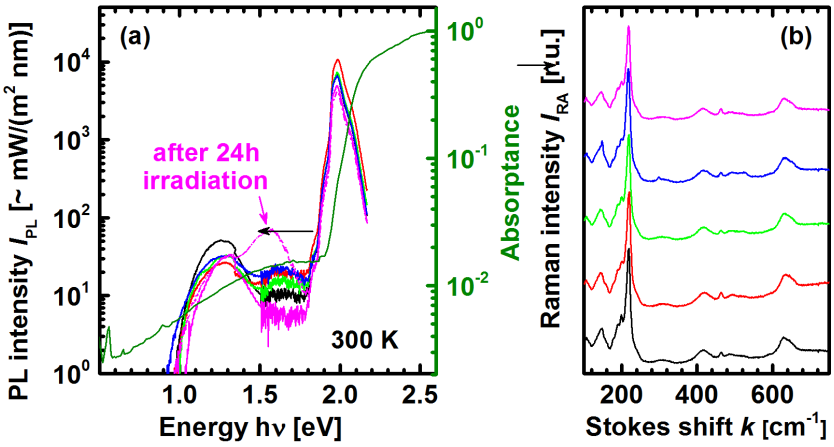

Figure 4.12 *– PL (a) and Raman (b) measurements at 300 K of five different sample spots after annealing at 1000 °C in nitrogen atmosphere. In (a) the absorptance is also given (green line). One spot is measured a second time after exposition to a laser excitation power of 25 Wcm^{-2} for 24 hours (magenta dashed-dotted line). The asterisks indicate Raman modes of the crystallized quartz substrate.*

Raman mode at about 298 cm^{-1} is detected, which is characteristic for the tenorite phase.

4.4 Annealing at 1000 °C in nitrogen atmosphere

After annealing at 1000 °C in nitrogen atmosphere, the Raman, PL, and PDS spectra are similar to those after annealing at 800 °C. Again several sample spots are investigated in order to analyze the homogeneity of the sample. The Raman spectra do not show significant differences (cf. figure 4.12 (b)). All spectra exhibit the characteristic cuprite Raman modes, and in general, there is no indication for the presence of the tenorite phase. Solely one sample (blue line), exhibits a weakly pronounced peak at about 300 cm^{-1}, which can be attributed to the tenorite phase. Figure 4.12 (a) depicts the corresponding emission spectra. Compared to the spectra detected after annealing at 800 °C, the variations of the emission bands are less pronounced. The intensity of the dominant emission at about 2 eV is similar for all spots and at least two orders of magnitute higher compared to the previous annealing step at 800 °C. In the low energy region, the emission at about 1.3 eV is dominant and the emission at about 1.55 eV is unincisive. Only slight differences are observed between the different spots below 1.6 eV. Again, an emission peak at 1.6 eV occurs after 24

hours of irradiation with a comparable low laser excitation power of $25\,\mathrm{Wcm^{-2}}$ (cf. figure 4.12, magenta dashed-dotted line).

4.5 Discussion - modification of copper oxide nanoparticles

In the previous sections Raman, PL, PDS, XRD, and TEM results of copper oxide nanoparticles are presented. Two annealing series of initially tenorite nanoparticles in air as well as in nitrogen atmosphere are analyzed. In the following, the results are discussed with respect to the literature. The discussion is divided into several parts. Firstly, the structural properties, which are deduced from Raman, XRD, and TEM measurements, are discussed. Afterwards, the changes of the opto-electronic properties are interpreted. The analysis of the opto-electronic properties of the tenorite and cuprite nanoparticles are presented separately. At the end of the discussion the main statements are briefly summarized.

4.5.1 Structural modification

Within the limits of the TEM measurements, the as-prepared commercially available tenorite nanoparticles seem to consist of a highly crystalline tenorite phase. According to the TEM images, nanoparticles with a diameter of about 30 nm and few nanoparticles with diameters above 100 nm are found (cf. figure 4.4), which is in good agreement with the diameter found by analyzing the line profile of the XRD reflexes yielding a nanoparticle diameter of 22 nm in the as-prepared state. Raman spectra of the as-prepared nanoparticles show the typical tenorite signature (cf. figure 4.5). According to Raman and XRD results, the nanoparticles remain in the tenorite phase when annealed up to 1000 °C in air. Contrasting, when annealing in nitrogen atmosphere, the nanoparticles are transformed into the cuprite phase for annealing temperatures of 800 °C and 1000 °C (cf. figures 4.5 and 4.7). Considering the stability diagram of the Cu-Cu_2O-CuO system (cf. figure 3.1), this can be explained by the significantly lower oxygen partial pressure when annealing in nitrogen atmosphere as compared to annealing in air. According to Raman and XRD measurements, the vast majority of the nanoparticles is present in the cuprite phase after annealing at 800 °C or 1000 °C in nitrogen atmosphere. According to the stability diagram of the copper oxide system (cf. figure 3.1), this implies an oxygen partial pressure of the order of 10^{-1} hPa when annealing in nitrogen atmosphere. In few Raman spectra, a weakly pronounced peak is detected at about 300 cm^{-1}, which can be ascribed to the tenorite phase (cf. figure 4.11). So far, it cannot be decided if there is a remaining tenorite phase after annealing at 800 °C and 1000 °C, or if the cuprite is oxidized to tenorite when being exposed to air. Besides, the laser irradiation during the Raman and PL measurements could induce the phase transition. Furthermore, based on the experience obtained in the course of this thesis, the Raman cross section of the cuprite phase is significantly higher compared to tenorite when detecting the Raman signal with an excitation laser wavelength of 532 nm. In conclusion, it cannot be ruled out, that there is still some tenorite phase left after

annealing at 800 °C or 1000 °C in nitrogen atmosphere.
The volume fraction of the respective copper oxide phases can be roughly estimated by a simple approach evaluating the count rates of characteristic Raman modes. For this purpose, the integrated count rates of the cuprite Raman mode at about 220 cm^{-1} and the tenorite Raman mode at 300 cm^{-1} that are observed after annealing at 800 °C in nitrogen atmosphere are investigated (cf. figure 4.11 (b)). These count rates are compared to the corresponding count rates derived from Raman spectra of as-prepared nanoparticles and after annealing at 1000 °C in nitrogen atmosphere. It is assumed that the as-prepared nanoparticles and the nanoparticles annealed at 1000 °C are solely present in the tenorite and cuprite phase, respectively. Hence, the count rates of these samples correspond to volume fractions of 100% for the respective phases.
The cuprite Raman mode at 220 cm^{-1} exhibits a asymmetric shape due to neighbouring Raman modes at lower wavenumbers. To avoid the influence of these neighbouring modes, the count rates are estimated as follows (cf. figure 4.13 (a)). A line parallel to the y-axis is fit to the peak at 220 cm^{-1} so that the top part of the peak is divided into two halves symmetrically. after correcting the background by subtraction a horizontal line, which is fit at the minimum next to the peak at the high wavenumber side, only the intensity of the high wavenumber half of the peak is integrated (striped area) and divided by the recording time. For the tenorite Raman mode, a neighbouring peak is observed at higher wavenumbers after annealing at 800 °C. Similar to the described procedure, the tenorite peak is also divided into two halves and only the low wavenumber half is evaluated accordingly.
As illustrated in figure 4.13 (b), the calibration line for the volume fraction of the tenorite phase (black line) mode is assumed to decrease linearly with decreasing tenorite volume fraction, whereas the cuprite count rate (red line) increases with increasing cuprite volume fraction. The count rates for the cuprite and tenorite Raman mode of the nanoparticles annealed at 800 °C are presented as green and blue horizontal bars, respectively. Since the Raman spectrum of the nanoparticles annealed at 800 °C is not measured at the same day as the spectra used for calibration, the adjustment of the Raman setup is probably slightly different leading to an error of the estimated count rates, which accounted for a relative error of about 10%. The widths of the blue and green bars are chosen to represent this error. The corresponding volume fraction can then be estimated by the intersection between the derived count rates and the red and black calibration line (indicated by dark and light grey striped areas). The count rate of the tenorite Raman mode implies a tenorite volume fraction of the order of 5%, whereas the cuprite Raman mode yields a cuprite volume fraction of only 80%.
This difference can probably be explained by the simplicity of the approach ignoring several problems which could arise from the arrangement of the nanoparticles. If for example tenorite nanoparticles are arranged to a layer with a thickness of about 1 µm, the laser beam is already absorbed in the first 500 nm of the layer. Hence,

the remaining tenorite nanoparticles do not contribute to the Raman signal, and are therefore not considered in the Raman count rates.[4] Consequently, the tenorite volume fraction is underestimated. The same conclusion applies for thick cuprite nanoparticle arrangements. Moreover, a similar argumentation is valid if cuprite nanoparticles are covered by tenorite nanoparticles and vice versa, leading to underestimating of the volume fraction of the buried compound.
Nevertheless, using this simple model, a first estimation of the respective copper oxide volume fractions is achieved, revealing a tenorite volume fraction of less than 20% in the probed spot after annealing at 800 °C. Note, that the tenorite Raman modes are not observed in every Raman spectrum after annealing at 800 °C. Hence, the respective volume fractions of the tenorite and cuprite phase probably vary with the sample spot indicating local inhomogeneities in terms of phase composition.
Under appropriate conditions, Raman signals offer information about defects and stress in the material. Defects and stress may lead to a distortion of the lattice and therefore to a variation of the binding properties, which can lead to a shift of the Raman frequencies and a variation of the line shape of the Raman signal. Here, the strongest tenorite Raman mode at about 298 cm^{-1} is analyzed in more detail. The samples of both modification series, which do not show cuprite Raman modes, are evaluated. This means, that the Raman spectra of the annealing series in nitrogen atmosphere up to an annealing temperature of 700 °C and all Raman spectra of the annealing series in air are regarded. Up to an annealing temperature of about 400 °C the FWHM remains nearly constant at 14 cm^{-1} to 15 cm^{-1}. Further annealing up to 800 °C leads to a continuous reduction of the FWHM to 8 cm^{-1} and remains constant up to an annealing temperature of 1000 °C (cf. figure 4.6 (a)). This width is comparable to the best value of about 6 cm^{-1} that is reported in the literature for a tenorite single crystal, which indicates the high quality of the nanoparticles obtained by proper annealing [82].
The narrowing of the peak is accompanied by a shift of the Raman mode from about 297 cm^{-1} to 299 cm^{-1} with increasing annealing temperature (cf. figure 4.6 (b)). The shift of the peak and the reduction of the FWHM indicate the reduction of structural defects and the release of stress. Note, the FWHM and the peak position change for both annealing series, likewisely. So, the surrounding annealing atmosphere does not influence the structural modification of the tenorite nanoparticles before the phase transition.
Besides, the detected XRD reflexes of the copper oxide nanoparticles give further information about the structure of the copper oxide properties. After instrumental correction, the signal obtained from the as-prepared sample shows a crystallite size of about 22 nm ± 3 nm and a microstrain value $\Delta d/d_0 = 0.22 \pm 0.03$, where d is the undistorted lattice spacing, as derived from the double Voigt approach (e.g.

[4] For this estimation, the absorption coefficient for tenorite at the laser wavelength of 532 nm is assumed to be about $4 \cdot 10^4\,\mathrm{cm}^{-1}$, cf. Meyer et al. [28].

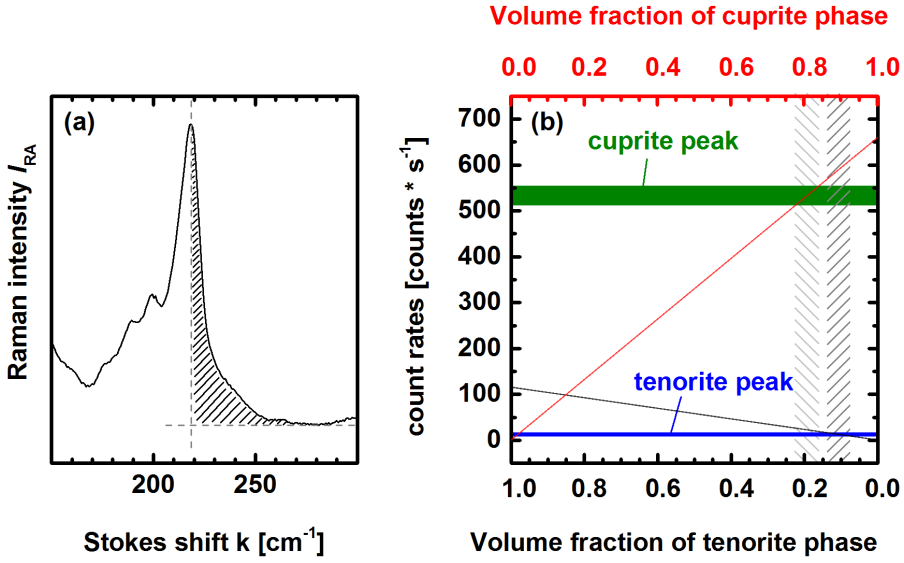

Figure 4.13 – *(a) illustration of the integrated intensity (striped area) of the cuprite Raman mode at 220 cm^{-1}. (b) Count rates for the cuprite (220 cm^{-1}) and tenorite (300 cm^{-1}) Raman modes of the nanoparticles annealed at 800 °C in nitrogen atmosphere (cf. figure 4.11 (b)) are presented as green and blue horizontal bars, respectively. The black and red line represent calibration lines for the volume fraction the tenorite (black line) and cuprite (red line) phases.*

[139]) using the software TOPAS[5]. For this evaluation, Lorentzian broadening is assigned to the crystallite size, whereas Gaussian broadening is ascribed to microstrain. After annealing at 700 °C in nitrogen atmosphere (air), the signal broadening is significantly limited by the experimental setup, leading to values with large error bars of 127 nm ± 25 nm (81 nm ± 15 nm) for the crystallite size and 0.04 ± 0.02 (0.09 ± 0.01) for the microstrain. These structural changes might be caused by partial sintering of the particles, as well as, by the annealing of structural defects like e.g. stacking faults which would be consistent with the conclusion derived from the Raman data. After annealing at 800 °C and 1000 °C in nitrogen atmosphere, the nanoparticles are transformed into the cuprite phase and exhibit diameters of 38 nm ± 3 nm and 62 nm ± 10 nm and microstrain values of 0.15 ± 0.01 and 0.22 ± 0.01, respectively. For the nanoparticles that are annealed at 1000 °C in air, a diameter of 295 nm ± 46 nm and a microstrain value of 0.08 ± 0.01 is deduced from the XRD

[5]Bruker AXS TOPAS V4: General profile and structure analysis software for powder diffraction data (2008)

reflexes. Hence, the nanoparticles that are annealed in air grow continuously with increasing annealing temperature. In contrast, the nanoparticles annealed in nitrogen atmosphere firstly grow with increasing annealing temperature, shrink after the phase transition into cuprite before they grow again for even higher temperature.

In order to probe if the nanoparticles sinter at elevated temperatures, the nanoparticles that are annealed at 1000 °C in air and nitrogen atmosphere are investigated by TEM measurements. Figure 4.14 (a) and (b) illustrate representative bright and dark field images of the nanoparticles that are annealed at 1000 °C in air. The bright field image (figure 4.14 (a)) shows a nanoparticle with dimensions of about 100 nm × 200 nm. Figure 4.14 (b) shows the corresponding dark field image and as an inset the diffraction pattern which reveals a crystalline structure. The figures 4.14 (c) and (d) depict a bright field image and a magnified bright field image of the nanoparticles after annealing at 1000 °C in nitrogen atmosphere. The nanoparticles are highly crystalline and seem to be composed of several smaller nanoparticles. In conclusion, the nanoparticles are sintered after anealing at 1000 °C and form larger aggregates. Hence, the TEM measurements confirm the increase of the nanoparticle size, which is derived from the XRD reflexes. However, in order to deduce a nanoparticle size of 100 nm in XRD, the coherence of the lattice planes should be on the same scale. This indicates, that the sintered nanoparticles do not exhibit randomly distributed crystallographic orientations, but align into coherent domains with the same orientation.
For the application as an absorber material in a thin film solar cell, the sintering of the nanoparticles to larger aggregates is a critical issue that has to be adressed in future work. It is important to analyze at what temperature the sintering takes place. Furthermore, it has to be probed, if the sintering can be suppressed by shorter annealing cycles, which can be achieved by rapid thermal annealing (RTA), or if comparable high quality copper oxide nanoparticles can be realized at lower annealing temperatures; e.g. by longer annealing cycles.

4.5.2 Opto-electronic properties of tenorite nanoparticles

Subsequently, the opto-electronic properties of the nanoparticles that are purely present in the tenorite phase are discussed. Thus, all samples of the air annealing series are analyzed, whereas only the samples that are annealed in nitrogen atmosphere are considered up to an annealing temperature of 700 °C.
For as-prepared nanoparticles, the PL spectrum at room temperature exhibits a peak at about 1.28 eV (cf. figures 4.8 (a) and (c)). The PDS signal slightly increases between 0.5 eV and 1.4 eV and then increases further by a factor of three in the region between 1.4 eV and 1.6 eV before it saturates at higher energies (cf. figures 4.8 (b) and (d)). The value just below the saturation at about 1.6 eV corresponds well to the optical band gap reported in the literature for tenorite bulk material [89, 90, 91]. The onset of the PL at about 1.6 eV is in good agreement

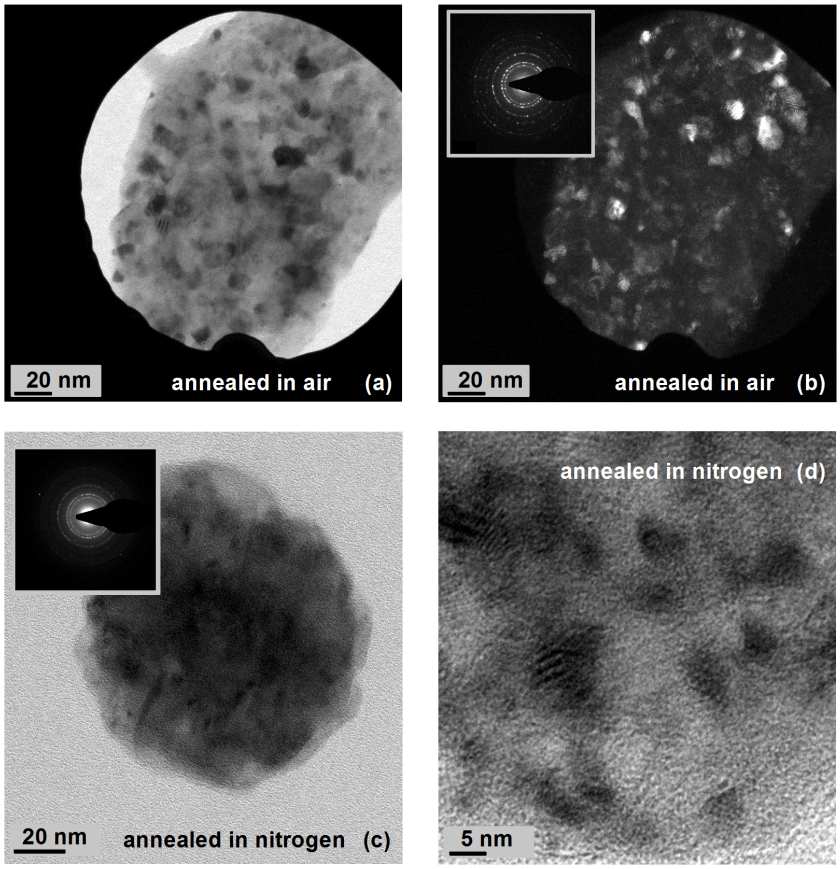

Figure 4.14 *– Bright field (a) and dark field image (b) of the nanoparticles after annealing at 1000°C in air. (c) and (d) show a bright field image and a magnified bright field image of the nanoparticles after annealing at 1000°C in nitrogen atmosphere. The insets in (b) and (c) show the corresponding diffraction patterns.*

with the band gap determined by PDS and is consequently interpreted as band edge emission. Tenorite is usually assumed to be a non-luminescent system [28]. Recently, several groups report luminescence of tenorite nanostructures and thin films in the region between 1 eV and 4 eV [97, 96, 95]. However, X-ray photoelectron spectra and XRD measurements reveal that these samples are not solely present in the tenorite phase but also contain cuprite, which could be responsible for the detected emission bands. Additionally, possible effects arising from substrate emission are not considered there. Here, the data provide very strong evidence for the observation of tenorite band edge emission. Therefore, the presented results show, that the as-prepared tenorite nanoparticles exhibit superior electronic properties in comparison with bulk material. Particularly, surface states, which could be expected to be problematic for nanoparticles with a high surface to volume ratio, do not fully deteriorate the opto-electronic properties significantly. Clearly, the PDS spectrum shows significant sub gap absorption extending to low energies indicating a high defect concentration in the initial state of the nanoparticles. Annealing stepwise in air and nitrogen atmosphere up to 1000 °C and 700 °C, respectively, reduces the sub gap absorption continuously and concomitantly the PL intensity increases by about one order of magnitude (cf. figures 4.8 (b) and (d)). The decreasing sub gap absorption with increasing annealing temperature confirms that the defect concentration is reduced. This leads to the conclusion, that the increasing PL signal is due to the reduction of non-radiative recombination. Moreover, the position of the PL peak and its width depends on the annealing temperature, which is discussed in the following section.

4.5.2.1 Shift of the emission peak

The maximum of the emission increases from about 1.25 eV to 1.3 eV with increasing annealing temperature up to 700 °C and 800 °C in air and nitrogen atmosphere, respectively. After annealing at 900 °C and 1000 °C in air, the maximum shifts back to 1.27 eV. Concomitantly, the full width at half maximum decreases from about 0.4 eV to 0.34 eV (cf. figure 4.9 (a)).

The shift of the emission peak could originate from a higher radiative recombination rate. When the defect concentration is reduced, the population of charge carriers in the conduction and valence band increases. Therefore, states that are located at energetically higher positions in the respective bands are occupied. This effect could lead to higher recombination energies and thus to a blue-shift shift of the emission peak. If the variation of the population in the corresponding band explained the shift of the emission, it should also be visible when varying the laser excitation power. However, the position of the emission peak is not affected by the excitation laser power. Consequently, this effect is possibly not responsible for the blue-shift of the emission. Alternatively, the shift of the emission maximum could be explained by a modification of the slopes of the density of states slightly above and below the valence and conduction band, respectively. Hence, the joint density

of states, which governs the emission and absorption characteristics, is altered. As discussed in section 2.2.2, there are a variety of reasons for the formation of band-tail states. The copper oxide compounds neither occur in an amorphous structure, nor in miscible phases of the form Cu_xO. Apart from slight deviations from the perfect stoichiometry due to copper and oxygen vacancies, copper oxides exists merely in the crystalline compositions CuO, Cu_2O, and Cu_4O_3. Consequently, the band-tail states probably arise from fluctuations of the optical band gap due to stress, changes of the interatomic distances, or microscopic electric fields that is related to electron-phonon coupling [91]. Besides, defects, which induce electronic states close to the band edges could be responsible the band-tail states. A strong defect absorption is observed just below the optical band gap, which is detected in all PDS spectra for both annealing series, which is continuously reduced with increasing annealing temperature. According to theoretical calculations, copper vacancies (V_{Cu}^{ξ}) exhibits the lowest formation enthalpy of all point defects and are therefore expected to be the dominant point defect in tenorite [140]. Experimentally, tenorite is found to exhibit p-type conductivity [28, 92]. In good agreement with theoretical calculations, the p-type behaviour is explained by copper vacancies that form acceptor levels at about 0.1 eV above the valence band [28, 93].
Hence, the absorption slightly below the band gap is partially ascribed to arise from acceptor conduction band transitions. Since the width of the tail is broader than 0.1 eV further effects such as stress or electron-phonon coupling probably contribute to the tail. The shift of the PL maximum accompanied by the narrowing of the line shape is explained by the annealing of defects leading to a narrower distribution of electronic states close to the band edges and probably steeper band-tails.

4.5.2.2 Defect structure in the tenorite nanoparticles

Knowing the electronic structure of defects is essential to understand the opto-electronic properties of a semiconductor. Because of that, the changes of the opto-electronic properties are evaluated with regard to information about the defect structure of the tenorite nanoparticles.
By introducing a defect into a crystal, a structural relaxation can take place, which is reflected in the change of the atomic distances and binding angles in the vicinity of the defect. Through this, also the electronic structure is altered by inducing a defect level. Theoretical calculations predict several point defects such as oxygen (V_O^{ξ}) and copper (V_{Cu}^{ξ}) vacancies, oxygen (O_{Cu}^{ξ}) and copper (Cu_O^{ξ}) antisites, as well as oxygen (O_i^{ξ}) and copper (Cu_i^{ξ}) interstitials to be present in the tenorite phase [140]. Here, the index ξ stands for the charge state of the defect. Wu et al. calculate the formation enthalpies of the different point defects [140]. Depending on the Fermi-level, different charge states are found to be most stable. For a Fermi-level close to the valence band maximum the stable charge states for each point defect are Cu_O^{2+}, Cu_i^0, V_O^0, O_i^0, O_i^{2-}, and V_{Cu}^{2-}. On the other hand, Cu_O^0, Cu_i^0, V_O^0, O_i^{2-}, O_{Cu}^{2-}, and V_{Cu}^{2-} are the most stable charge states when the Fermi-

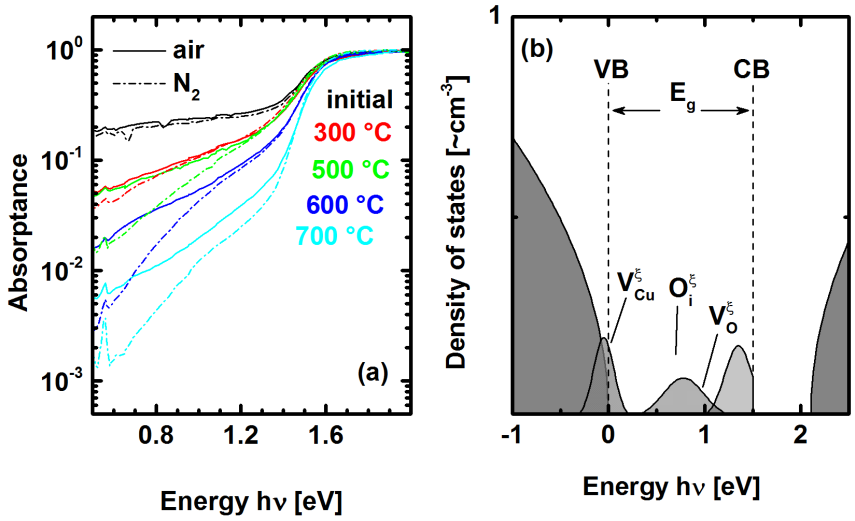

Figure 4.15 – *(a) PDS spectra of tenorite nanoparticles that are annealed in air (solid line) and nitrogen atmosphere (dashed-dotted line). (b) a schematic model of the density of states of tenorite involving the contribution of copper oxide vacancies (V_{Cu}^{ξ}) and oxygen interstitials (O_i^{ξ}). Moreover, the presence of defect states due to oxygen vacancies (V_O^{ξ}) is indicated.*

level is close to the conduction band minimum. The doubly charged copper vacancy (V_{Cu}^{2-}) always exhibits the lowest formation enthalpie of all point defects and is consequently expected to be the dominant point defect. According to Peng et al. and Wu et al., copper vacancies (V_{Cu}^{ξ}) and oxygen vacancies (V_O^{ξ}) form shallow defect level slightly above the valence band and deep defect states in the middle of the band gap, respectively [140, 93]. So far, no experimental results are published, which specify the energetical positions of the point defects.

As previously discussed, the absorption in the near IR is reduced significantly with increasing annealing temperature, which is ascribed to the annealing of defects. According to the theoretical considerations, probably copper and oxygen vacancies are the predominant point defect. The changes of the emission and absorption characteristics are similar for both annealing series. However, also significant differences are observed between the samples that are annealed in air and nitrogen atmosphere, which bares information about the defect structure.

Up to an annealing temperature of 300 °C, the PL intensities are similar for both series. However, after annealing at 500 °C, 600 °C, and 700 °C, the emission intensity of the nanoparticle that are annealed in nitrogen atmosphere is significantly higher indicating a lower defect concentration. This interpretation is also confirmed by the PDS spectra. The sub gap absorption of the nanoparticles that are annealed up to

900 °C in air exhibits a power law behaviour, whereas a bent curvature is found for the annealing series in nitrogen atmosphere. Figure 4.15 (a) depicts the PDS spectra of the tenorite nanoparticles that are annealed in air (solid line) and nitrogen atmosphere (dashed-dotted line). Comparing the spectra for the respective annealing temperatures, no significant differences are observed for the as-prepared nanoparticles (black line) and after annealing at 300 °C (red lines). However, after annealing at 500 °C (light green lines), 600 °C (blue lines), and 700 °C (cyan lines) the sub gap absorption of the nanoparticles annealed in nitrogen atmosphere is lower. Especially, the absorption below 1.2 eV is reduced significantly. This indicates a lower defect concentration, which leads to less non-radiative recombination and explains the higher PL intensities of nanoparticles annealed in nitrogen atmosphere. The origin for this is very likely the different oxygen partial pressures of the annealing atmosphere, which holds information about the related defects. At elevated temperatures, oxygen is expected to escape from the sample, which finally ends up in the phase transition from tenorite to cuprite. The release of oxygen depends on the temperature and on the oxygen partial pressure. Annealing in nitrogen atmosphere, the oxygen partial pressure is considerably lower than in air. Hence, the oxygen is expected to escape from the nanoparticles at lower temperatures. Therefore, the dynamics of the oxygen atoms, and thus the changes of the oxygen related point defects, are believed to be responsible for the differences between the two annealing series. There are three oxygen related point defects in tenorite, namely vacancies (V_O^{ξ}), antisites (O_{Cu}^{ξ}), and interstitials (O_i^{ξ}). The oxygen atom that forms a vacancy either has to occupy another position in the crystal lattice, or has to escape from the crystal. In the former case, the oxygen can occupy the position of a copper vacancy forming an oxygen antisite (O_{Cu}^{ξ}). Alternatively, the oxygen atom can be located at an interstitial position. However, there is no reason, why these redistribution processes should be affected by the annealing atmosphere. A lower oxygen partial pressure is beneficial if the oxygen vacancy is formed by the escape of an oxygen atom from the crystal. But, this should lead to a higher concentration of oxygen vacancies for the nanoparticles that are annealed in nitrogen atmosphere, which contradicts the stronger PL intensity as well as the lower sub gap absorption. Likewise, a possible reduction of the concentration of the oxygen vacancies due to the incoporation of oxygen atoms from the air atmosphere is not compatible with the variations of the PDS and PL results. In conclusion, the oxygen vacancy point defect cannot be the origin for the defect absorption below 1.2 eV. The lower defect concentration for the nanoparticles that are annealed in nitrogen atmosphere is possible related to the release of oxygen from the nanoparticles, which is facilitated by the lower oxygen partial pressure. Instead of oxygen vacancies (V_O^{ξ}), oxygen antisites (O_{Cu}^{ξ}) or oxygen interstitials (O_i^{ξ}) could be the reason for the differences. The concentration of these two point defects can be reduced by the release of oxygen. However, if an antisite oxygen atom (O_{Cu}^{ξ}) escapes from the nanoparticle, it will leave a copper vacancy (V_{Cu}^{ξ}), which give rise to electronic states slightly above the

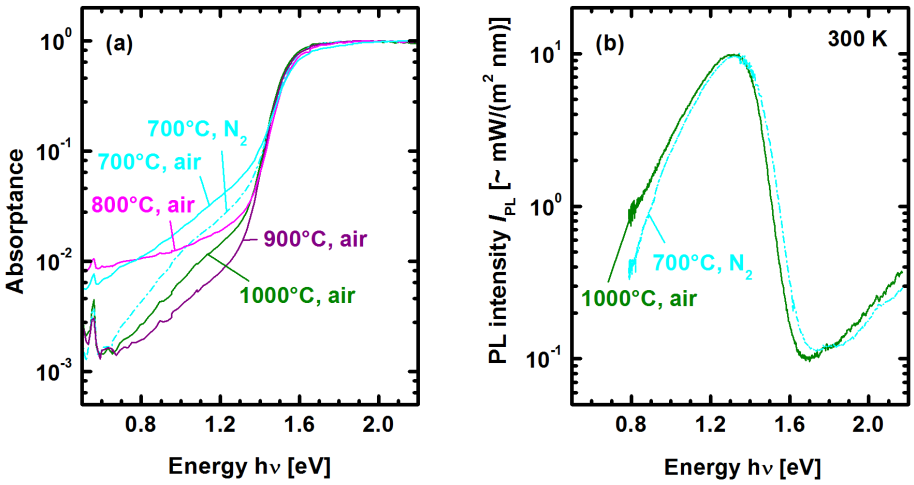

Figure 4.16 *– (a) PDS spectra of tenorite nanoparticles that are annealed in air (cyan, magenta, purple, and dark green solid line) and nitrogen atmosphere (cyan dashed-dotted line). (b) PL spectra at 300 K of the tenorite nanoparticles annealed at 1000 °C (dark green line) and 700 °C (cyan dashed-dotted line) in air and nitrogen atmosphere, respectively.*

valence band [28, 93, 140, 141]. Since the absorption just below the optical band gap does not increase, the decrease of the sub gap absorption cannot be associated with a decreasing concentration of oxygen antisites (O_{Cu}^{ξ}). Therefore, the sub gap absorption below 1.2 eV is partly ascribed to oxygen interstitials, which induce deep defect levels in the optical band gap. Note, that theoretical considerations show that other defects such as oxygen vacancies (V_O^{ξ}) induce defect levels, which are proposed to be located in the middle of the band gap [141].
As a result, figure 4.15 (b) illustrates a simple model of the density of states of tenorite material involving the contribution of copper vacancies (V_{Cu}^{ξ}) and oxygen interstitials (O_i^{ξ}) as proposed in the previous sections. According to theoretical considerations, defect states in the middle of the band gap that arise from copper vacancies are included (V_O^{ξ}) [140, 141]. Note, that the exact energetical postions of the defect states has not been investigated experimentally in the literature, and is thus unknown so far.

Interestingly, the shape of the sub gap absorption of the nanoparticles that are annealed in air do not evolve continuously for elevated annealing temperatures. Figure 4.16 (a) depicts the absorptance spectra of the nanoparticles annealed at 700 °C (cyan line), 800 °C (magenta line), 900 °C (purple line), and 1000 °C (dark green line) in air as well as 700 °C (cyan dashed-dotted line) in nitrogen atmosphere. In contrast to the general trend for the air annealing series, a flatter increase of the

sub gap absorption of the sample that is annealed at 800 °C is observed. The reason for this behaviour is not clear so far. Notably, after annealing at 900 °C, the increase of the sub gap absorption is steeper again. Moreover, after annealing at 1000 °C, the sub gap absorption does not scale according to a power law, but exhibits a bent curvature similar to the nanoparticles that are annealed in nitrogen atmosphere. Comparing the absorption spectra of the nanoparticles that are annealed at 1000 °C and 700 °C in air and nitrogen atmosphere, respectively, a similar shape is obersved. Also, the emission signals are comparable in terms of peak intensity, width, and position (cf. figure 4.16 (b)). For annealing in air atmosphere, according to the stability diagram of the copper oxide system (cf. figure 3.1), the phase transition is expected at about 1000 °C. Therefore, the change of the curvature after annealing at 1000 °C could be related to the release of oxygen due to the onset of the phase transition from tenorite to cuprite.

4.5.3 Opto-electronic properties of cuprite nanoparticles

Annealing at 800 °C in nitrogen atmosphere, the nanoparticles are transformed in to the cuprite phase, which is clearly visible in the emission and absorption characteristics. Between 1.9 eV and 2.2 eV the absorptance increases by about two orders of magnitude and saturates for higher energies. The value just below the saturation is in good agreement with the pronounced emission at 2 eV and the optical band gap of 2.1 eV for cuprite bulk material [41, 42] (cf. figure 4.10 (a)). Accordingly, the dominant emission band at about 2 eV is ascribed to cuprite band edge emission (cf. figure 4.10 (a)). The fine structure of this peak can be attributed to exciton related transitions, which will be discussed in detail in section 4.5.3.1. Furthermore, an absorption tail extending to lower energies is observed and is attributed to defect absorption from copper and oxygen vacancies [54]. The slight increase of the PDS signal at about 1.4 eV is ascribed to tenorite. Therefore, the PDS method is more sensitive in detecting a remaining tenorite phase than Raman spectroscopy and XRD. In the near IR a weakly pronounced emission is observed, which is composed of at least four bands located at about 1.1 eV, 1.3 eV, 1.4 eV and 1.6 eV (cf. figure 4.10 (a)). In the literature, three emission signals at 1.72 eV, 1.53 eV, and 1.35 eV have been attributed to doubly-charged oxygen, singly-charged oxygen, and copper vacancies, respectively [60, 70, 71, 72, 70]. The exact peak positions and intensities strongly depend on the preparation procedure. Consequently, the emission in the near IR is due to a superposition of tenorite band edge emission of the remaining tenorite phase and well known defect emission in cuprite, arising from copper and oxygen vacancies.
Depending on the sample position, the relative intensities of the four peaks as well as the intensity of the pronounced band edge emission vary significantly. This indicates that the nanoparticles are not modified homogeneously, which is reflected in variations of the defect concentrations and different portions of remaining tenorite

phase. This inhomogeneity is supposedly explained by inhomogeneous heat transfer in the sample during annealing. Besides, the size of the nanoparticles probably affects the phase transition and the generation of defects.
Interestingly, the absorption that is attributed to the tenorite phase saturates, before the absorption increases further due to the absorption of the cuprite phase and finally saturates at higher energies (cf. figure 4.10 (a)). If the two phases were homogeneously mixed, a gradual increase of the absorption below 2 eV would be expected. Therefore, the shape of the PDS signal gives evidence, that the cuprite and tenorite nanoparticles are separated. Assuming that the PDS values in the regions of saturation for the tenorite and cuprite phase is proportional to the covered area of the respective phases, the ratio of these PDS values can be interpreted as the relative volume fraction of the two phases. Again, this simple model ignores effects due to the arrangement of the nanoparticles as discussed in section 4.5.1. This evaluation yields a tenorite volume fraction of about 2.5%, which is in good agreement with the estimation derived from the Raman spectra, which suggested a tenorite volume fraction smaller than 20%. By PDS, a substantially larger spot is probed than by the micro-Raman measurement. Hence, the PDS data provide averaged information, whereas the Raman measurement investigates the nanoparticles more locally. Note, that the tenorite Raman modes are not observed in every Raman spectra of the nanoparticles annealed at 800 °C indicating local differences of the composition. Probably, the sample spot that was investigated by Raman contained a higher tenorite volume fraction than the average of the sample.

After annealing at 1000 °C in nitrogen atmosphere, the absorption spectrum is comparable to the previous annealing step, but no contribution from a remaining tenorite phase is detected (cf. figure 4.12 (a)). In comparison to the nanoparticles annealed at 800 °C, the intensity of the dominant band edge emission at about 2 eV increases by more than two orders of magnitude. This considerable increase of the intensity suggests less non-radiative recombination and therefore a lower defect concentration. In the near IR, only weakly pronounced emission signals are detected, whereof the emission at 1.3 eV is the most strongest. According to the literature, this emission is attributed to the presence of copper vacancies [60]. Hence, copper vacancies are found to be a dominent point defect in cuprite. This interpretation is in good agreement with the fact that cuprite shows usually p-type conductivity, which is explained by copper vacancies forming acceptor levels slightly above the valence band [30, 29]. Investigating several sample spots, hardly any difference are observed in the emission spectra, which indicates very homogeneous properties.

4.5.3.1 PL of cuprite - comparison to literature

The emission spectra of cuprite material are usually dominated by the strongly pronounced defect related emission in the near IR. Mostly, band edge emission of cuprite is not detected at all or only observed at low temperatures, which is

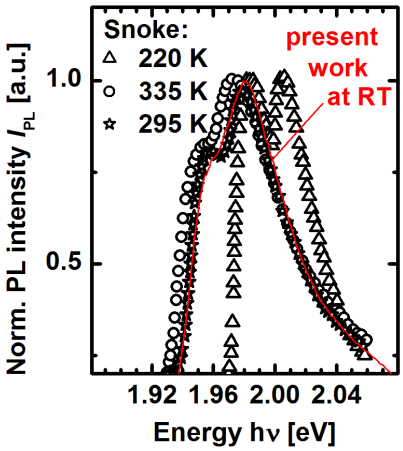

Figure 4.17 – *PL spectra of a natural, high purity cuprite single crystal detected at sample temperatures of 220K (triangle), 295K (star), and 335K (circle) after Snoke et al. [53]. For comparison, a representative PL spectrum of cuprite nanoparticles after annealing at 1000 °C in nitrogen atmosphere (red line) is given.*

ascribed to poor quality material due to a high defect concentration [28, 72]. But, Snoke et al. investigated a natural, high purity cuprite single crystal, which exhibits strong band edge emission in the temperature region between 77 K an 335 K. The dominant emission band at 2 eV shows a characteristic fine structure. Snoke et al. investigated this fine structure and identified two luminescence lines due to phonon assisted recombination of the orthoexciton involving the 13.6 meV (110 cm^{-1}) Γ_{12} phonon [53] (cf. 3.1.1.4). Figure 4.17 illustrates PL spectra of natural, high purity samples of cuprite detected at sample temperatures of 220 K (triangle), 295 K (star), and 335 K (circle) taken from Snoke et al. [53]. For comparison, a representative PL spectrum of cuprite nanoparticles after annealing at 1000 °C in nitrogen atmosphere (red line) is given. Note, that Snoke et al. give no information about the unit of the emission intensity. However, as the spectra cover only a narrow spectral range a direct comparison of these spectra and the data obtained in this work is feasible. Comparing a PL spectrum that is typically detected in the course of this thesis to the literature data a very good agreement to the spectrum taken at 295 K is found. Merely, the minimum between the two emission lines is more pronounced in the literature data. Since the shape and the relative intensities of the two emission signals depend on the kinetic distribution of the excitons and the occupation number of the phonons, respectively, the differences could be explained by a broadening of the kinetic energy distribution.

Consequently, the cuprite nanoparticles that are prepared by the modification of tenorite by oven annealing exhibit excellent opto-electronic properties, which are at least similar to high quality bulk material.

4.5.3.2 Influence of laser irradiation

For the samples that are annealed at 800 °C and 1000 °C in nitrogen atmosphere, the emission of the nanoparticles is found to change under laser irradiation with a low laser excitation power of about 2.5 $\mathrm{Wcm^{-2}}$. Exemplarily, figure 4.11 illustrates the change of the emission spectrum for the nanoparticles annealed at 800 °C. With prolonged laser irradiation, the emission band located at about 1.55 eV increases continuously. According to the literature, this peak can be attributed to transitions involving singly-charged oxygen vacancies [60, 71, 72, 70]. The reason for the increasing intensity is not evident. Possibly, oxygen vacancies are created by laser irradiation. If the defect related emission at 1.6 eV and the excitonic emission at 2 eV arised from the same nanoparticle, an increase of the defect emission would be expected to be accompanied by a reduction of the excitonic emission due to competing transitions. However, the excitonic emission does not change at all. Hence, it is concluded that the occuring emission at 1.6 eV does not originate from the same nanoparticles as the excitonic emission. Therefore, different nanoparticles exhibit different opto-electronic properties; e.g. different defect concentrations. It is believed that high quality cuprite nanoparticles that already give rise to the pronounced emission at 2 eV are not affected by laser irradiation, whereas nanoparticles of poorer properties are modified.

4.5.4 Summary - characterization & modification of copper oxide nanoparticles

The structural and opto-electronic properties of tenorite nanoparticles are significantly improved by oven annealing in nitrogen atmosphere as well as in air. Subsequently, the main statements of the discussion are summarized briefly.

Annealing in air, the nanoparticles remain in the tenorite phase up to an annealing temperature of 1000 °C. Changes of the Raman and XRD patterns confirm an improvement of the structural properties due to the reduction of structural defects and the release of stress. The emission signal at 1.3 eV is attributed to tenorite band edge emission, which is in line with the band gap deduced from the PDS measurement. The emission intensity increases by more than one order of magnitude with increasing annealing temperature accompanied by a continuous decrease of the sub gap absorption, which underlines the annealing of defects and confirms the formation of high quality tenorite material. Similar results are observed for the second annealing series in nitrogen atmosphere up to an annealing temperature of 700 °C. Following the prevailing opinion in the literature, copper and oxygen vacancies are

believed to be dominant point defects in tenorite. Comparing the two annealing series, a significant impact of oxygen interstitials is found, which concentration is preferentially reduced when annealing in nitrogen atmosphere.

After annealing at 800 °C in nitrogen atmosphere, the tenorite nanoparticles are transformed into cuprite. While XRD measurements suggest the nanoparticles to be present solely in the cuprite phase, the PDS measurements and few Raman spectra reveal a remaining tenorite phase. From Raman and PDS measurements the tenorite volume fraction is estimated to be smaller than 20%. The PL spectra are dominated by a strong emission at 2 eV, which correlates well to the band gap derived from the PDS measurement and is consequently attributed to band edge emission. Besides, weakly pronounced tenorite band edge and defect emission arising from copper and oxygen vacancies is detected below 1.8 eV. Local differences of the emission, especially in the near IR, reveal inhomogeneity in terms of defect concentration and phase composition. After annealing at 1000 °C in nitrogen atmosphere, the nanoparticles are completely transformed into the cuprite phase. The intensity of the band edge emission increases by more then two orders of magnitude indicating high quality material. Moreover, no significant local variations are observed any more. The emission in the near IR primarily arises from copper vacancies.

The high PL intensity demonstrates the high quality of the tenorite and cuprite nanoparticles that can be achieved by proper oven annealing and indicates the suitability of this material for photovoltaic applications. In comparison to results reported for tenorite bulk material, nanoparticles include fewer defects and therefore show superior opto-electronic properties. The cuprite nanoparticles exhibit excellent properties at least similar to high quality bulk material.

Chapter 5

Characterization & modification of iron oxide nanoparticles

This chapter is dedicated to the characterization and modification of iron oxide nanoparticles. Commercially available maghemite nanoparticles, which are purchased as powder from IoLiTec GmbH [1], and hematite nanoparticles dispersed in water, which are provided by the Institute of Interactive Materials Research DWI an der RWTH Aachen e.V. [2] are investigated. In context of a diploma thesis, laser annealing experiments were conducted in order to analyze the properties of the commercially available maghemite nanoparticles. The main results are summarized in the beginning of this chapter. Preliminary TEM experiments are performed to investigate the size, shape, and phase of the nanoparticles. The maghemite nanoparticles are annealed up to 900°C in nitrogen atmosphere. The modifications of the structural and opto-electronic properties are investigated by Raman and PL spectroscopy. On the same sample several sample spots are analyzed in order to probe the homogeneity of the material. Furthermore, the optical absorption is characterized by PDS. Raman, PL, and PDS spectra as well as TEM images of the hematite nanoparticles that are provided by the DWI are taken. The results are compared to the results of the oven annealing series.

[1] http://www.iolitec.de/
[2] http://www.dwi.rwth-aachen.de/

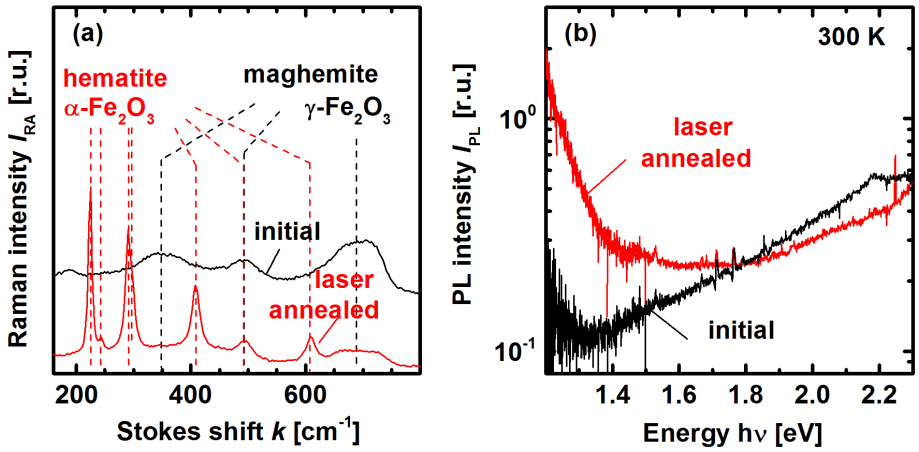

Figure 5.1 *– Raman (a) and PL (b) spectra of commercially available iron oxide nanoparticles measured at room temperature after Jan Flohre [21]. All spectra were taken on the same spot with a laser excitation power of about 1.6 Wcm^{-2} before (black line) and after (red line) a laser treatment with a laser excitation power of 10 Wcm^{-2} for ten minutes in air. References for the maghemite and hematite Raman modes of bulk material are indicated by black and red dashed lines, respectively [128].*

5.1 Summary of the related diploma thesis

In his diploma thesis, Jan Flohre investigated commercially available maghemite nanoparticles [21]. Raman and PL spectra were detected at room temperature with an excitation laser power of about 1.6 Wcm^{-2}. Then the nanoparticles were annealed with a laser power of about 10 Wcm^{-2} under ambient atmosphere for ten minutes, before again Raman and PL measurements were performed with the low laser power. Figure 5.1 (a) shows the Raman spectra before (black line) and after laser annealing (red line). The spectrum of the as-prepared nanoparticles exhibited three broad features at about 350 cm^{-1}, 500 cm^{-1}, and 700 cm^{-1}, which are characteristic for maghemite [128]. After the laser annealing step, various peaks were detected, which are typical for the hematite phase [128]. In conclusion, the maghemite nanoparticles were transformed into the hematite phase due to the laser treatment. Figure 5.1 (b) illustrates the corresponding PL spectra in the region between 1.2 eV to 2.3 eV, which were measured at room temperature. Before laser annealing (black line), the PL signal increased between 1.3 eV and 2.3 eV and showed a weakly pronounced emission signal at about 2.2 eV. This emission was believed to originate from the quartz substrate. After the laser annealing step, a high PL signal is indicated at low energy outside of the detection range. This emission was suggested to be the falling

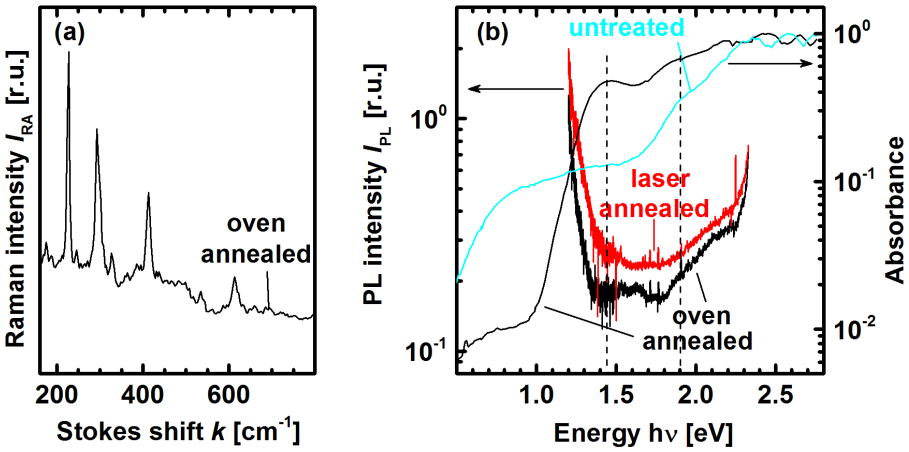

Figure 5.2 – *Figure (a) illustrates the Raman spectrum of the iron oxide nanoparticles after the oven annealing step at 1000 °C for 30 minutes under nitrogen atmosphere after Jan Flohre [21]. Figure (b) shows the corresponding PL and PDS spectra (black line). For comparison, the emission signal of the laser annealed nanoparticles (red line) and the absorptance of the as-prepared nanoparticles (cyan line) are presented.*

edge of an emission peak located at energies lower than 1.2 eV. Between 1.8 eV and 2.3 eV, the emission increases slightly.

For comparison, the maghemite nanoparticles were also annealed in an oven at 1000 °C under nitrogen atmosphere. Figure 5.2 (a) and (b) show Raman and PL spectra of the iron oxide nanoparticles after the oven annealing step (black line). The Raman spectrum clearly indicated the transition from the maghemite to the hematite phase after the annealing step. Compared to the hematite nanoparticles that are obtained by laser annealing, a similar emission is observed in the near IR. The origin of this emission could not be identified. Above 1.4 eV two weakly pronounced and broad emission bands were detected between 1.4 eV to 1.8 eV, and 1.8 eV to 2.3 eV. At 2.3 eV the emission seemed to increase more strongly. The emission bands above 1.4 eV were not discussed in detail, but were believed to originate from the quartz substate.

Figure 5.2 (b) also illustrates the absorptance of the as-prepared (cyan line) and oven annealed nanoparticles (black line), which were determined by PDS. The absorptance of the as-prepared nanoparticles increased between 1.6 eV and 2.2 eV by about one order of magnitude which hinted at the optical band gap of about 2 eV which is reported in the literature for bulk material [5]. Moreover, a high sub gap absorption was observed, which was attributed to defect absorption, and which was probably the reason that no band edge emission was detected due to defect related

non-radiative recombination.
After oven annealing, the absorptance increased by about one order of magnitude between 0.9 eV and 1.3 eV, passed a maximum at 1.4 eV and increased further, before it saturated at about 2.3 eV. At about 1.9 eV the same unidentified absorption band that was already observed in the absorptance of the as-prepared nanoparticles was detected. The absorption edge at about 1 eV was in good agreement with the near IR emission of the laser and oven annealed nanoparticles. However, the origin of these features remained unexplained.

5.2 Pre-examination of maghemite nanoparticles by TEM

Commercially available maghemite (γ-Fe_2O_3) nanoparticles with a nominal diameter of 8 nm to 15 nm are purchased as powder from IoLiTec GmbH [3]. These nanoparticles are dispersed in deionized water by treatment in an ultrasonic bath. For preliminary TEM measurements a TEM grid [4] is coated with nanoparticles by dipping it into the dispersion and subsequent drying in air. Figure 5.3 (a) shows a bright field image of the untreated maghemite nanoparticles. No single nanoparticles but large agglomerates are found on the sample. By adding oleic acid to the dispersion, the nanoparticles could be stabilized. When this stabilized nanoparticles are transferred onto the TEM grid, almost no agglomerates are formed (cf. figure 5.3 (c)). According to the TEM images, facetted nanoparticles with a diameter of about 6 nm to 18 nm are found. Figure 5.3(c) illustrates a representative diffraction pattern corresponding to the bright field image in figure 5.3 (a). The diffractrogram in figure 5.3 (b) is derived from the angular integration of the diffraction pattern shown as inset in figure 5.3 (c). It exhibits a multitude of reflexes resulting from the different crystallographic orientations of the nanoparticles, similar to a powder pattern. Reflexes referring to characteristic maghemite lattice distances are observed.[5]

5.3 Oven annealing of iron oxide nanoparticles

In the course of Jens Bergmann's diploma thesis, the PL and Raman setup was optimized in terms of its sensitivity. Moreover, it was extended by an InGaAs detector, which widened the detectable region to the near IR [22]. This allows to investigate the emission of the hematite nanoparticles which was indicated in Jan Flohre's diploma thesis [21]. For this, the commercially available maghemite

[3] http://www.iolitec.de/
[4] Copper grid with carbon film (Lacey-Carbon)
[5] The reference data is taken from the International Centre for Diffraction Data (ICDD), identification number: 00-039-1346.

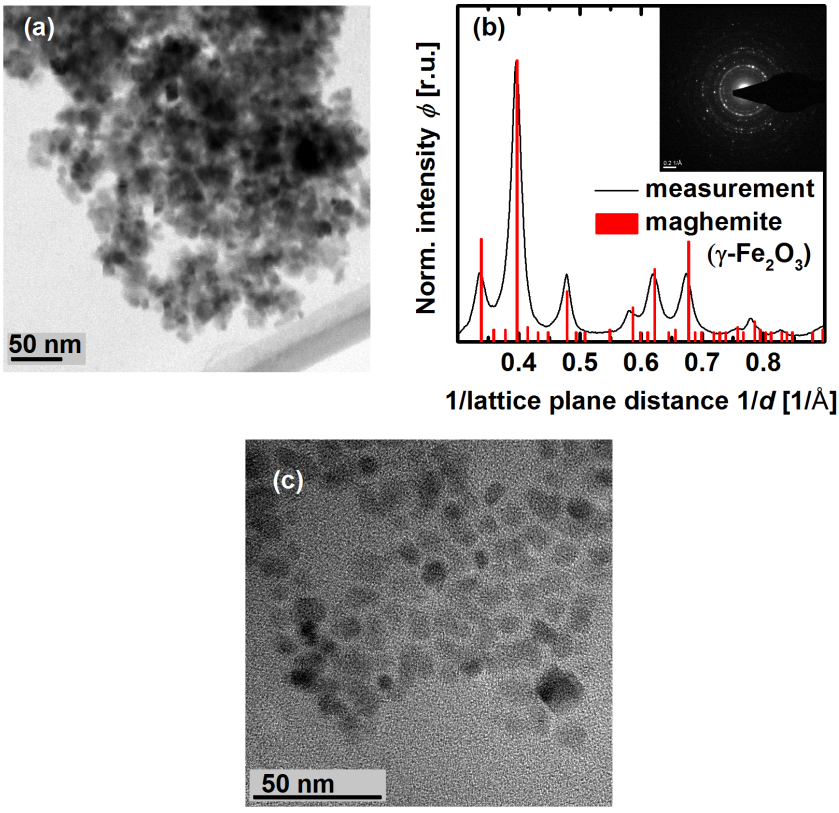

Figure 5.3 – *TEM bright field images of untreated maghemite nanoparticles (a) and nanoparticles that are stabilized by oleic acid (c). The diffractogram (b) corresponds the bright field image (a) and is calculated from the angular integration of the diffraction pattern that is shown as the inset. For comparison, literature data for the maghemite phase is indicated by the red bars. The reference data is taken from the International Centre for Diffraction Data (ICDD), identification number: 00-039-1346.*

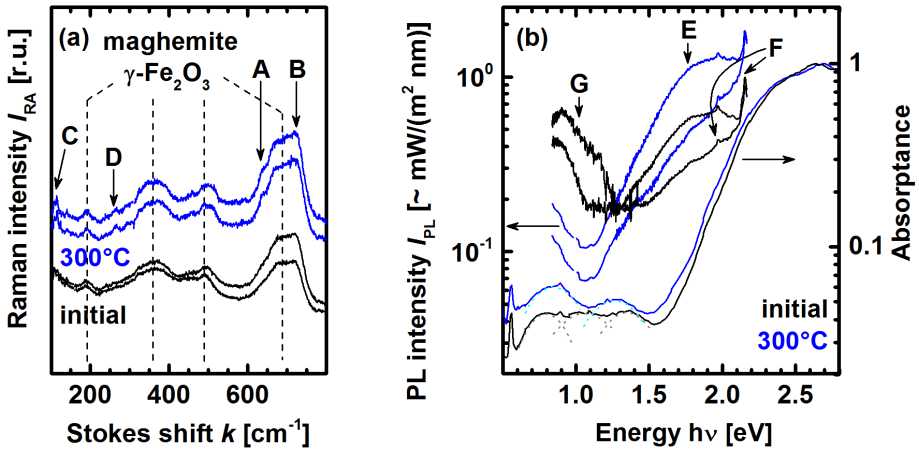

Figure 5.4 *– (a) Representative Raman spectra of the as-prepared nanoparticles (black line) and the nanoparticles that are annealed at 300 °C in nitrogen atmosphere (blue line). Reference data for the maghemite Raman modes of bulk material are indicated by black lines [128]. (b) shows the corresponding PL and PDS spectra.*

nanoparticles are annealed stepwise in nitrogen atmosphere up to 900 °C. After each annealing step, Raman and PL measurements were detected from various sample spots. Furthermore, PDS measurements are performed to analyze the absorption characteristics. For the sake of clarity, only two representative Raman and PL spectra are presented for each annealing step.

5.3.1 Untreated maghemite nanoparticles and nanoparticles annealed at 300 °C

Figure 5.4 (a) illustrates representative Raman spectra of the as-prepared nanoparticles (black line) and the nanoparticles that are annealed at 300 °C (blue line). All spectra exhibit the three broad features at about 350 cm^{-1}, 500 cm^{-1}, and 700 cm^{-1}, which are characteristic for the maghemite phase [128]. According to the reference spectra presented in figure 3.15 (a), the Raman modes at about 190 cm^{-1} is also attributed to the maghemite phase. The Raman spectra of the untreated and annealed nanoparticles look similar. But the shoulder at the low energy side of the broad band at about 700 cm^{-1} (A) as well as the signal at 720 cm^{-1} (B) are slightly more pronounced after the annealing step. Moreover, two weakly pronounced Raman signals are detected at about 114 cm^{-1} (C) and 263 cm^{-1} (D). At least the latter Raman peak can be ascribed to the maghemite phase [128]. Investigating different spots reveals no significant differences. Merely, the intensity of the structure

at 700 cm^{-1} varies slightly. For the sake of clarity only two spectra of each sample are presented.

Figure 5.4 (b) shows the corresponding PL and PDS spectra of the as-prepared nanoparticles (black line) and after annealing at 300 °C (blue line) in the spectral region from the near IR to the visible. Subsequently, the description of the absorption and emission results is divided into two paragraphs: (1) the region of the band gap above about 1.6 eV and (2) the sub gap region below 1.6 eV. In each paragraph firstly the results of the as-prepared and afterwards of the annealed nanoparticles are described.

In the spectral region between 1.6 eV and 2.3 eV, the absorptance spectra of the as-prepared nanoparticles (black line) increases by more than one order of magnitude. In the region of the band gap, the corresponding PL spectra (black line) exhibit a broad emission signal (E) with several peaks located between 1.7 eV and 2.2 eV. The most intensive features are peaked at 1.97 eV and 2.15 eV with a shoulder at 2.13 eV (F).[6] Comparing the emission of different sample spots, the intensity of the broad emission varies. No correlation between the varying intensity of the Raman mode at 700 cm^{-1} and the PL emission is found.
After annealing at 300 °C (blue line), no significant changes of the absorptance is observed above 1.6 eV. Furthermore, the overall signature of the broad emission signal remains unchanged. Again, the intensity of this emission varies with the sample spot. In general, a slightly higher intensity is observed compared to the intensity of the untreated nanoparticles. In the region between 1.7 eV and 2.2 eV the previously described fine structure of several sharp emission peaks is also detected.

Below 1.6 eV a high sub gap absorption is observed for the as-prepared nanoparticles. As indicated by the grey dotted lines, three absorption features peaked at about 0.79 eV, 1.07 eV, and 1.35 eV can be identified contributing to the sub gap absorption. The corresponding PL spectra exhibit an emission in the near IR (G). Depending on the sample spot, the spectral distribution of this emission varies. Again, no correlation between the variation of this emission in the near IR and the varying intensity of the Raman mode at 700 cm^{-1}, or the PL emission above 1.6 eV is found.
Also after annealing at 300 °C, a high sub gap absorption is detected. But only two absorption features centred at about 0.85 eV and 1.28 eV are observed (indicated by cyan dotted lines). In comparison to the untreated sample, the emission below 1.3 eV is significantly reduced.

5.3.2 Annealing of maghemite nanoparticles at 450 °C and 550 °C

Figure 5.5 (a) illustrates several Raman spectra of the nanoparticles that are annealed at 450 °C (green line) and 550 °C (orange line). The black and grey dashed

[6] A detailed view of this fine structure will be presented in the discussion (cf. section 5.5.3).

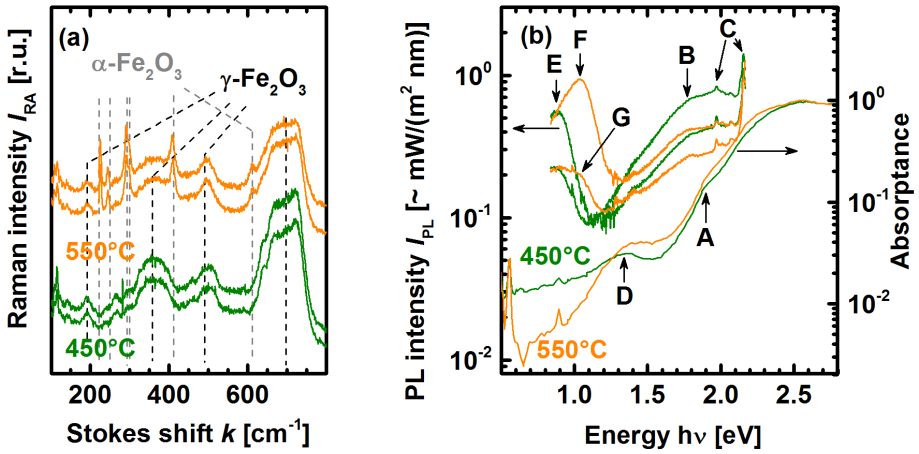

Figure 5.5 – *(a) illustrates representative Raman spectra of the nanoparticles that are annealed at 450 °C (green line) and 550 °C (orange line) in nitrogen atmosphere. Reference data for the maghemite and hematite Raman modes of bulk material are indicated by black and grey dashed lines, respectively [128]. (b) shows the corresponding PL and PDS spectra.*

lines indicate characteristic Raman modes of the maghemite and hematite phase, respectively [128]. The spectra of the nanoparticles that are annealed at 450 °C exhibit the broad features that are typical for maghemite. There is no indication for the presence of hematite.
Also, the Raman spectra of the nanoparticles that are annealed at 550 °C show the signature of the maghemite phase. However, additional sharp Raman modes are observed, which match well with the Raman frequencies that are reported in the literature for hematite bulk material [128].

The corresponding absorption and emission spectra are presented in figure 5.5 (b). Again, the discription of the results in the spectral region of the band gap and the sub gap region are presented separately.

Similar to the spectra discussed before, the absorptance of the nanoparticles that are annealed at 450 °C (green line) strongly increases between 1.6 eV and 2.2 eV. An absorption feature is detected at about 1.9 eV (A). Again, a broad PL signal (B) is detected in the region of the band gap accompanied by sharp emissions (C) in the region between 1.8 eV to 2.2 eV. Comparing the emission of different sample spots, the intensity and spectral distribution of the broad emission varies slightly.
After annealing at 550 °C, no fundamental changes of the absorptance and emission spectra (orange line) are observed above 1.6 eV compared to the previous annealing step. But, the emission intensity of the broad emission (B) is lower. Again, the intensity of this emission varies for different sample spots.

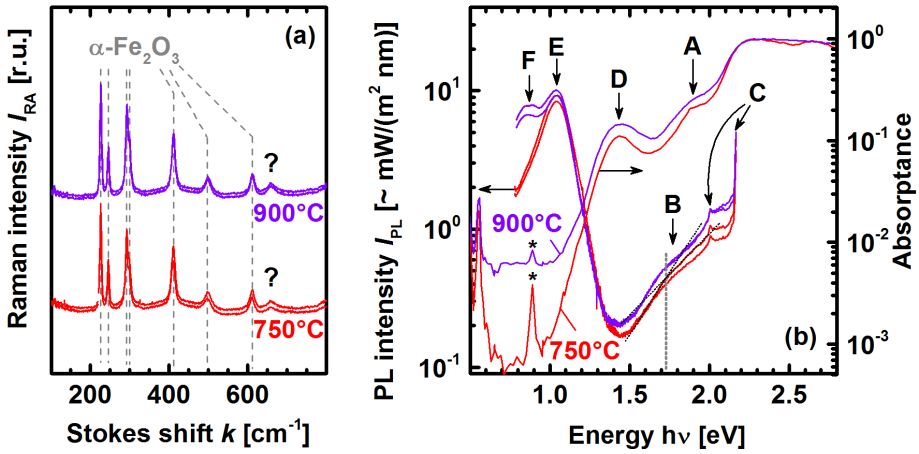

Figure 5.6 – *(a) illustrates representative Raman spectra of the commercially available iron oxide nanoparticles annealed at 750 °C (red lines) and 900 °C (purple lines) in nitrogen atmosphere. References for the hematite Raman modes of bulk material are indicated by grey dashed lines [128]. Figure (b) shows the corresponding PL and PDS spectra.*

Still, a high sub gap absorption is detected for the nanoparticles that are annealed at 450 °C (green line) below 1.6 eV with a prominent absorption feature at about 1.35 eV (D). Moreover, the PL spectra exhibit an emission at about 0.9 eV (E). After annealing at 550 °C (orange line), the general signature of the absorption below 1.6 eV is similar to the previous annealing step, but the absorption is significantly reduced in the spectral region below 1.2 eV. Between 0.8 eV and 1.4 eV, the PL spectra show a broad emission band. The representative PL spectra illustrate that the spectral distribution of this emission varies with the investigated sample spot. Here, two spectra are depicted for clarity. For most spots, a dominant emission peak is detected at 1 eV (F).

5.3.3 Annealing of maghemite nanoparticles at 750 °C and 900 °C

After annealing at 750 °C (red line) and 900 °C (purple line) the Raman spectra exhibit characteristic hematite Raman modes and no indication for the presence of maghemite is observed (cf. figure 5.6 (a)). Only the peak at about 660 cm^{-1} (labeled by a question mark ?) cannot be identified with a typical hematite Raman mode. No significant differences between the different spots of the sample are detected.

The corresponding absorption and emission spectra are presented in figure 5.6 (b). As before, the absorption and emission characteristics in the spectral region of the band gap are described for both samples, before the sub gap region is regarded.

Between 1.6 eV to 2.2 eV, the absorptance of the nanoparticles annealed at 750 °C (cf. figure 5.6 (b), red line) increases by almost one order of magnitude at which the previously mentioned absorption feature is visible as a hump at about 1.9 eV (A). Above 1.5 eV, the corresponding PL signals exhibit a broad emission (B). Between 1.5 eV and 2.2 eV the PL signal increases by about a factor of five, in which the rise of the emission flattens at about 1.7 eV (indicated by the dotted lines). Again, between 1.9 eV and 2.2 eV several sharp emissions are observed. In comparison to the emission signals that are previously described in this chapter, these sharp emission peaks are slightly blue-shifted (C). Moreover, no shoulder is observed at the low energy rise of the pronounced peak at about 2.15 eV.[7]
After annealing at 900 °C, the general shape of the absorption and emission spectra does not change significantly above 1.6 eV. Merely, the absorption feature at 1.9 eV (A) is considerably broader and the intensity of the broad emission (B) is slightly higher. Note, that for both samples almost no local variations are observed for different sample spots.

Between 1 eV to 1.2 eV the absorption of the nanoparticles annealed at 750 °C (red line) increases by more than one order of magnitude, reaching a maximum at about 1.45 eV. The sharp feature at about 0.9 eV can be assigned to oxygen vibrations in the quartz substrate (labeled by the asterisk *). Below 1.5 eV a strongly pronounced emission is observed with its maximum peaked at about 1 eV.
Annealing at 900 °C (purple line), the absorption below 1 eV increases by a factor of five. Moreover, the absorption maximum (D) at about 1.45 eV is broader. The most striking difference is detected for the emission in the near IR. At 0.9 eV, a second emission peak (F) arises at the low energy rising edge of the pronounced emission at 1 eV (E).

5.4 Characterization of hematite nanoparticles from the DWI

In addition to the comercially available maghemite nanoparticles, hematite nanoparticles are provided by the Institute of Interactive Materials Research DWI an der RWTH Aachen e.V.[8]. The nanoparticles are prepared according to the synthesis reported by Ozaki et al. [142] and are available as a dispersion in water with a concentration of about 1.5 (wt)%. These nanoparticles are investigated by Raman, PL, and PDS spectroscopy as well as TEM measurements in order to analyze their

[7] A detailed presentation of the fine structure of the emission in the spectral region of the band gap is given in section 5.5.3.
[8] http://www.dwi.rwth-aachen.de/, in the following referred to as DWI.

structural and opto-electronic properties. For PL, Raman, and PDS measurements, one drop of the dispersion is placed on a quartz substrate and is allowed to dry in air. A TEM grid is coated with the nanoparticles, by dipping the grid into the dispersion and subsequent drying in air.

5.4.1 TEM pre-examination of the hematite nanoparticles from the DWI

The figures 5.7 (a), (c), and (d) illustrate bright field images of the hematite nanoparticles that are obtained from the DWI. The TEM measuremente reveal a narrow size distribution with diameters of mainly about 45 nm to 60 nm and a facetted shape.[9] The nanoparticles do not tend to agglomerate. The figures 5.7 (c) and (d) show a high resolution bright field image of a single hematite nanoparticle and its magnification, respectively. Clearly, lattice planes, which extends over the whole nanoparticle without changing the crystallographic orientation, are visible in the magnification. The diffraction pattern of all nanoparticles that are shown in figure 5.7 (a) is given in figure 5.7 (b). The diffractrogram is calculated from the angular integration of the pattern, which is displayed as an inset. It shows a multitude of reflexes resulting from the different crystallographic orientations of the nanoparticles. For comparison, reference data for typical hematite reflexes are given (red bars) after Pailhe et al. [143].

5.4.2 Raman, PL, and PDS measurements of the hematite nanoparticles from the DWI

The hematite nanoparticles from the DWI are deposited by dropping about 50 µl of the dispersion onto a quartz substrate and subsequent drying in air. In contrast to the TEM grid which is just dipped into the dispersion, a considerably larger amount of nanoparticles is deposited when a drop of the dispersion is allowed to dry on the quartz substrate. On the substrate, the nanoparticles form a closely packed layer with a thickness of about 10 µm (cf. figures 5.8 (a) and (b)). Raman, PL, and PDS spectra of the hematite nanoparticles are detected (cf. figure 5.9).
The Raman spectrum exhibits characteristic hematite Raman modes and there is no indication for the presence of any other iron oxide phase. This spectrum of the DWI nanoparticles resembles those of the hematite nanoparticles that are obtained by annealing of maghemite nanoparticles at 750 °C or 900 °C (cf. figure 5.6 (a)). Even the unexplained mode peaked at about 660 cm^{-1} is detected (indicated by a question mark ?). Moreover, the absorption and emission characteristics are in general the same for both types of hematite nanoparticles. The absorption increases rapidly between 1 eV and 1.4 eV, passes through a local maximum at 1.4 eV (A)

[9] Robert Imlau, personal communication, January 2013

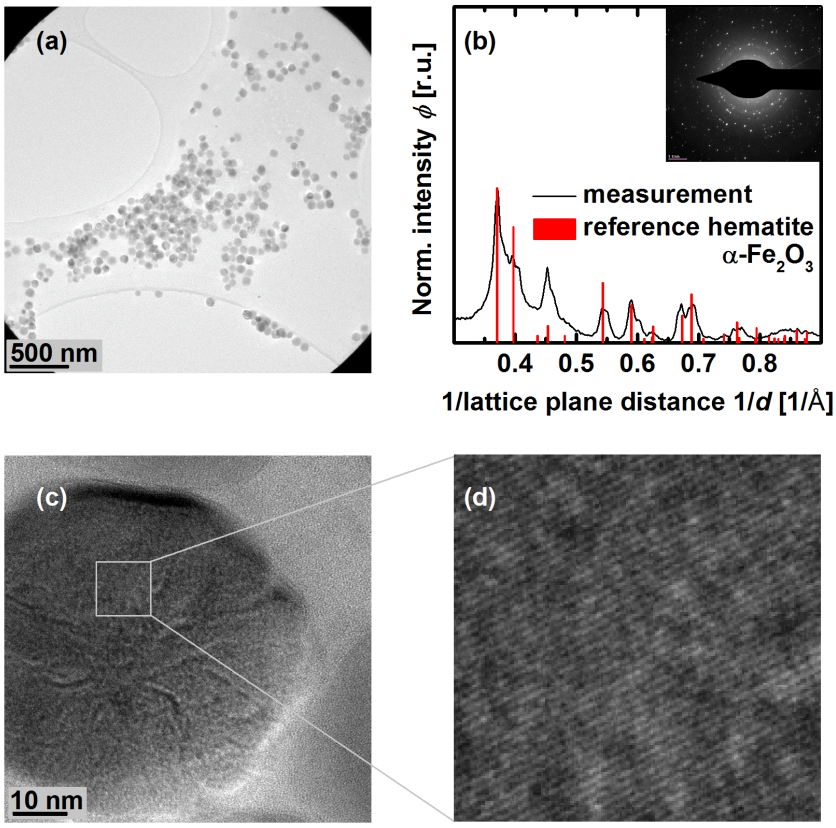

Figure 5.7 – *(a) TEM bright field image of hematite nanoparticles that are obtained from the DWI. (b) illustrates the corresponding angular integrated diffractogram of the diffraction pattern shown as the inset. The red bars indicate reference data for the hematite phase [143]. (c) gives a high resolution bright field image of a single nanoparticle. (d) shows a magnification of the single nanoparticle.*

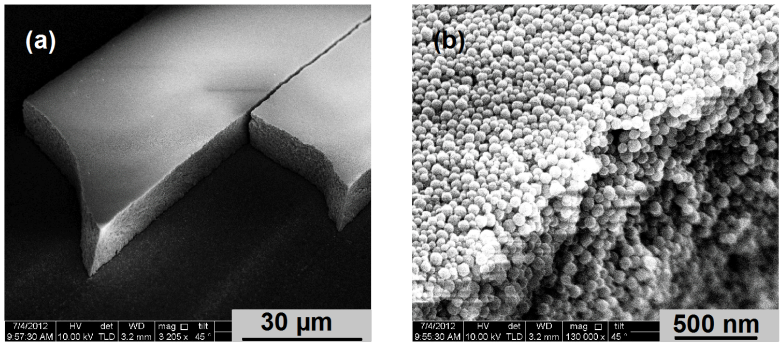

Figure 5.8 – *SEM images of films of hematite nanoparticles that are provided by the DWI. The samples are prepared by dropping about 50 µl of the dispersion onto a quartz substrate and subsequent drying in air.*

and increases further with an absorption feature at 1.9 eV (B) before it saturates at about 2.3 eV. Similar to the emission spectra, that are detected for the commercially available iron oxide nanoparticles that are transformed into the hematite phase, the emission spectrum shows a dominant peak at about 1.35 eV (C) and a broad emission between 1.5 eV to 2.2 eV (D) with several sharp emission lines (E) at about 1.97 eV, 2.01 eV, and 2.17 eV. Note, that the emission at 1.97 eV is not observed for the hematite nanoparticles of the oven annealed series after annealing at 750 °C and 900 °C.

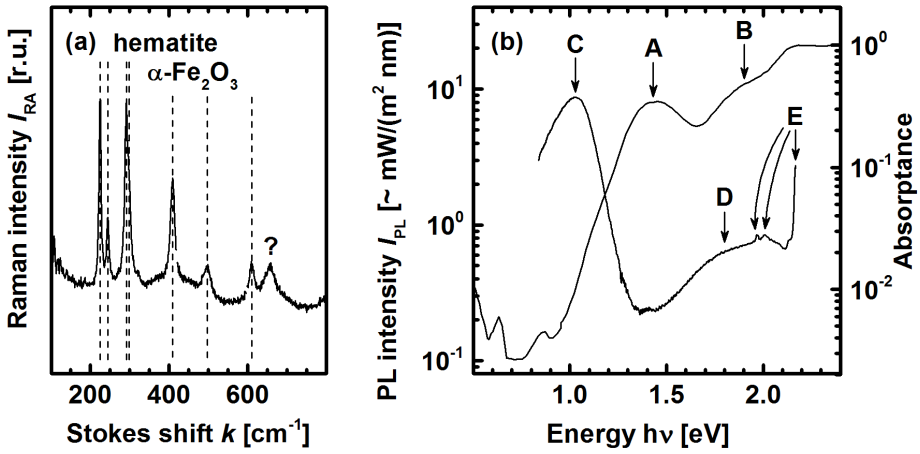

Figure 5.9 *– (a) shows the Raman spectrum of the hematite nanoparticles that are obtained from the DWI. Literature data for characteristic Raman modes of hematite bulk material are indicated by the dashed lines [128]. (b) illustrates the corresponding PL and PDS spectra.*

5.5 Discussion - modification of iron oxide nanoparticles

In the following, the results that are presented in the previous sections are interpreted and discussed with respect to results reported in literature. Firstly, it is focussed on the commercially available maghemite nanoparticles that are modified by oven annealing in nitrogen atmosphere. The experimental absorption and emission spectra presented in this thesis are compared to theoretical and experimental results from the literature. Finally, the properties of the hematite nanoparticles that are provided by the DWI, are compared to the commercially available nanoparticles.

5.5.1 Oven annealing of maghemite nanoparticles

According to the TEM measurements, the commercially available maghemite nanoparticles are highly crystalline and show diameters of 8 nm to 15 nm. By annealing in nitrogen atmosphere, the structural and opto-electronic properties of these nanoparticles are modified. For a detailed discussion, selected Raman, PL, and PDS spectra that are presented in the previous sections are subsequently illustrated.

Up to an annealing temperature of 450 °C the Raman spectra indicate that the nanoparticles are present purely in the maghemite phase. Figure 5.10 (a) illustrates three representative Raman spectra of the maghemite nanoparticles in

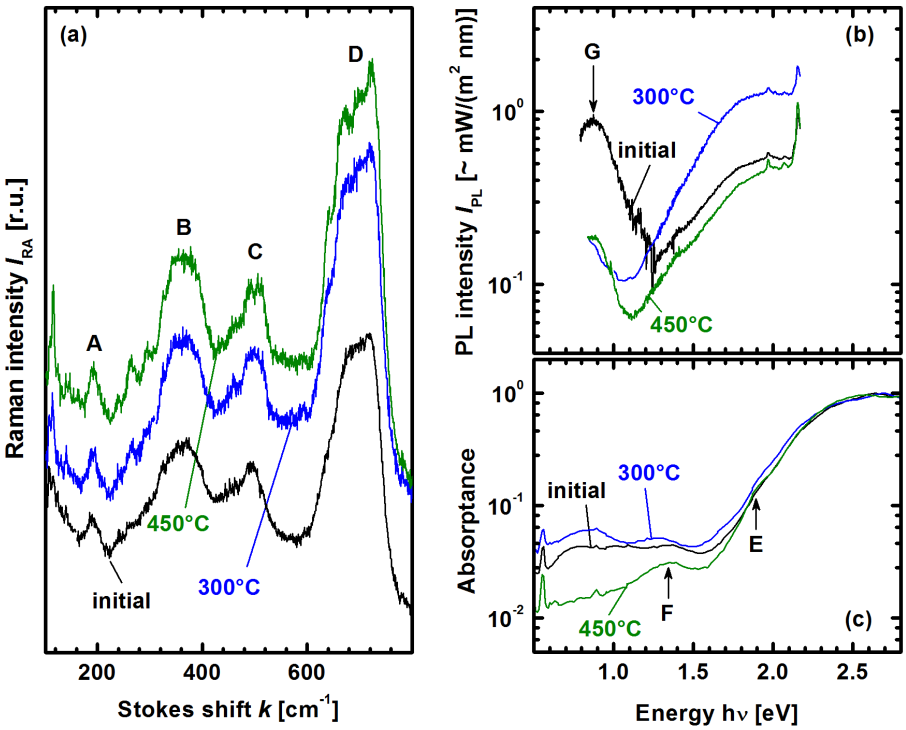

Figure 5.10 – *Representative Raman (a), photoluminescence (b), and PDS (c) spectra of the commercially available maghemite nanoparticles in the as-prepared state (black line), after annealing at 300 °C (blue line), and 450 °C (green line).*

the as-prepared state (black line), after annealing at 300 °C (blue line), and 450 °C (green line). All spectra exhibit broad Raman modes at 190 cm^{-1} (A), 350 cm^{-1} (B), 500 cm^{-1} (C), and 700 cm^{-1} (D) that are typical for the maghemite phase. But, after annealing, the nanoparticles, the relative contribution of the different modes change considerably and new peaks appear. In order to reveal the changes, Raman spectra of the as-prepared nanoparticles (black line) as well as after annealing at 450 °C (green line) are presented in figure 5.11 (a) along with the difference between the two spectra given in figure 5.11 (b). After annealing, Raman modes occur at about 110 cm^{-1} (E), 260 cm^{-1} (F) and 290 cm^{-1} (G). Though not explicitly mentioned in the literature, similar features are observed in the literature, and can therefore be ascribed to the maghemite phase (cf. section 3.2.5, figure 3.15 (a)). Moreover, the broad Raman modes at 350 cm^{-1} (B), 500 cm^{-1} (C), and 700 cm^{-1} (D) exhibit pronounced features at 345 cm^{-1} (H), 511 cm^{-1} (I), 642 cm^{-1} (J), 670 cm^{-1} (K), and 725 cm^{-1} (L). This fine structure of the broad peaks is also reported in the

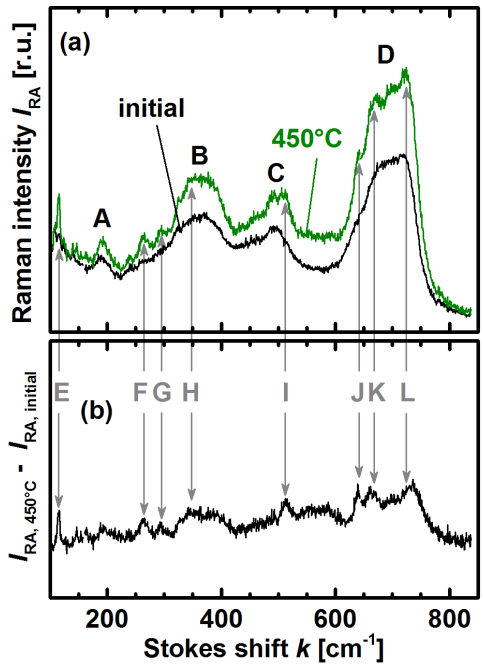

Figure 5.11 *– (a) Representative Raman spectra of the commercially available maghemite nanoparticles in the as-prepared state (black line) and after annealing at 450 °C (green line). (b) Deviation of the two Raman spectra shown in (a).*

literature for maghemite[125]. Note, that the occuring Raman modes do not match with characteristic combinations of Raman modes of any other iron oxide or iron hydroxide [127]. The changes of the relative contribution of the different modes and the occurance of new Raman modes with increasing annealing temperature might indicate a higher structural order. As mentioned in section 3.2, the maghemite phase is metastable and can be described as a Fe^{2+} deficient magnetite phase. The distribution of the Fe^{2+} vacancies depends on the preparation technique. Either the vacancies order in superstructures (tetragonal or tetrahedral), or occur in a disordered distribution [113, 114, 115]. At elevated annealing temperatures, the cations and anions tend to migrate and occupy energetically beneficial positions. Though no evidence is found in the literature, the changes of the Raman signal might indicate that the vacancies form a more ordered superstructure at tetragonal or tetrahedral sites at elevated annealing temperatures.

In the following, the absorption characteristics of the nanoparticles annealed up to 450 °C are discussed. For the sake of clarity, the corresponding absorption spectra that are already presented in the previous sections are given in figure 5.10 (c).

Between 1.5 eV and 2.2 eV the absorptance of the as-prepared nanoparticles and after annealing at 300 °C and 450 °C increase by more than one order of magnitude. The deduced band gap is in good agreement with the optical band gap of about 2 eV that is reported for maghemite bulk material in the literature [5]. After annealing at 450 °C, an absorption feature is visible as a hump at about 1.9 eV indicated by E in figure 5.10 (c). According to Sherman et al., this feature is ascribed to the ligand field transition ${}^6A_1 \rightarrow {}^4\ T_2({}^4G)$ of octahedrally coordinated Fe^{3+} ions [103, 101].
After annealing at 300 °C the absorption below 1.1 eV decreases and decreases further after annealing 450 °C significantly, whereas an absorption maximum at about 1.35 eV (F) remains prominent. These changes suggest different physical origins for the absorption between 0.5 eV to 1.1 eV and 1.1 eV to 1.5 eV. Sherman et al. claim, that the absorption maximum at 1.35 eV can be associated with the multiplet ${}^6A_1 \rightarrow {}^4\ T_1({}^4G)$ that arise from the $2t_{2g}^{\downarrow}$ and $4e_g^{\uparrow}$ energy levels of the iron $3d$ electrons that are split in the ligand field of the octahedrally coordinated cluster $(FeO_6)^{9-}$ [103, 101].
The absorption feature at 1.9 eV and the maximum at 1.35 eV along with classification to the ${}^6A_1 \rightarrow {}^4\ T_2({}^4G)$ and ${}^6A_1 \rightarrow {}^4\ T_1({}^4G)$ compare well to the theoretical and experimental data that are summarized in table 3.3. The absorption below 1.1 eV cannot be attributed to such a transition and is believed to arise from defects. Hence, the reduction of this absorption after annealing at 450 °C indicates a reduction of the defect concentration.

The corresponding emission spectra of the three samples reveal a broad emission between 1.5 eV and 2.2 eV accompanied by sharp emission lines at 1.97 eV, 2.07 eV, and most dominant at 2.15 eV with a shoulder at the low energy side. This fine structure is discussed separately in section 5.5.3. The broad emission is attributed to maghemite band edge emission. Furthermore, the intensity of the broad emission varies with the sample spot (cf. figures 5.4 (b) and 5.5 (b)). Hence, the nanoparticles are not modified equally. Consequently, differences in terms of defect concentration are probably present leading to different emission intensities.
Furthermore, the increase of the broad emission of the nanoparticles annealed at 300 °C is substantially steeper than for the as-prepared nanoparticles and after annealing at 450 °C, whereas no variation of the slope of the respective PDS spectra is observed in the corresponding spectral region. By PDS, a macroscopic spot is investigated and a large number of nanoparticles contribute to the signal, which represents the average absorption properties. The PL spectra are detected from a significantly smaller spot, and thus fewer nanoparticles are probed. In contrast to the PDS measurements, exclusively the radiative transitions are observed in the PL spectra. Since the slope of the emission does not compare with the slope of the absorption, this gives strong evidence, that different nanoparticles exhibit different electronic properties. The nanoparticles with the lowest defect concentration govern the emission spectra, whereas the average absorption characteristics of all probed

nanoparticles contribute to the PDS spectra.
For the as-prepared nanoparticles an emission peak is detected in the near IR at about 0.9 eV. After annealing at 300 °C this emission vanishes, but reappears after further annealing at 450 °C. The origin of this near IR emission cannot be explained unambigeously. On the one hand, it could arise from the ${}^6A_1 \rightarrow {}^4\ T_1({}^4G)$ ligand field transition. On the other hand, it could be related to transitions involving deep defect states that form energy levels in the middle of the optical band gap. Note, that the intensity of the broad emission is higher and the emission in the near IR is hardly observed after annealing at 300 °C, whereas less emission is detected above 1.5 eV and stronger emission is detected in the near IR for the as-prepared nanoparticles or after annealing at 450 °C. This indicates competing transition mechanisms, but a detailed analysis would require larger statistics.

After annealing at 550 °C, the Raman spectrum reveals the presence of the maghemite as well as the hematite phase (cf. figure 5.12 (b), orange line). So far, it is not clear if different phases are present in different nanoparticles or if single nanoparticles contain both phases.

In the literature, the optical band gap of maghemite and hematite are found to be at about 2 eV to 2.2 eV [5]. According to Sherman et al., the electronic structure of both phases is dominated by Fe^{3+} ions that are octahedrally coordinated with oxygen atoms [101]. Hence, similar absorption characteristics are expected.

Comparing the absorptance of the nanoparticles that are annealed at 450 °C and 550 °C, no significant changes are detected above 1.6 eV (cf. figure 5.12 (c), green and orange lines). In the near IR, the general absorption features remain unchanged, but the absorption below 1.1 eV is further reduced. This reduction can probably be explained by the annealing of defects, and thus less defect absorption.

Comparing the absorption feature at about 1.35 eV (A), differences between the two absorption spectra are observed. After annealing at 550 °C, this feature seems to be blue-shifted in comparison to the previous annealing step, which is explained by the influence of the defect absorption. Below 1.1 eV, the sub gap absorptions exhibit an exponential behaviour. As illustrated in figure 5.13 (a), the influence of this absorption is corrected by substraction of exponential trends (indicated by the black dotted lines). After this correction (dashed-dotted lines), the absorption feature is at the same position (A). Furthermore, after annealing at 550 °C, no minimum is observed at about 1.5 eV which may be explained by the beginning phase transition into the hematite phase leading to variations of the atomic distances, and thus altering the electronic structure. But, the missing minimum could also be a result of a suboptimal correction.
The emission above 1.5 eV is only weakly affected by the annealing step. Merely, an additional sharp peak is detected in the fine structure at about 2.01 eV, which is discussed in section 5.5.3. In the near IR, a strong emission centered at 1 eV with a shoulder at the low energy site is observed. The shoulder corresponds probably to the emission that is detected after the previous annealing step. The origin of these

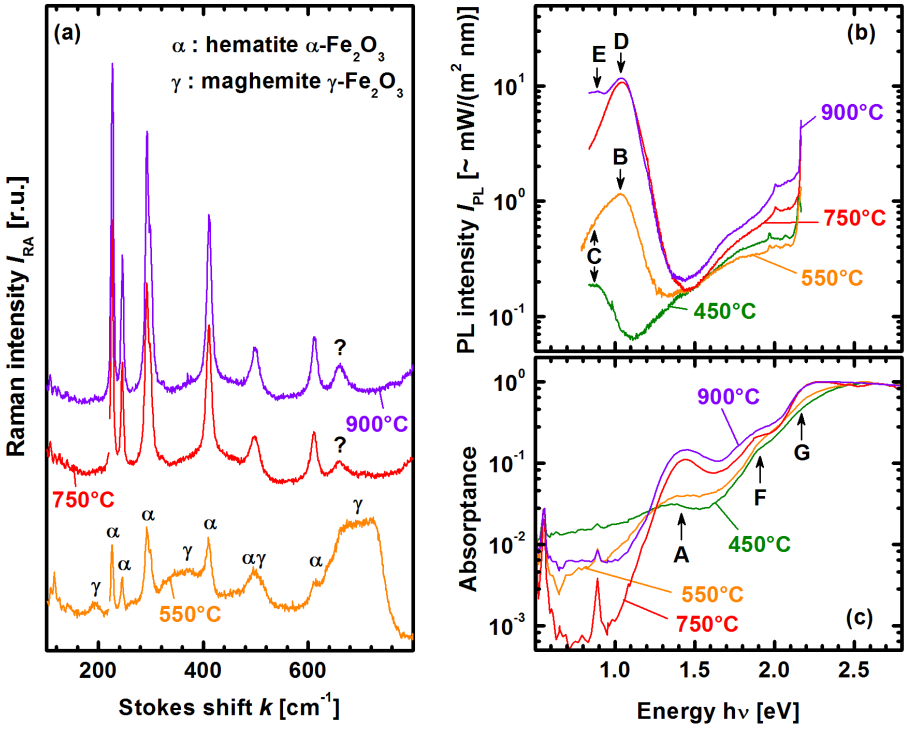

Figure 5.12 – *Representative Raman spectra (a), PL spectra (b), and PDS spectra (c) of the commercially available maghemite nanoparticles after annealing at 550 °C (orange line), 750 °C (red line), and 900 °C (purple line). For comparison, the PL and PDS spectra of the sample that is annealed at 450 °C (green line) is also presented.*

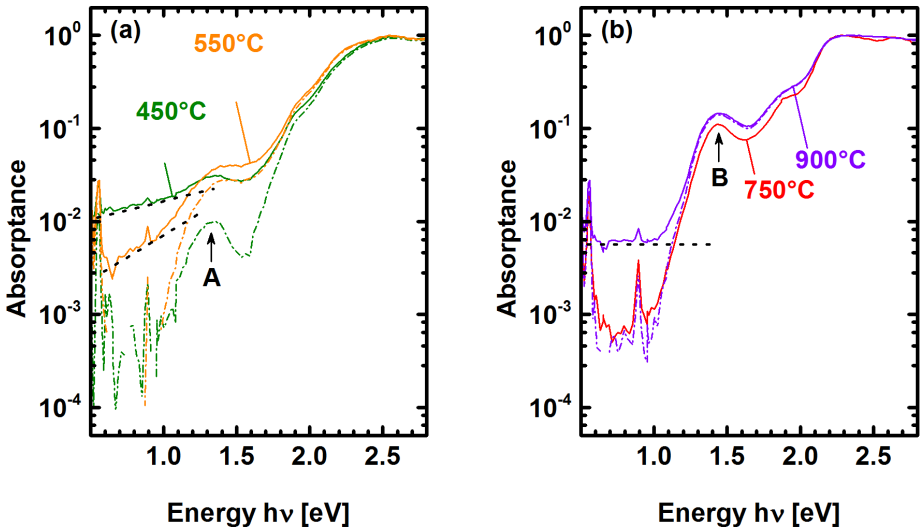

Figure 5.13 – *(a) illustrates the PDS spectra of the nanoparticles annealed at 450 °C (green line) and 550 °C (orange line) as well as the corresponding spectra (dashed-dotted lines) corrected for the sub gap absorption by substraction of a exponential trends (indicated by the black dotted lines). (b) gives the PDS spectra of the nanoparticles annealed at 750 °C (red line) and 900 °C (purple line). For the latter the sub gap absorption was also substracted (dashed-dotted line).*

features cannot finally be explained. For hematite, the energy of the ${}^6A_1 \rightarrow {}^4T_1({}^4G)$ transition is found at 1.40 eV, whereas a slightly lower energy of 1.32 eV is reported for the maghemite phase [103]. Hence, the contributions at 0.9 eV and 1 eV could arise from the ${}^6A_1 \rightarrow {}^4T_1({}^4G)$ transitions of the maghemite and hematite phase, respectively. If the emission bands at 0.9 eV and 1. eV are associated with the ligand field transitions at 1.3 eV and 1.4 eV, this implies a very large stokes shift for the emission bands of about 0.4 eV. Contingently, the involvement of tail states or variation of the electron-phonon coupling may explain the shift to lower energies. On the other hand, radiative recombination from defect states located deep in the band gap could be responsible for this emission. As described in section 3.2.4, Wang et al. report the observation of PL emission of hematite microparticles in the near IR, which is comparable to the results presented here (cf. figure 3.14). Wang et al. suppose the emission bands to originate from the ${}^6A_1 \rightarrow {}^4T_1({}^4G)$ ligand field transitions or transitions involving defect states arising from vacancies and/or impurity atoms for instance [120]. However, finally, the origin of the emission remains unexplained.

After annealing at 750 °C and 900 °C no maghemite but only hematite Raman modes are observed, which indicate that the initial maghemite nanoparticles are completely transformed into the hematite phase (cf. figure 5.12 (a)). Besides, a signal at 660 cm^{-1} is observed (indicated by the question mark). Shim and Duffy measured Raman spectra of hematite under pressure up to 62 GPa [144]. At high pressure, a Raman mode at 660 cm^{-1} was detected and attributed to an IR active mode [145]. According to the selection rules, this mode should not be Raman active. However, the selection rules are only strictly valid for a perfect and infinitely expanded crystal with a well defined symmetry. Surfaces, defects, and stress may disturb the symmetry and weaken the selection rules. Hence, the high surface to volume ratio of the nanoparticles as well as defects or stress could account for the observation of this mode in the Raman spectra. The discussion of this mode is picked up in section 5.5.4.

Figure 5.12 (c) illustrates the corresponding aborbance spectra. In general, the absorption features that are discussed for the nanoparticles annealed at 550 °C are also visible after annealing at 750 °C and 900 °C. Nevertheless, significant differences are observed. The absorption features that arise from the ligand field transitions (A, F) are stronger pronounced. Moreover, the increase of the absorptance above 2 eV is considerably steeper (G).
The sub gap absorption of the nanoparticles that are annealed at 750 °C (red line) is very low, which indicates a low defect concentration. After annealing at 900 °C (purple line), the sub gap absorption increases again, which suggests the introduction of defects at very high temperatures. Assuming an exponential trend for the sub gap absorption of the absorption after annealing at 900 °C (cf. figure 5.13 (b), dotted line), the influence of the sub gap absorption can substracted. After correction (pruple dashed-dotted line), the sub gap absorption is similar to that of the previous annealing step.
After annealing at 750 °C, the intensity of the emission centered at 1 eV increases by about one order of magnitude (D). In contrast to the corresponding emission detected for the nanoparticles annealed at 550 °C (B), no substantial contribution is observed at the low energy side of the peak (C). The emission at 1 eV is also observed after annealing at 900 °C. But, an additional emission is detected at its low energy side (E). The interpretation of the emission in the near IR is sophisticated. The emission peaked at 1 eV is solely observed when the hematite phase is present. Therefore, this emission is characteristic for the hematite phase. According to the discussion before, this feature might originate from ligand field transitions or involve defect states. The emission signal at 0.9 eV can neither be strictly attributed to the maghemite nor to the hematite phase. It is detected for the as-prepared (maghemite) nanoparticles, as well as after annealing at 450 °C (maghemite), 550 °C (maghemite and hematite), and 900 °C (hematite), whereas it is not or only weakly resolved after annealing at 300 °C (maghemite) and 750 °C (hematite) (cf. figures 5.10 (b) and 5.12 (b)). Though beeing located at the same position at 0.9 eV, the reason for

the emission of the maghemite and hematite nanoparticles could still be different. Above 1.5 eV, both spectra exhibit the broad emission accompanied by several sharp transitions that are mentioned earlier. The emission signal of the nanoparticles annealed at 900 °C is slightly higher compared to the previous annealing step indicating less non-radiative recombination. The sharp peak at 1.97 eV disappears and the dominant emission at 2.15 eV is slightly shifted to higher energies, which is discussed in section 5.5.3.

5.5.2 Absorption of maghemite and hematite

In order to investigate the quality of the nanoparticles, the absorptance spectra are compared to available data of maghemite thin films and bulk material. Figure 5.14 (a) illustrates the absorption coefficient of maghemite thin films that are prepared by sputtering (red circle) and epitaxially growth (blue square) after Wang et al. and Babkin et al., respectively [106, 105]. Moreover, 40 nm of epitaxially grown magnetite thin films provided by Leo Farrell [10] are investigated. These films are transformed into the maghemite phase by oven annealing at 350 °C. Its optical absorption is measured by PDS and is presented in figure 5.14 (a) (black line). The absorptance spectrum of the nanoparticles that are annealed at 450 °C is also shown (green line), but scaled for comparison to the reference data. The absorptance of the nanoparticles is scaled so that its increase at about 1.8 eV (*) matches the corresponding increase of the absorption of the thin film (black line).
Comparing the absorptance spectrum of the nanoparticles (green line) and the absorption coefficient of the epitaxially grown thin film (black line), which is determined in the course of this thesis, a fairly good agreement is observed. The characteristic ligand field transitions at about 1.35 eV (A) and 1.9 eV (B) are observed in both spectra. The region below the band gap is of special interest in terms of material quality, since it gives information about electronic states in the band gap. As discussed before, states that arise from the iron $3d$ electrons that are split in the ligand field are found at about 1.4 eV (A). The absorption below this ligand field transition is possibly related to defects introducing states deep in the band gap. For both spectra, the sub gap absorption is similar. In conclusion, the defect concentration of the thermally modified nanoparticles is comparable to that of the epitaxially grown film. This indicates the high quality of the nanoparticles, which can be achieved by the modification due to thermal annealing. There are few reports about the absorption characteristics of the maghemite phase. Here, two absorption spectra of a sputtered (blue star) and an epitaxially grown thin film (blue square) are presented after Wang et al. and Babkin et al., respectively [106, 105]. In comparison to the absorption data that are obtained in this thesis (black line), the absorption edge is observed at higher energies (C) and the absorption coefficient

[10] Chair of Applied Physics, Trinity College, Dublin 2, Ireland, group of Prof. Igor Shvets

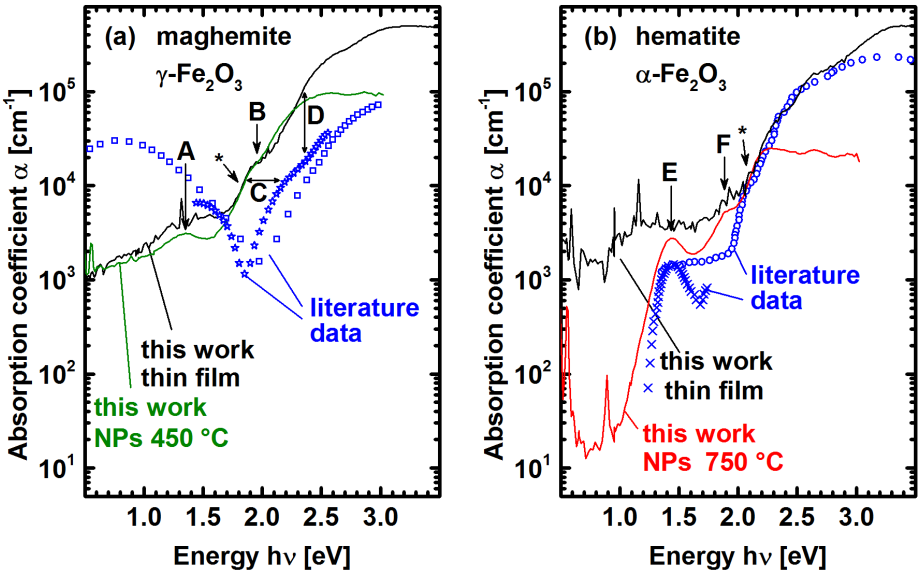

Figure 5.14 – *(a) illustrates the absorption coefficient of maghemite thin films that are prepared by sputtering (blue star) and epitaxially growth (blue square) after Wang et al. and Babkin et al., respectively [106, 105]. Additionally, the PDS spectrum of the commercially abailable maghemite nanoparticles that are annealed at 450°C (green line) and the absorption coefficient of a maghemite thin film (black line), which is measured in the course of this thesis, are given. For comparison, the absorptance of the nanoparticles is scaled so that its increase at about 1.8 eV (*) matches the corresponding increase in the absorption of the thin film (black line). (b) shows the absorption coefficient of hematite thin films in the visible region (blue circle) and of a hematite single crystal in the IR (blue cross) after Marusak et al. [104]. The PDS spectrum of the commercially available maghemite nanoparticles that are annealed at 750°C (red line) and the absorption coefficient of a hematite thin film (black line), which is measured in the course of this thesis, are presented. For comparison, the absorptance of the nanoparticles is scaled so that its increase at about 1.8 eV (*) matches the corresponding increase in the absorption of the thin film (black line).*

at the band edge is significantly lower (D). The most striking difference between the literature data and the results obtained in this thesis is the substantially higher sub gap absorption, which might indicate a higher defect concentration, and thus, a significantly worse material quality. Note, that the literature data is of questionable valididy as no detailed information about the data generation and evaluation is given.

In contrast to maghemite, reliable data of the absorption coefficient of hematite are available in the literature. Figure 5.14 (b) shows literature data of the absorption coefficient of a hematite thin film (blue circle) and a thin hematite single crystal (blue star) after Marusak et al. [104]. Additionally, the spectrum of a hematite thin film obtained from Leo Farrell that is prepared by annealing the epitaxially grown magnetite film at 650 °C (black line) is presented. Lastly, the absorptance of the nanoparticles that are annealed at 750 °C is given, but scaled for comparison (red line). The absorptance of the nanoparticles is scaled so that its increase at about 1.8 eV (*) matches the corresponding increase of the absorption of the thin film (black line)
The absorption spectra of the two hematite thin films (literature data: blue circle and present work: black line) are very similar. Below 2 eV a high sub gap absorption is detected, which is explained by a high defect concentration and the contribution from ligand field transitions (E). The absorptance of the nanoparticles shows an absorption maximum at about 1.4 eV (E) and an absorption band at 1.9 eV (F). Both features are resolved in the absorption spectra after Marusak et al. (blue circle and blue cross), but the intensity of the maximum (E) is lower and the latter feature is found at a slightly higher energy at about 2 eV. The absorption of the hematite single crystal (blue cross) decreases significantly from about 1.3 eV towards lower energies, which is also detected in the absorptance of the nanoparticles. This decrease of the absorption hints at a low defect concentration. Consequently, the hematite nanoparticles that are annealed at 750 °C exhibit a lower defect absorption compared to other thin films and are at least of the same high quality as single crystals.

5.5.3 PL in the band gap region

The emission spectra of the commercially available maghemite nanoparticles that are annealed up to 900 °C exhibit several emission bands between 1.9 eV and 2.2 eV. Figure 5.15 illustrates representative PL spectra in this spectral region. According to the discussion before, the nanoparticles are present purely in the maghemite phase up to an annealing temperature of 450 °C. After annealing at 550 °C, the maghemite as well as the hematite phase are detected, whereas only the hematite phase is observed after annealing at 750 °C and 900 °C. This phase transition is also visible in the fine structure of the emission bands between 1.9 eV and 2.2 eV. Up to an annealing temperature of 450 °C, a dominant emission peak is detected

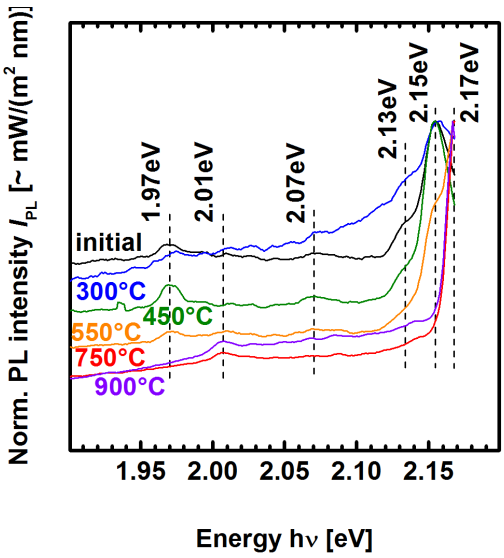

Figure 5.15 – *PL spectra of the commercially available maghemite nanoparticles in the spectral region between 1.9 eV to 2.2 eV. The spectra of the as-prepared nanoparticles as well as after annealing at different temperatures are presented.*

at 2.15 eV with a shoulder at 2.13 eV. Besides, weakly pronounced emission bands are observed at 1.97 eV and 2.07 eV, although the latter one is hardly resolved. These bands are also detected in the emission spectrum of the sample that exhibits both iron oxide phases (annealed at 550 °C, orange line). Additionally, the emission increases strongly at the border of the measurement range, which suggests a strong emission band peaked above 2.17 eV. This increase is also visible after annealing at 750 °C and 900 °C. The peak at 1.97 eV vanishes and another band at 2.01 eV occurs. Comparing these results to the electronic transitions that are observed in the absorption characteristics, these emission bands could be related to ligand field transitions of the Fe^{3+} electrons [103, 101]. As discussed in section 3.2.4, several groups reported sharp emission bands in the visible spectral region to the near UV. The detected emission bands were believed to arise from maghemite and hematite band edge emission or related ligand field as well as ligand to metal charge transfer transitions [119, 116, 120, 121, 118]. However, here, this interpretation is questionable. When the excitation laser with a central emission line at 532 nm (2.35 eV) is substituted by a 488 nm (2.56 eV) argon laser, the emission bands vanish. This finding suggests a different origin of the observed emission lines.

In order to clarify this, figure 5.16 illustrates Raman spectra of the as-prepared nanoparticles and after annealing at 550 °C and 750 °C between 200 cm^{-1} and 1600 cm^{-1} measured with an excitation laser of 488 nm (blue line) and 532 nm (green line).

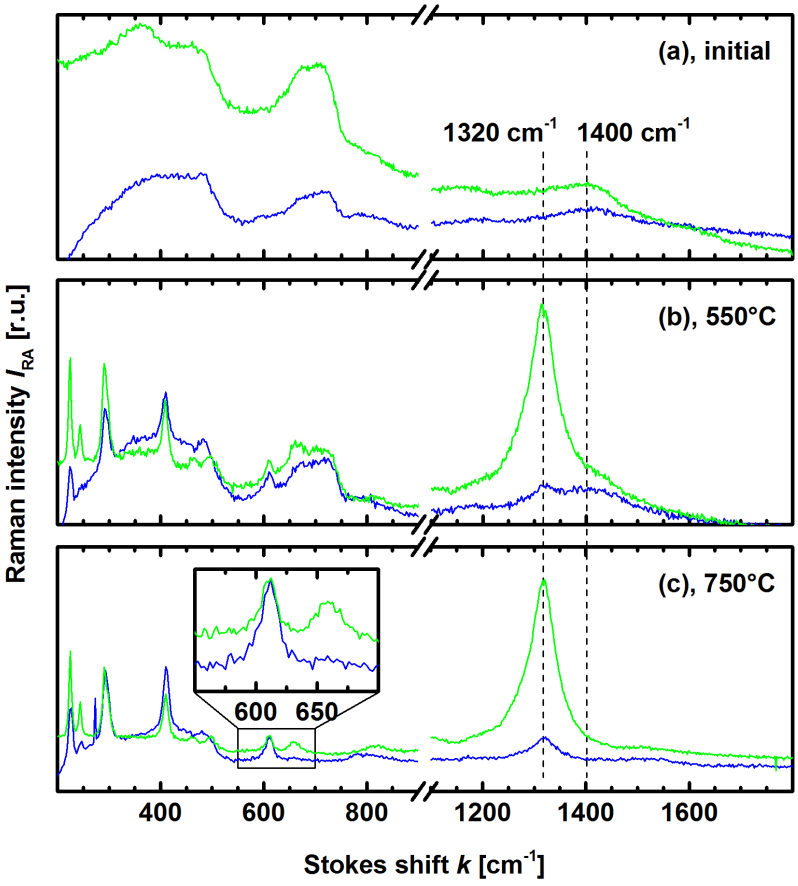

Figure 5.16 – *Raman spectra of the as-prepared commercially available maghemite nanoparticles (a) as well as after annealing at 550°C (b) and 750°C (c) in the spectral region between 200 cm^{-1} to 1800 cm^{-1}. For each sample two spectra are presented, which are measured with an excitation laser wavelength of 532 nm (green line) and 488 nm (blue line).*

Both spectra of the as-prepared nanoparticles (a) exhibit a weakly pronounced and broad Raman signal at about 1400 cm^{-1} with a shoulder at about 1600 cm^{-1}. Similar bands were observed but not explained by De Faria et al. and Varadwaj et al. [128, 146]. After annealing at 550 °C, this broad emission is also detected. Additionally, a peak at 1320 cm^{-1} appears, which is characteristic for hematite [128]. Its origin is controversly ascribed to a two-magnon process, or a two-phonon excitation [130, 131, 132, 133]. The Raman spectra are plotted against the wavenumber relative to the central excitation wavelength. Since the phonon frequency is independent from the excitation wavelength, the peaks are found at the same position for both excitation wavelengths. However, if the Raman signal is plotted against the absolute energy, the peaks appear at different positions with respect to the excitation wavelengths.

Figure 5.17 shows the PL spectra of the as-prepared nanoparticles (a), after annealing at 550 °C (b), and 750 °C (c). Moreover, the corresponding Raman spectra, which are measured with an excitation wavelength of 532 nm (green line) and 488 nm (blue line), is plotted against the absolute energy. In this depiction, the broad bands between 2.14 eV to 2.18 eV (532 nm excitation), and 2.35 eV to 2.39 eV (488 nm excitation) correspond to the broad Raman mode between 1400 cm^{-1} and 1600 cm^{-1} that is detected from the as-prepared maghemite nanoparticles. The position and shape of this Raman band that is detected with an excitation wavelength of 532 nm is similar to the PL emission between 2.12 eV to 2.17 eV.[11] Therefore, the emission between 2.12 eV to 2.17 eV is identified as a Raman mode of the maghemite phase. This interpretation is confirmed by the weak emission signal at 1.97 eV, which is in good agreement with the second order signal of this Raman mode. Furthermore, it explains, why the sharp emissions are not observed in spectra that are measured with an excitation wavelength of 488 nm. Using a 488 nm excitation wavelength, the Raman band would be detected at an absolute energy of about 2.38 eV and is consequently not revealed in the PL spectra, which are measured up to 2.2 eV. As discussed above, the maghemite nanoparticles are partially transformed into the hematite phase after annealing at 550 °C. This transition is documented by the appearance of additional Raman bands. The PL emission shows the same band at about 2.15 eV as the as-prepared sample, which can be ascribed to the broad Raman mode between 1400 cm^{-1} and 1600 cm^{-1} of the maghemite phase (cf. figure 5.17 (b)). Additionally, the emission increases strongly at the border of the measurement range. According to the previous discussion, this increase corresponds to the Raman signal at 1320 cm^{-1} of the hematite phase. The second order signal of the maghemite as well as the hematite Raman signals are weakly visible at 1.97 eV and 2.01 eV, respectively. After annealing at 750 °C, the nanoparticles are purely

[11] Slight differences of the corresponding peak positions are observed for the respective Raman and PL spectra, which is explained by the limited precision in the calibration of the x-axis of the PL spectra. For clarity, the x-axis of the Raman spectra are thus corrected by subtracting a constant offset of 0.013 eV.

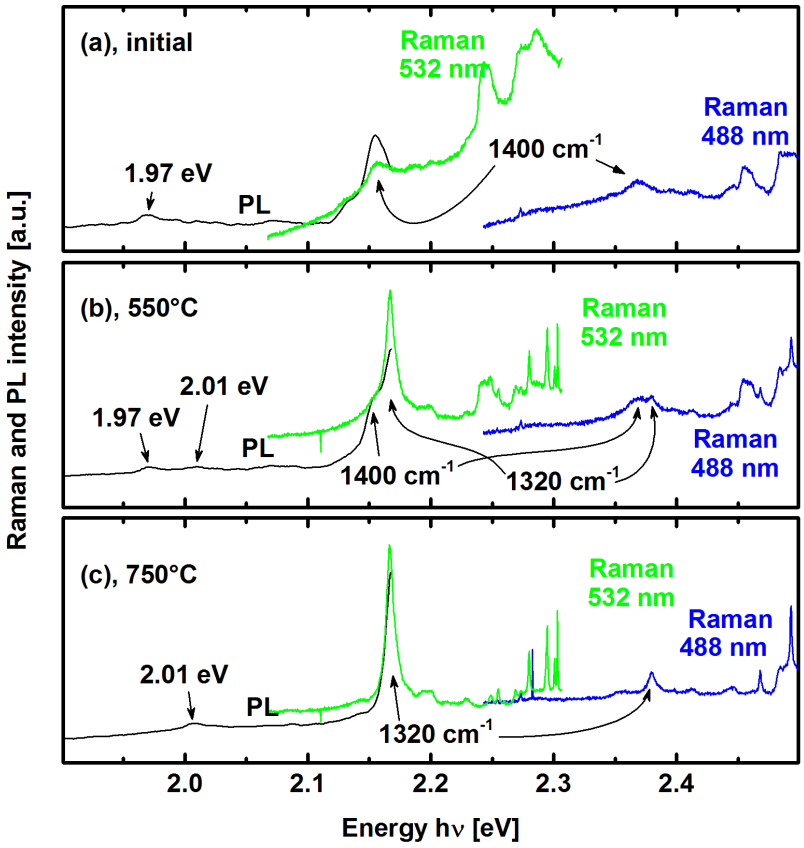

Figure 5.17 – *PL spectra (black line) of the commercially available maghemite nanoparticles between 1.9 eV to 2.2 eV of the as-prepared nanoparticles (a) as well as after annealing at 550° C (b) and 750° C (c). Additionally, corresponding Raman spectra that are measured with an excitation laser wavelength of 532 nm (green line) and 488 nm (blue line) are presented.*

present in the hematite phase. Accordingly, no signal is detected at 2.15 eV anymore, which is related to the Raman mode of the maghemite phase. Again, the first and second order of the characteristic Raman mode of hematite are observed on top of the PL emission as an increase at about 2.17 eV and a hump at 2.01 eV, respectively. Summarizing, the relatively sharp emission bands between 1.9 eV to 2.2 eV of the maghemite as well as hematite nanoparticles are identified to be pure Raman bands and are not related to radiative recombination of excited electrons. Hence, some of the emission bands, which are reported in the literature for maghemite and hematite are possibly misinterpreted and can be ascribed to their high frequency Raman modes between 1400 cm^{-1} to 1600 cm^{-1} and 1320 cm^{-1}.

Moreover, the observation of the Raman modes suggests a rather low quantum efficiency of the PL emission, or a high Raman cross section as indicated by the strong intensity of the Raman mode at 1320 cm^{-1} (cf. figure 5.16)

5.5.4 Raman spectra measured with different excitation wavelengths

Comparing the Raman spectra that are measured with an excitation laser wavelength of 532 nm (green line) and 488 nm in figure 5.16, significant differences are observed for the nanoparticles that are annealed at 550 °C (b) and 750 °C (c). Exciting with a wavelength of 532 nm (green line) the hematite Raman mode at about 1320 cm^{-1} is the predominant feature in both Raman spectra, whereas its intensity is significantly lower when exciting with a wavelength of 488 nm (blue line). Likewise, the Raman mode at 660 cm^{-1} is only observed when exciting with a wavelength of 532 nm. As discussed in this section, the latter is referred to an initially IR active vibrational mode, which becomes Raman active. In the literature, stress and defects were identified to account for the weakening of the selection rules, and hence the presence in the Raman spectra [144]. However, this does not explain why it is only resolved with an excitation wavelength of 532 nm. If the energy of the exciting photon is close to an electronic transition in the solid (resonant Raman spectroscopy), normally forbidden transitions can be observed in the Raman spectrum. The excitation wavelength of 532 nm corresponds to an energy of about 2.34 eV, which is the energy of a transition that is observed in the literature for the hematite phase. This transition is ascribed to the ${}^6A_1 + {}^6A_1 \rightarrow {}^4T_1({}^4G) + {}^4T_1({}^4G)$ pair excitation of the iron $3d$ electrons, which are split in the ligand field (cf. table 3.3). Hence, it is concluded that the peak at 660 cm^{-1} is only detected with an excitation wavelength of 532 nm due to resonant Raman scattering.
In the literature, the origin of the Raman band at 1320 cm^{-1} is controversly discussed. Either two-magnon or two-phonon processes are believed to be responsible for this Raman peak. Regarding the fact, that the frequency of the Raman mode at 1320 cm^{-1} is twice the frequency of the mode at 660 cm^{-1}, and that the mode at 660 cm^{-1} is only visible, when the intensity of the mode at 1320 cm^{-1} is high, it

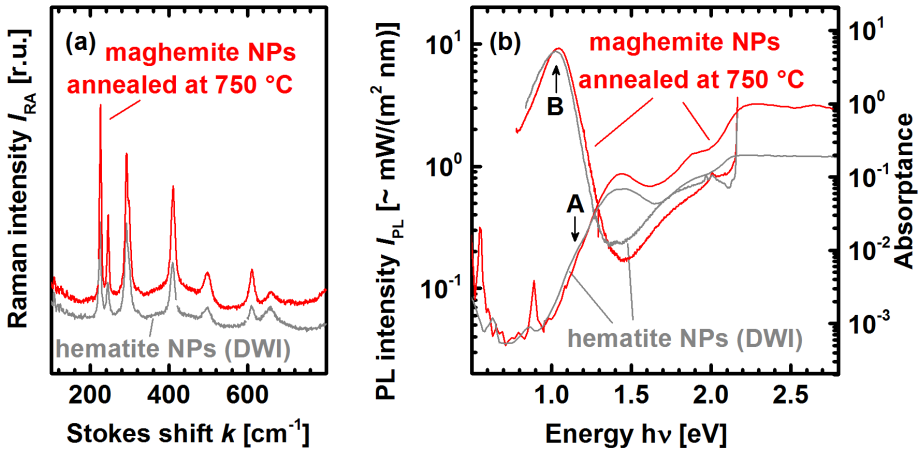

Figure 5.18 *– (a) Raman spectra of the hematite nanoparticles obtained from the DWI (grey line) and the hematite nanoparticles that are obtained by annealing of commercially available maghemite nanoparticles at 750 °C (red line). (b) corresponding PL and PDS spectra. For better comparison, the absorptance of the hematite nanoparticles obtained from the DWI is scaled.*

is concluded that it can be attributed to a two-phonon excitation of the IR active vibration.

5.5.5 Comparison different kind of hematite nanoparticles

In the present chapter two kinds of hematite nanoparticles are investigated. On the one hand, hematite nanoparticles that are obtained by thermal annealing of commercially available maghemite nanoparticles with a diameter of about 8 nm to 15 nm are analyzed. On the other hand, larger hematite nanoparticles with a diameter of about 50 nm, which are provided by the DWI, are investigated. Annealing of the commercially available nanoparticles at 750 °C leads to phase pure hematite nanoparticles with good properties in terms of a low defect concentration and homogeneiety (cf. figure 5.6). Figure 5.18 illustrates the Raman (a), PL (b), and PDS (b) spectra of the as-prepared hematite nanoparticles (grey line) and of the commercially available nanoparticles that are obtained by oven annealing at 750 °C. The larger hematite nanoparticles from the DWI possess similar absorption and emission properties. The absorption bands at 1.4 eV and 1.9 eV that are related to ligand field transitions of the Fe^{3+} electrons are marginally narrower for the commercial nanoparticles (red line). Moreover, the slope of the absorptance in the near IR of the commercial nanoparticles are slightly steeper (A) and a slightly narrower PL (B) band is observed. This could hint at a slightly higher grade of disorder. The similar

properties of the two different batches show, that high quality hematite nanoparticles can be obtained independly from the preparation technique. In comparison to bulk material, defects can efficiently be removed by thermal annealing resulting in a low defect concentration as manifested in the low sub gap absorption.

Chapter 6

Summary & Outlook

The present thesis provides a basis for an innovative solar cell concept involving nanoparticles composed of almost unlimitedly available elements as absorber material in thin film solar cells. This approach is promising to meet the requirements of increasing the production capacity and lowering the production costs. The high expectations base on the believe, that nanoparticles exhibit superior properties compared to corresponding thin films. Therefore, the goal of this thesis was to demonstrate the high quality of nanoparticles that can be achieved by proper treatment. For this, the structural and opto-electronic properties of binary oxides were investigated and the influence of thermal annealing was analyzed.

In chapter 4 of this work, the structural and opto-electronic properties of commercially available tenorite (CuO) nanoparticles were investigated and modified by thermal annealing. For this purpose, in two separate series, the nanoparticles were annealed stepwise in air or nitrogen atmosphere. After each annealing step, the structural and electronic properties were analyzed by micro-Raman and micro-PL measurements, respectively, on the same sample spot. Moreover, the optical absorption characteristics were probed by PDS measurements. Besides, XRD and TEM were applied after selected annealing steps.

The tenorite (CuO) nanoparticles were oven annealed stepwise under air or nitrogen atmosphere up to an annealing temperature of 1000 °C. Up to an annealing temperature of 1000 °C and 700 °C in air and nitrogen atmosphere, respectively, no phase transition towards cuprite (Cu_2O) was observed in Raman, PL, PDS, XRD, and TEM. The structural and opto-electronic properties of the tenorite nanoparticles with a diameter of about 30 nm were significantly improved by oven annealing. With increasing annealing temperature, structural defects were reduced and stress was released. The size of the nanoparticles increased with increasing annealing temperature. At elevated annealing temperatures, the nanoparticles sintered and formed larger aggregates with dimensions larger than 100 nm.
An emission detected at room temperature located at 1.3 eV was attributed to

tenorite band edge emission, which was in line with the band gap deduced from the PDS measurement. The emission intensity increased by more than one order of magnitude with increasing annealing temperature accompanied by a continuous decrease of the sub gap absorption, which underlined the annealing of defects. Up to now, tenorite bulk material or thin films were believed to be nonluminescent due to high defect concentrations. Hence, the occurrence of tenorite band edge emission demonstrated the high quality of the tenorite nanoparticles that was achieved by proper annealing.
Following the prevailing opinion in the literature, copper and oxygen vacancies (V_{Cu}^{ξ}, V_O^{ξ}) were believed to be the dominant point defects in the tenorite nanoparticles. Additionally, the PDS data provided evidence for the presence of oxygen interstitials (O_i^{ξ}), which concentration was more easily reduced by annealing in nitrogen atmosphere as compared to annealing in air.

After annealing at 800 °C in nitrogen atmosphere, the tenorite nanoparticles are largely transformed into cuprite (Cu_2O), but a remaining tenorite phase is still present. From Raman and PDS measurements the tenorite volume fraction is estimated to be smaller than 20%. The PL spectra at room temperature were dominated by a strong emission at 2 eV, which correlated well to the band gap derived from the PDS measurement and was consequently attributed to cuprite band edge emission. The fine structure of this emission band was correlated to phonon assisted recombination of excitons. Besides, weakly pronounced tenorite band edge and well known defect emission arising from copper and oxygen vacancies were detected below 1.8 eV. Local differences of the emission, especially in the near IR, uncovered inhomogeneity in terms of defect concentration and phase composition.

After annealing at 1000 °C in nitrogen atmosphere, the nanoparticles were completely transformed into the cuprite phase. The intensity of the band edge emission increased by more than two orders of magnitude indicating high quality material. Moreover, no significant local variations were observed any more. The emission in the near IR primarily arose from copper vacancies.
The emission spectra of cuprite material reported in the literature are usually dominated by a strongly pronounced defect related emission in the near IR and band edge emission of cuprite is rarely detected, which is ascribed to poor quality material due to a high defect concentration. Here, the extremely strong band edge emission at room temperature, which is comparable to high quality cuprite bulk material accompanied by a only weakly pronounced defect emission in the IR illustrated the excellent properties of the cuprite nanoparticles.
Irradiating the nanoparticles annealed at 800 °C or 1000 °C in nitrogen atmosphere with an excitation laser power of about 2.5 Wcm^{-2}, oxygen vacancies (V_O^{ξ}) were introduced, which was confirmed by the increase of the emission intensity at about 1.6 eV. Temperature dependent and time resolved PL measurements have to be performed to get deeper insight into the recombination mechanisms.

Putting it into a nutshell, the high PL intensity demonstrated the high quality of the tenorite and cuprite nanoparticles that was achieved by proper oven annealing and indicated the suitability of this material for photovoltaic application. In comparison to results reported for tenorite bulk material and thin films, nanoparticles included fewer defects and therefore showed superior opto-electronic properties. The cuprite nanoparticles exhibited excellent properties at least similar to high quality bulk material. Consequently, the assumption was confirmed that high quality nanoparticles can be easier prepared than corresponding thin films or bulk material.

Chapter 5 dealt with the characterization and modification of iron oxide nanoparticles. The structural and opto-electronic properties of commercially available maghemite (γ-Fe_2O_3) as well as hematite (α-Fe_2O_3) nanoparticles that were provided by the Institute of Interactive Materials Research DWI an der RWTH Aachen e.V. were investigated.

The commercially available maghemite nanoparticles with a diameter of about 8 nm to 15 nm were annealed stepwise in nitrogen atmosphere up to an annealing temperature of 900 °C. After each annealing step, the structural and opto-electronic properties were analyzed by Raman, PL, and PDS measurements.

Up to an annealing temperature of 450 °C, the nanoparticles remain in the maghemite phase. Slight changes of the Raman spectra were attributed to a higher structural order, which was believed to arise from ordering of iron vacancies with increasing annealing temperature. The optical band gap of about 2 eV was derived from the PDS measurements and characteristic absorption features at 1.3 eV and 1.9 eV were attributed to the ${}^6A_1 \rightarrow {}^4T_1({}^4G)$ and ${}^6A_1 \rightarrow {}^4T_2({}^4G)$ ligand field transitions of the iron $3d$ electrons, respectively. Moreover, the sub gap absorption was slightly reduced indicating the annealing of defects. Comparing the absorption spectra of the nanoparticles to literature data as well as to spectra of high quality thin films that were investigated in the course of this thesis, it was demonstrated that the nanoparticles exhibited excellent properties that were at least comparable to high quality thin films. In the spectral region of the band gap, a weakly pronounced luminescence was detected and attributed to maghemite band edge emission. Additionally, an emission band centered at about 0.9 eV was observed in the near IR. The origin of this emission was not identified unambigeously, but transitions involving defect states or stokes shifted ${}^6A_1 \rightarrow {}^4T_1({}^4G)$ ligand field transition were considered to give rise to this emission.
After annealing at 550 °C, the presence of the maghemite as well as the hematite phase was confirmed. It could not be decided if different phases were present in different nanoparticles or if single nanoparticles contained both phases. According to the resemblance of the electronic structure of these two compounds, the absorption and emission spectra changed only slightly. But in the near IR an additional emission occured at about 1 eV. Also, the origin of this transition remained unexplained.

After annealing at 750 °C, the nanoparticles were completely transformed into the hematite phase. The emission intensity at 1 eV increased by about one order of magnitude, which was explained by a reduced defect concentration. Moreover, no emission was detected at the low energy side of this PL signal. The intensity of the broad emission band in the region of the band gap increased slightly and the sub gap absorption decreased tremendously, which showed the improvement of the material quality.

Annealing at 900 °C, defects were introduced into the nanoparticles. Though a higher sub gap absorption was observed, the emission in the region of the band gap increased marginally. Again, the dominant emission at 1 eV was detected, but a second peak at 0.9 eV appeared. In order to clarify the origin of the emission bands in the near IR, temperature dependent and time resolved PL measurements have to be performed in the future.

Also, the absorption characteristics of the hematite nanoparticles were compared to literature data as well as high quality thin films that were investigated in the course of this thesis. It was demonstrated that the hematite nanoparticles showed excellent properties that were at least comparable to high quality thin films and single crystalline bulk material. Hence, this provides further evidence that high quality nanoparticles can be easier prepared than corresponding thin films.

Apart from the hematite nanoparticles that were obtained by annealing of maghemite nanoparticles, the Institute of Interactive Materials Research DWI an der RWTH Aachen e.V. provided hematite nanoparticles with a diameter of about 50 nm. Raman, PL, and PDS measurements revealed similar structural and opto-electronic as the oven annealed hematite nanoparticles implying that the observed results were not related to size dependent effects.

Strong Raman modes of maghemite and hematite were observed on top of the respective PL emission between 2 eV and 2.2 eV. In the literature, the observation of these Raman modes in PL spectra is probably misinterpreted as maghemite or hematite band edge emission.

Summarizing, although high quality iron oxide nanoparticles were prepared, the feasability of maghemite as well as hematite nanoparticles as a direct absorber material in thin film solar cells had to be questioned. Exhibiting a considerably high absorption coefficients of about $10^5\,\mathrm{cm}^{-1}$ above the band gap in the region between 2 eV and 2.2 eV, maghemite and hematite had been believed to be potential absorber in a multi-junction solar cell harvesting the solar spectrum in the region above 2 eV. However, the absorption and emission spectra clearly demonstrated that electronic states were introduced deep in the band gap due to the ligand field splitting of iron $3d$ electrons. This intrinsic property of both iron oxides is expected to limit the

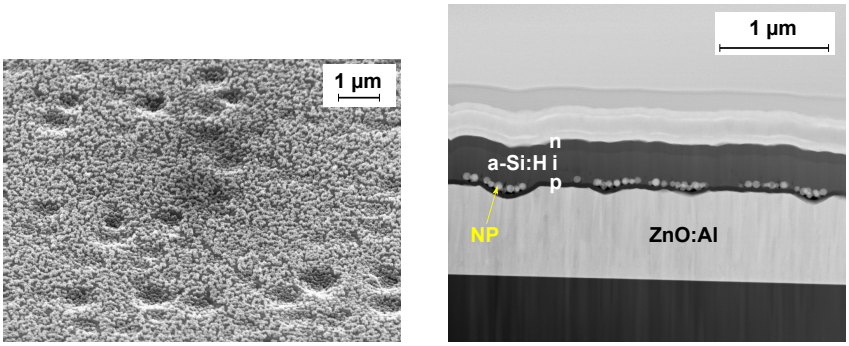

Figure 6.1 *– (a) SEM image of hematite nanoparticles that are deposited by spin-coating onto a p-type amorphous silicon (a-Si:H(p)) layer. (b) scanning transmission electron microscopy (STEM) image of an amorphous silicon p-i-n solar cell with embedded hematite nanoparticles.*

Fermi-level splitting, and thus would restrict the achievable open circuit voltage of a photovoltaic device drastically.

Also, the possibility to use maghemite and hematite as a low band gap absorber by exploiting the interband directly was disregarded due to the low corresponding absorption coefficient of the order of $10^3\,\mathrm{cm}^{-1}$, which is not compatable with the innovative solar cell concept presented in this thesis.

In future work, several tasks have to be addressed. In the present thesis, we showed that nanoparticles exhibit promising opto-electronic properties for the application as absorber material in solar cells that can be achieved by proper annealing. Besides, there are a variety of other techniques which can be applied to enhance the quality of the nanoparticles, i.e. the passivation and functionalization of surfaces by gas phase or chemical reactions, as well as the embedding of nanoparticles in a matrix material.

Temperature dependent and time resolved PL measurements must be employed to get information about the lifetimes and activation energies. Thermo power as well as Hall measurements have to be performed to identify the type of doping and charge carrier concentration of the nanoparticles. Moreover, measurements of the electric conductivity need to be conducted to probe their transport properties. For this purpose, new methods have to be developed to investigate the properties of single nanoparticles, i.e. using a conductive atomic force microscope (c-AFM) to detect I/V characteristics locally.

For a proof of concept, nanoparticles have to be incorporated into a thin film solar cell. For this, mono- or multilayer of nanoparticles must be prepared. Recently, the hematite nanoparticles that are provided from the DWI were used as a model system to prepare homogeneous nanoparticle layers. Figure 6.1 (a) shows a SEM image of the hematite nanoparticles that are deposited onto a p-type amorphous silicon (a-Si:H(p)) layer by spin-coating. In a further step, the hematite nanoparticles were embedded into an amorphous silicon solar cell (cf. figure 6.1 (b)). The resulting device showed the typical I/V characteristics of a solar cell, but no generation of charge carriers due to the absorption of light in the nanoparticles could be confirmed. Nevertheless, this prototype demonstrated the possibility of producing a working solar cell including nanoparticles.
Furthermore, the presented characterization techniques and embedding experiments have to be applied to other material systems such as β-$FeSi_2$, pyrite-FeS_2, ZrS_2, and chalcocite-Cu_2S.

Bibliography

[1] M. A. Green, *Progress in Photovoltaics: Research and Applications* **17**, 347 (2009).

[2] V. Fthenakis, *Renewable and Sustainable Energy Reviews* **13**, 2746 (2009).

[3] K. Radermacher, R. Carius, and S. Mantl, *Nuclear Instruments and Methods in Physics Research Section B: Beam Interactions with Materials and Atoms* **84**, 163 (1994).

[4] M. C. Bost and J. E. Mahan, *Journal of Applied Physics* **58**, 2696 (1985).

[5] R. M. Cornell and U. Schwertmann, *The Iron Oxides*, Wiley-VCH Verlag GmbH Co. KGaA, Weinheim, FRG, 2003.

[6] C. N. Wadia, *Establishing Iron Pyrite (FeS_2) and Chalcocite (Cu_2S) as a Novel Material Pair for Low Cost Photovoltaic Devices*, PhD thesis, University of California, Berkley, 2008.

[7] M. Shaban, K. Nakashima, W. Yokoyama, and T. Yoshitake, *Japanese Journal of Applied Physics* **46**, L667 (2007).

[8] A. Ennaoui, S. Fiechter, C. Pettenkofer, N. Alonso-Vante, K. Büker, M. Bronold, C. Höpfner, and H. Tributsch, *Solar Energy Materials and Solar Cells* **29**, 289 (1993).

[9] J. Herion, *Applied Physics Letters* **34**, 599 (1979).

[10] C. Wadia, Y. Wu, S. Gul, S. K. Volkman, J. Guo, and A. P. Alivisatos, *Chemistry of Materials* **21**, 2568 (2009).

[11] Y. Wu, C. Wadia, W. Ma, B. Sadtler, and A. P. Alivisatos, *Nano letters* **8**, 2551 (2008).

[12] L. Li, H. Wang, X. Fang, T. Zhai, Y. Bando, and D. Golberg, *Energy Environmental Science* **4**, 2586 (2011).

[13] F. Urbach, *Physical Review* **92**, 1324 (1953).

[14] T. Skettrup, *Physical Review B* **18**, 2622 (1978).

[15] D. Dexter, *Physical Review Letters* **19**, 1383 (1967).

[16] J. Joannopoulos, *The Physics of Hydrogenated Amorphous Silicon: Electronic and Vibrational Properties: 2*, Springer-Verlag, Berlin, 1984.

[17] W. B. Jackson, N. M. Amer, A. C. Boccara, and D. Fournier, *Applied Optics* **20**, 1333 (1981).

[18] W. K. Rontgen, *Nature* **53**, 274 (1896).

[19] B. Warren, X-Ray Studies of Deformed Metals, in *Progress in Metal Physics*, chapter X-Ray Stud, pp. 147–202, Pergamon Press, London, 8 edition, 1959.

[20] B. E. Warren and B. L. Averbach, *Journal of Applied Physics* **21**, 595 (1950).

[21] J. Flohre, *Charakterisierung und Modifizierung von halbleitenden Nanopartikeln für Solarzellen*, PhD thesis, Rheinisch-Westfälische Technische Hochschule Aachen, 2010.

[22] J. Bergmann, *Charakterisierung und Modifizierung von CuO-Nanopartikeln an einem automatisierten Mikro-Raman-Photolumineszenz-Aufbau*, PhD thesis, Universität Duisburg-Essen, 2012.

[23] A. E. Rakhshani, *Review Literature And Arts Of The Americas* **29**, 7 (1986).

[24] M. R. Wright, *The Hall Effect and Electrical Conductivity of Single Crystal Cuprous-Oxide*, PhD thesis, Wayne State University, Detroit, MI, Dept. Chemistry, 1962.

[25] J. R. Coughlin, *U.S. Bur. Mines Bull.* **20**, 542 (1954).

[26] M. O'Keeffe and W. J. Moore, *The Journal of Chemical Physics* **36**, 3009 (1962).

[27] A. E. Rakhshani and J. Varghese, *Physica Status Solidi (a)* **101**, 479 (1987).

[28] B. K. Meyer, A. Polity, D. Reppin, M. Becker, P. Hering, P. J. Klar, T. Sander, C. Reindl, J. Benz, M. Eickhoff, C. Heiliger, M. Heinemann, J. Bläsing, A. Krost, S. Shokovets, C. Müller, and C. Ronning, *physica status solidi (b)* , n/a (2012).

[29] L. Grondahl, *Reviews of Modern Physics* **5**, 141 (1933).

[30] W. Brattain, *Reviews of Modern Physics* **23**, 203 (1951).

[31] L. Grondahl and P. H. Geiger, *Transactions of the American Institute of Electrical Engineers* **XLVI**, 357 (1927).

[32] R. S. Toth, R. Kilkson, and D. Trivich, *Journal of Applied Physics* **31**, 1117 (1960).

[33] A. Rakhshani, A. Al-Jassar, and J. Varghese, *Thin Solid Films* **148**, 191 (1987).

[34] V. Drobny and L. Pulfrey, *Thin Solid Films* **61**, 89 (1979).

[35] L. Papadimitriou, N. A. Economou, and D. Trivich, *Solar Cells* **3**, 73 (1981).

[36] J. Herion, E. Niekisch, and G. Scharl, *Solar Energy Materials* **4**, 101 (1980).

[37] B. Rai, *Solar Cells* **25**, 265 (1988).

[38] L. C. Olsen, R. C. Bohara, and M. W. Urie, *Applied Physics Letters* **34**, 47 (1979).

[39] L. C. Olsen, F. W. Addis, and W. Miller, **7**, 247 (1983).

[40] M. Balkanski, Y. Petroff, and D. Trivich, *Solid State Communications* **5**, 85 (1967).

[41] J. Grun, M. Sieskind, and S. Nikitine, *Journal of Physics and Chemistry of Solids* **19**, 189 (1961).

[42] J. Dahl and A. Switendick, *Journal of Physics and Chemistry of Solids* **27**, 931 (1966).

[43] R. Elliott, *Physical Review* **124**, 340 (1961).

[44] R. Elliott, *Physical Review* **108**, 1384 (1957).

[45] V. T. Agekyan, *Physica Status Solidi (a)* **43**, 11 (1977).

[46] A. Daunois, J. Deiss, and B. Meyer, *Journal de Physique* **27**, 142 (1966).

[47] R. Forman, W. Brower, and H. Parker, *Physics Letters A* **36**, 395 (1971).

[48] D. Fröhlich, R. Kenklies, C. Uihlein, and C. Schwab, *Physical Review Letters* **43**, 1260 (1979).

[49] J. W. Hodby, T. E. Jenkins, C. Schwab, H. Tamura, and D. Trivich, *Journal of Physics C: Solid State Physics* **9**, 1429 (1976).

[50] T. Ohyama, T. Ogawa, and H. Nakata, *Physical Review B* **56**, 3871 (1997).

[51] C. Malerba, F. Biccari, C. Leonor Azanza Ricardo, M. D'Incau, P. Scardi, and A. Mittiga, *Solar Energy Materials and Solar Cells* **95**, 2848 (2011).

[52] J. Pastrnak and R. Kuzel, *Soviet Physics-Solid State* **1**, 888 (1959).

[53] D. W. Snoke, A. J. Shields, and M. Cardona, *Physical Review B* **45**, 11693 (1992).

[54] F. L. Weichman and J. M. Reyes, *Canadian Journal of Physics* **58**, 325 (1980).

[55] B. Prevot, C. Carabatos, and M. Sieskind, *Physica Status Solidi (a)* **10**, 455 (1972).

[56] M. Zouaghi, B. Prevot, C. Carabatos, and M. Sieskind, *Physica Status Solidi (a)* **11**, 449 (1972).

[57] M. Zouaghi, *Physica Status Solidi (a)* **11**, 219 (1972).

[58] S. AGGARWAL, *Solid State Ionics* **101-103**, 321 (1997).

[59] J. Xue and R. Dieckmann, *Journal of Physics and Chemistry of Solids* **51**, 1263 (1990).

[60] J. Bloem, A. Van der Houven van Oordt, and F. Kröger, *Physica* **22**, 1254 (1956).

[61] J. Bloem, *Philips Research Reports* **13**, 167 (1958).

[62] N. Peterson and C. Wiley, *Journal of Physics and Chemistry of Solids* **45**, 281 (1984).

[63] N. Peterson and C. Wiley, *Journal of Physics and Chemistry of Solids* **45**, 295 (1984).

[64] J. Xue and R. Dieckmann, *Journal of Physics and Chemistry of Solids* **51**, 1263 (1990).

[65] J. H. Park and K. Natesan, *Oxidation of Metals* **39**, 411 (1993).

[66] O. PORAT and I. RIESS, *Solid State Ionics* **74**, 229 (1994).

[67] H. Raebiger, S. Lany, and A. Zunger, *Physical Review B* **76**, 045209 (2007).

[68] D. Scanlon and G. Watson, *Physical Review Letters* **106**, 186403 (2011).

[69] J. L. Birman, *Solid State Communications* **13**, 1189 (1973).

[70] T. Ito, H. Yamaguchi, K. Okabe, and T. Masumi, *Journal of Materials Science* **33**, 3555.3566 (1998).

[71] R. G. Kaufman, *Journal of The Electrochemical Society* **131**, 385 (1984).

[72] T. Ito and T. Masumi, *Journal of the Physics Society Japan* **66**, 2185 (1997).

[73] K. Huang, *Zeitschrift fuer Physik* **171**, 213 (1963).

[74] C. Carabatos, B. Prevot, and L. Symmetry, *Phys. Stat. Sol . (b)* **44**, 701 (1971).

[75] M. O'Keeffe, *The Journal of Chemical Physics* **39**, 1789 (1963).

[76] E. C. Heltemes, *Physical Review* **141**, 803 (1966).

[77] J. Reydellet, *Phys. Stat. Sol. (b)* **52**, 175 (1972).

[78] P. Dawson, M. M. Hargreave, and G. R. Wilkinson, *J. Phys. Chem. Solids* **34**, 2201 (1973).

[79] M. Balkanski, M. Nusimovici, and J. Reydellet, *Solid State Communications* **7**, 815 (1969).

[80] A. Compaan and H. Cummins, *Physical Review B* **6**, 4753 (1972).

[81] J. Chrzanowski and J. Irwin, *Solid State Communications* **70**, 11 (1989).

[82] H. Hagemann, H. Bill, W. Sadowski, E. Walker, and M. François, *Solid State Communications* **73**, 447 (1990).

[83] S. Guha, D. Peebles, and J. Terence Wieting, *Bulletin of Materials Science* **14**, 539 (1991).

[84] L. Debbichi, M. C. Marco de Lucas, J. F. Pierson, and P. Krüger, *The Journal of Physical Chemistry C* **116**, 10232 (2012).

[85] S. Å sbrink and L. J. Norrby, *Acta Crystallographica Section B Structural Crystallography and Crystal Chemistry* **26**, 8 (1970).

[86] M. O'Keeffe and J.-O. Bovin, *American Mineralogist* **63**, 180 (1978).

[87] H. Wieder, *Journal of Applied Physics* **37**, 184 (1966).

[88] V. Drobny and L. Pulfrey, *Thin Solid Films* **61**, 89 (1979).

[89] A. Roos and B. Karlsson, *Solar Energy Materials* **7**, 467 (1983).

[90] F. P. Koffyberg and F. A. Benko, *Journal of Applied Physics* **53**, 1173 (1982).

[91] F. Marabelli, G. Parravicini, and F. Salghetti-Drioli, *Physical Review B* **52**, 1433 (1995).

[92] S. Suda, S. Fujitsu, K. Koumoto, and H. Yanagida, *Japanese Journal of Applied Physics* **31**, 2488 (1992).

[93] Y. Peng, Z. Zhang, T. Viet Pham, Y. Zhao, P. Wu, and J. Wang, *Journal of Applied Physics* **111**, 103708 (2012).

[94] D. Wu, Q. Zhang, and M. Tao, *Physical Review B* **73**, 235206 (2006).

[95] M. Vila, C. Díaz-Guerra, and J. Piqueras, *Journal of Physics D: Applied Physics* **43**, 135403 (2010).

[96] R. Al-Gaashani, S. Radiman, N. Tabet, and A. Razak Daud, *Journal of Alloys and Compounds* **509**, 8761 (2011).

[97] S.-S. Chang, H.-J. Lee, and H. J. Park, *Ceramics International* **31**, 411 (2005).

[98] G. Shirane, S. Pickart, R. Nathans, and Y. Ishikawa, *Journal of Physics and Chemistry of Solids* **10**, 35 (1959).

[99] P. J. Flanders and W. J. Schuele, *Philosophical Magazine* **9**, 485 (1964).

[100] E. Verwey, *Z. Krist.* **A91**, 65 (1935).

[101] D. M. Sherman, *Physics and Chemistry of Minerals* **12**, 161 (1985).

[102] J. Slater, *Physical Review* **165**, 655 (1968).

[103] D. Sherman and T. Waite, *Amercian Mineralogist* **70**, 1262 (1985).

[104] L. Marusak, R. Messier, and W. B. White, *Journal of Physics and Chemistry of Solids* **41**, 981 (1980).

[105] E. Babkin, K. Koval, and V. Pynko, *Thin Solid Films* **117**, 217 (1984).

[106] H. Wang, J. Shen, and J. Qian, *Journal of Magnetism and Magnetic Materials* **73**, 103 (1988).

[107] R. K. Quinn, R. Nasby, and R. Baughman, *Materials Research Bulletin* **11**, 1011 (1976).

[108] K. L. Hardee, *Journal of The Electrochemical Society* **123**, 1024 (1976).

[109] H. H. Kung, H. S. Jarrett, A. W. Sleight, and A. Ferretti, *Journal of Applied Physics* **48**, 2463 (1977).

[110] L.-S. R. Yeh, *Journal of The Electrochemical Society* **124**, 833 (1977).

[111] J. Tossell, D. Vaughan, and K. Johnson, *Nature Phyical Science* **244**, 42 (1973).

[112] A. I. Galuza, *Low Temperature Physics* **24**, 726 (1998).

[113] H. Takei and S. Chiba, *Journal of the Physical Society of Japan* **21**, 1255 (1966).

[114] C. Greaves, *Journal of Solid State Chemistry* **49**, 325 (1983).

[115] K. Haneda and A. Morrish, *Solid State Communications* **22**, 779 (1977).

[116] M. F. Chioncel, C. DiÌaz-Guerra, and J. Piqueras, *Journal of Applied Physics* **104**, 124311 (2008).

[117] H. Fei, X. Ai, M. Gao, Y. Yang, T. Zhang, and J. Shen, *Journal of Luminescence* **66-67**, 345 (1995).

[118] Q. Han, Z. Liu, Y. Xu, Z. Chen, T. Wang, and H. Zhang, *J. Phys. Chem. C* **111**, 5034 (2007).

[119] B. Zou and V. Volkov, *Journal of Physics and Chemistry of Solids* **61**, 757 (2000).

[120] J. Wang, W. B. White, and J. H. Adair, *Materials Letters* **60**, 2013 (2006).

[121] N. Tsuda, K. Nasu, A. Yanase, and K. Siratori, *Electronic Conduction in Oxide*, Springer-Verlag, Berlin, springer s edition, 1991.

[122] B. Zou, W. Huang, M. Y. Han, S. F. Y. Li, W. Xiaochun, Y. Zhang, J. Zhang, W. Pengfei, and R. Wang, *Journal of Physics and Chemistry of Solids* **58**, 1315 (1997).

[123] X. Ai, H. Fei, Y. Yang, L. Han, R. Nie, Y. Zhang, C. Zhao, L. Xiao, T. Li, J. Zhao, and J. Yu, *Journal of Luminescence* **60-61**, 364 (1994).

[124] J. de Wit, A. Broersma, and M. Stroband, *Journal of Solid State Chemistry* **37**, 242 (1981).

[125] M. Hanesch, *Geophysical Journal International* **177**, 941 (2009).

[126] I. R. Beattie and T. R. Gilson, *Journal of the Chemical Society A: Inorganic, Physical, Theoretical* , 980 (1970).

[127] S. Oh, D. Cook, and H. Townsend, *Hyperfine Interactions* **112**, 59 (1998).

[128] D. L. A. de Faria, S. Venâncio Silva, and M. T. de Oliveira, *Journal of Raman Spectroscopy* **28**, 873 (1997).

[129] C. Shull, W. Strauser, and E. Wollan, *Physical Review* **83**, 333 (1951).

[130] T. Hart, S. Adams, and T. H., No Title, in *Proceedings of the 3rd International Conference on Light Scattering in Solids*, edited by B. M., R. Leite, and P. S., p. 259, Paris, 1976.

[131] T. Martin, R. Merlin, D. Huffman, and M. Cardona, *Solid State Communications* **22**, 565 (1977).

[132] K. McCarty, *Solid State Communications* **68**, 799 (1988).

[133] M. Massey, U. Baier, R. Merlin, and W. Weber, *Physical Review B* **41**, 7822 (1990).

[134] F. DeBoer and P. Selwood, *J. Am. Chem. Soc.* **76**, 3366 (1954).

[135] O. Shebanova and P. Lazor, *Journal of Raman Spectroscopy* **34**, 845 (2003).

[136] J. Dünnwald and A. Otto, *Fresenius' Zeitschrift für analytische Chemie* **319**, 738 (1984).

[137] B. Brockhouse and H. Watanabe, *Physics Letters* **1**, 189 (1962).

[138] M. C. Neuburger, *Zeitschrift für Physik* **67**, 845 (1931).

[139] D. Balzar, Voigt-Function Model in Diffraction Line-Broadening Analysis, in *Defect and Microstructure Analysis from Diffraction*, edited by R. Snyder, H. Bunge, and J. Fiala, pp. 94 – 126, International Union of Crystallography, New York, 1999.

[140] D. Wu, Q. Zhang, and M. Tao, *Physical Review B* **73**, 235206 (2006).

[141] D. Wu, *A First-Principle study on bulk CuO: Electronic Structures and Native Point Defects*, PhD thesis, University of Texas at Arlington, 2005.

[142] M. Ozaki, S. Kratohvil, and E. Matijević, *Journal of Colloid and Interface Science* **102**, 146 (1984).

[143] N. Pailhé, A. Wattiaux, M. Gaudon, and A. Demourgues, *Journal of Solid State Chemistry* **181**, 2697 (2008).

[144] S.-H. Shim and T. Duffy, *American Mineralogist* **87**, 318 (2001).

[145] S. Onari, T. Arai, and K. Kudo, *Physical Review B* **16**, 1717 (1977).

[146] K. Varadwaj, M. Panigrahi, and J. Ghose, *Journal of Solid State Chemistry* **177**, 4286 (2004).

Acknowledgments-Dank

Hiermit möchte ich allen Danken, die zum Gelingen der vorliegenden Arbeit beigetragen haben. Mein besonderer Dank gilt dabei:

- meinem Erstgutachter und Institutsleiter Prof. Dr. U. Rau für die Möglichkeit meine Doktorarbeit am IEK-5 des Forschungszentrums Jülich anzufertigen
- Herrn Prof. Dr. A. Lorke für die Übernahme der Aufgabe des Zweitgutachters
- meinem Betreuer Prof. Dr. R. Carius für die stets gute Betreuung und Unterstützung sowie viele inspirierende Gespräche. Besonders möchte ich mich für die Hilfe Endphase der Anfertigung meiner Arbeit bedanken, in der kaum ein Wochenende verstrich, ohne dass der ein oder andere Absatz diskutiert wurde
- unserem Team bestehend aus Christine Leidinger, Jan Flohre, Dr. Florian Köhler, Jens Bergmann und Dr. Stefan Muthmann für die gute Zusammenarbeit und Hilfe während der gesamten Zeit meines Promotionsvorhabens am IEK-5 und insbesondere für die Durchsicht einzelner Kapitel dieser Arbeit und der seelischen Unterstützung als das Ende noch nicht in Sicht war
- Oliver Thimm, Josef Klomfaß und Markus Hülsbeck ohne deren Temperexperimente, PDS Messungen und technische Unterstützung es keinen Grund gäbe diese Danksagung zu schreiben, da die Dissertation dazu fehlen würde
- meinen ehemaligen Bürokollegen Dr. Etienne Moulin und David Wippler, die mich seit meiner Ankunft am Institut im November 2008 begleitet haben
- Andrea Mülheims, Petra Lorbach und Susanne Griesen für die Unterstützung bei allen formalen Fragen
- Daniel Weigand für das Foto des PL und Raman Aufbaus, das die Titelseite dieser Arbeit ziert
- meiner Mutter Beate, meinem Vater Gottfried und meinen Geschwistern Dr. Marcel und Madeleine
- all jenen, die es verdient haben an dieser Stelle genannt zu werden...

Band / Volume 278
Keramiken des Monazit-Typs zur Immobilisierung von minoren Actinoiden und Plutonium
J. M. Heuser (2015), viii, 212 pp
ISBN: 978-3-95806-076-0

Band / Volume 279
IEK-3 Report 2015
Systems Research and Engineering for a Sustainable Energy Supply
(2015)
ISBN: 978-3-95806-077-7

Band / Volume 280
IEK-3 Report 2015
Systemforschung und –technik für eine nachhaltige Energieversorgung
(2015)
ISBN: 978-3-95806-078-4

Band / Volume 281
Integration of the German energy transition in the EU-context
A. Ernst (2015), 76 pp
ISBN: 978-3-95806-079-1

Band / Volume 282
Modelling and Experimental Validation of the Viscosity of Liquid Phases in Oxide Systems Relevant to Fuel Slags
G. Wu (2015), XVI, 170 pp
ISBN: 978-3-95806-081-4

Band / Volume 283
Entwicklung von geträgerten protonenleitenden Dünnschichtmembranen für die Wasserstoffabtrennung
W. Deibert (2015), XI, 117 pp
ISBN: 978-3-95806-082-1

Band / Volume 284
Thermochemische Beständigkeit von keramischen Membranen und Katalysatoren für die H_2-Abtrennung in CO-Shift-Reaktoren
E. M. H. Forster (2015), X, 137 pp
ISBN: 978-3-95806-084-5

Band / Volume 285
Spektrale aktinische Flussdichten und Photolysefrequenzen - Untersuchungen in der atmosphärischen Grenzschicht und der freien Troposphäre
I. M. Lohse (2015), VI, 111, VII-XXIII pp
ISBN: 978-3-95806-086-9

Band / Volume 286
Neue Charakterisierungsmethoden für die Gasdiffusionslage in PEM-Brennstoffzellen vor dem Hintergrund produktionsprozessbedingter Materialschwankungen
S. M. Bach (2015), VIII, 149 pp
ISBN: 978-3-95806-088-3

Band / Volume 287
Using the anisotropy of electrical properties for the characterization of sedimentological structures and preferential flow processes
S. Al-Hazaimay (2015), xxii, 94 pp
ISBN: 978-3-95806-090-6

Band / Volume 288
Aktivitätsuntersuchungen und Methoden zur Regeneration von Katalysatoren für die autotherme Reformierung von Dieselkraftstoffen
K. Löhken (2015), II, 147 pp
ISBN: 978-3-95806-093-7

Band / Volume 289
Large-Scale Three Dimensional Modelling of a Direct Methanol Fuel Cell Stack
J. W. McIntyre (2015), 138 pp
ISBN: 978-3-95806-094-4

Band / Volume 290
Abscheidung von Wärmedämmschichtsystemen mit dem Plasma Spray-Physical Vapor Deposition- (PS-PVD-) Prozess – Untersuchung des Prozesses und der hergestellten Schichten
S. Rezanka (2015), XII, 234 pp
ISBN: 978-3-95806-095-1

Band / Volume 291
Characterization & Modification of Copper and Iron Oxide Nanoparticles for Application as Absorber Material in Silicon based Thin Film Solar Cells
Nuys (2015), XII, 123 pp
ISBN: 978-3-95806-096-8

Energie & Umwelt /
Energy & Environment
Band / Volume 291
ISBN 978-3-95806-096-8

JÜLICH
FORSCHUNGSZENTRUM